

**MOLECULAR ANALYSIS OF ENGINEERED  
NANOMATERIALS IN BIOMEDICAL AND  
REGENERATIVE MEDICINE APPLICATIONS**

A DISSERTATION SUBMITTED TO  
THE GRADUATE SCHOOL OF ENGINEERING AND SCIENCE  
OF BILKENT UNIVERSITY  
IN PARTIAL FULFILLMENT OF THE REQUIREMENTS FOR  
THE DEGREE OF  
DOCTOR OF PHILOSOPHY  
IN  
MATERIALS SCIENCE AND NANOTECHNOLOGY

By  
NURAY GÜNDÜZ

April 2019

**MOLECULAR ANALYSIS OF ENGINEERED NANOMATERIALS IN  
BIOMEDICAL AND REGENERATIVE MEDICINE APPLICATIONS**

By Nuray Gündüz

April 2019

We certify that we have read this dissertation and that in our opinion it is fully adequate, in scope and in quality, as a dissertation for the degree of Doctor of Philosophy.

---

Çağlar Elbüken (Advisor)

---

Ayşe Begüm Tekinay (Co-advisor)

---

Ömer Hıdır Yılmaz (Co-advisor)

---

Melih Önder Babaoğlu

---

Dönüş Tuncel

---

Bahar Değirmenci Uzun

---

Sreeparna Banarjee

Approved for the Graduate School of Engineering and Science:

---

Ezhan Karaşan

Director of the Graduate School

# ABSTRACT

## MOLECULAR ANALYSIS OF ENGINEERED NANOMATERIALS IN BIOMEDICAL AND REGENERATIVE MEDICINE APPLICATIONS

Nuray Gündüz

Ph.D. in Materials Science and Nanotechnology

Advisor: Çağlar Elbüken

Co-Advisor: Ayşe Begüm Tekinay

Co-Advisor: Ömer H. Yılmaz

April, 2019

Molecular mechanisms are inspiration source for effective nanomaterial synthesis through minimalist bottom-up approaches. Mimicking functional bio-physicochemical properties of biomacromolecules can give new insights for design and synthesis of nanomaterials used in biomedical and regenerative medicine applications. In this thesis, rationally-designed nanomaterials and their biomedical applications as oral ketone delivery and biomineralization and long-term potential toxicities were investigated. In the first chapter, basic concepts of nanomaterial design, synthesis, characterization, and nano-bio interface were explained. In the second chapter, a novel long-term nanoparticle accumulation model was developed to understand active regulation of nanoparticle uptake, nanoparticle accumulation behavior and the impact of long-term exposure on cellular machineries (e.g. ER stress). In the third chapter, the role of ketone body betahydroxybutyrate ( $\beta$ OHB) generated by a metabolic enzyme, hydroxymethylglutaryl CoA synthase 2 (HMGCS2), on intestinal stem cell maintenance and regeneration after radiation injury was investigated. Consequences of  $\beta$ OHB depletion in intestine were rectified by oral

delivery of PLGA-encapsulated and oligomer forms of  $\beta$ OHB. The last chapter, acidic epitopes of enamel proteins (e.g. amelogenin) were integrated into self-assembling peptides to remineralize eroded enamel. Overall these studies show potential of nature-inspired engineered nanomaterials in vast range of biomedical and regenerative medicine applications.

*Keywords: nanoparticle; toxicity; cell-nanomaterial interactions; gold nanoparticles; nanoparticle accumulation; organoid; HMGCS2; beta hydroxybutyrate; small intestine; oral ketone delivery; mineralization; enamel; self-assembling peptide*

# ÖZET

## BİYOMEDİKAL VE YENİLEYİCİ TIP UYGULAMALARINDA KULLANILAN NANOMALZEMELERİN MOLEKÜLER SEVİYEDE İNCELENMESİ

Nuray Gündüz

Malzeme Bilimi ve Nanoteknoloji, Doktora

Tez Danışmanı: Çağlar Elbükten

Tez Eş Danışmanı: Ayşe Begüm Tekinay

Tez Eş Danışmanı: Ömer H. Yılmaz

Nisan, 2019

Moleküler mekanizmalar, minimalist yaklaşım olan aşağıdan-yukarıya yöntemiyle etkili nanomalzemelerin sentezi için ilham kaynağıdır. Biyomakromoleküllerin fonksiyonel biyo-fizikokimyasal özelliklerini taklit etmek, biyomedikal ve rejeneratif tıp uygulamalarında kullanılan nanomalzemelerin tasarımı ve sentezi için yeni bilgiler verebilir. Bu tezde, rasyonel tasarımlı nanomalzemeler ve bunların oral keton iletimi, biyomeralizasyon gibi biyomedikal uygulamaları ve biyomedikal uygulamalarda oluşabilecek uzun vadeli potansiyel toksisiteleri gibi incelenmiştir. Birinci bölümde, nanomalzemenin tasarımı, sentezi, karakterizasyonu ve nano-biyo arayüzü gibi temel kavramlar açıklanmıştır. İkinci bölümde, nanoparçacık alımının aktif düzenlenmesini, hücrelerdeki nanoparçacık birikim davranışını ve uzun süreli maruz kalmanın hücresel makineler üzerindeki etkisini (örneğin, ER stresi) anlamak için yeni bir uzun vadeli nanoparçacık birikim modeli geliştirilmiştir. İkinci bölümde, metabolik bir enzim, hidroksimetilglütaryl CoA sentaz 2 (HMGCS2) tarafından üretilen keton molekülünün betahidroksibutiratin ( $\beta$ OHB), bağırsak kök hücrelerin devamlılığı ve radyasyon hasarı sonrasında bağırsak rejenerasyonu üzerindeki rolü araştırıldı. Bağırsakta  $\beta$ OHB

tükenmesinin sonuçları,  $\beta$ OHB enkapsüle edilmiş PLGA nanoparçacıklar ve  $\beta$ OHB oligomer formlarının oral yoldan verilmesi ile kısmen düzeltildi. Son bölüm, enamel proteinlerinin asidik epitoplari (örneğin, amelogenin) kendiliğinden birleştirilen peptitlere entegre edildikten sonra aşınmış enamelin biyomineralizasyonunda kullanıldı. Genel olarak, bu çalışmalar çok çeşitli biyomedikal ve rejeneratif tıp uygulamalarında kullanılan doğadan ilham alan nanomalzemelerin potansiyelini göstermektedir.

*Anahtar kelimeler: nanoparçacık; toksisite; hücre-nanomalzeme etkileşimi; altın nanoparçacıklar, nanoparçacık birikmesi; organoid; HMGCS2; ince bağırsak; beta hidroksibutirat; ağızdan keton dağıtımı; mineralleşme; enamel; kendiliğinden bir-araya gelen peptit amfifil*

# ACKNOWLEDGEMENT

I would like to thank my advisor Dr. Çağlar Elbüken his support, encouragement and sincere talks about science and life. I would like to express my gratitude to my thesis co-advisor and previous advisor Dr. Ayşe Begüm Tekinay for her scientific knowledge, guidance, encouragement and support throughout my PhD thesis studies. She has gone beyond being only an advisor because her encouragement and advices helped me to understand and improve myself. I would like to thank my co-advisor Dr. Ömer H. Yılmaz for hosting me in his lab at Koch Institute of Massachusetts Institute of Technology and opening a new page in my scientific career with his wisdom and energy. I would also like to acknowledge my jury members Dr. Melih Önder Babaoğlu for his kind personality and scientific feedbacks since qualification exam, Dr. Dönüş Tuncel for her contributions to my thesis, Dr. Bahar Değirmenci Uzun for giving hope and encouragement as a young women scientist, Dr. Sreeparna Banarjee for her contributions to my thesis. I would like to thank Dr. Mustafa Özgür Güler for his scientific support during first three years of my PhD.

I would like to acknowledge my financial supports and funding. I will not able finish without support of TUBITAK (The Scientific and Research Council of Turkey) and Bilkent University. I got two different PhD scholarships from TÜBİTAK; BİDEB 2211-A for PhD and 2214-A for research during my last year of PhD at MIT. In addition to scholarships, TUBITAK also supported research in Chapter 2 with 213M001 grant. I would like to acknowledge Bilkent/UNAM scholarship support in transition times.

Bilkent University has been my home with all the unforgettable memories for the past six years. I need to acknowledge professors who worked hard for the

establishment of National Nanotechnology Research Center which plays an important role in the advancement of science and technology in Turkey and training of many students like me. There are also special professors who are student-friendly as Dr. Engin Durgun and Dr. Seymour Jahangirov. Thank you both for not behaving students as homo erectus! Duygu Kazancı is also exceptional person in UNAM administrative team with her big smile. My friends from dorm Kevser Özdemir, Norizan Sulong and many others shared their time, food, and energy with me.

I would like to express my special thanks to Ceren Yaşa (Garip), Dr. Hakan Ceylan, Dr. Rashad Mammadov, Dr. Chia-Wei Cheng for their fruitful collaboration. Together, we pursued interesting scientific questions, which we managed / will manage to publish in high quality journals.

I would like to express my thanks to my previous lab members Oğuz Tuncay, Özge Uysal, İdil Uyan, Dr. Alper Devrim Özkan, Dr. Ahmet Emin Topal, Nurcan Haştar, Dr. Elif Arslan, Fatma Begüm Dikeçoğlu, Canelif Yılmaz, Dr. Ruslan Garifullin, Dr. Berna Şentürk, Dr. Gülcihan Gülseren, Dr. Gülistan Tansık, Dr. M. Aref Khalily, Dr. Melis Şardan, Dr. Gözde Uzunallı, Dr. Özlem Erol, Dr. Ashif Shaikh, Dr. Seher Yaylacı, Dr. Ayşe Özdemir, Gökhan Günay, Murat Kılınç, Mevhibe Geçer, Aygül Zengin, Meryem Hatip, Özüm Şehnaz Günel, Çağla Eren Çimenci, Öncay Yaşa, Hapi Hari Susapto, Zeynep Orhan, Seren Hamsici, Merve Şen, Fatih Yergöz, Burak Demircan, Dr. Melis Göktaş, Yasin Tümtaş, Dr. Didem Mumcuoğlu, Mustafa Beter, Şehmus Tohumeken, Burak Demircan for creating such big and instructive working environment. I would like to express my special thanks to Elbüken lab members for their sincere friendships in my last few months. Especially, Abtin Saateh was with me in my difficult times.



None of these studies can be done without immense technical helps and trainings from UNAM staffs; Zeynep Erdoğan in LC-MS and HPLC, Dr. Gökçe Çelik in ICP-MS and Mustafa Güler in TEM, MIT histology core facility staffs; Kathleen Corner, Charlene Condon and Michael Brown, and Sven Holder for sections, H&E and AB&PAS staining, MIT flow cytometry core facility staffs; Glenn Paradis, Michael Jennings and Mervelina Saturno-Condon, DCM core facility staffs.

UNAM became a big family in past 6 years with Buket Gültekin (Bukim), Dr. Yelda Ertaş, Dr. Aslı Celebioğlu, Zehra İrem Yıldız, Dr. Zeynep Ergül Ülger, Said Ergöktaş, Abdüllatif Önen, Fatma Göksemin Şengül, Talha Masood Khan, Dr. Aydan Yeltik, Dr. Burak Güzel Türk, Türkan Gamze Ulusoy Ghobadi, Dr. Yusuf Keleştemur, Dr. Peter Deminskyi, Suna Temiz, and many others I could not write their names here.

I also would like to thank my dear friends Emine Kazanç, Tuba Özdemir Sancı, Zeynep Öztürk and Şeyma Türkseven for their long-lasting friendships and supports since college years (2008-).

I would like to thank MIT dudes as well. Yılmaz Lab members; Elizabeth Galoyan for administrative works and her sincere smile almost every morning, Kerry Kelley for managing lab and taking care of me like mom whenever I need, Dr. Chia-Wei Cheng, Dr. Miyeko M. Mana, Dr. Shinya Imada, Dr. Wen Zhou, Dr. Heaji Shin, Dr. Amanda M. Hussey, H. Dorukhan Bahçeci, Ameena Iqbal, Surya Tripathi, Dr. Jonathan Braverman, Dr. George Eng, Dr. Fang Wang, Dr. Gizem Çalıbaşı Koçal, Dr. Jatin Roper, and Dr. Mohammad Almeqdadi for helping in experiments, guiding, being home and family in US. Dr. Jette Lengefeld from Angelika Amon Lab was very nice and supportive all the time whenever I asked question. MIT TSA (Turkish Student Association) friends: Eren Can Kızıldağ (Yoldaş), Dr. Renin Hazan, Dr. Murat-

Mihriban Yıldırım, Ulugbek Barotov for friendship in good-bad days and outdoor activities.

This part will cover special thanks: Rashad Mammadov who is the most inspirational person in my life, I feel more myself when I am talking with him. I did not hear even single word from him implying judgement or discouragement. Together we are talking about life, science, human behavior, psychology and so many topics like ‘difference of two realities: fact and truth’, ‘fear of missing out’, ‘fame and ethic’, ‘anxiety of authenticity’, ‘identity’, ‘freedom in university’ which are significantly helping me to understand my inner person and meaning of the life. I wish I knew him earlier and have more time to talk. I strongly believe that he will be a great mentor to his students and his daughter Gülnare. Maybe we could not have enough time to share everything due to heavy experimental schedules, but Miyeko Mana helped me to believe myself again. She is also a good role model of not giving up (go-girl role model is uploading). Elif Duman is another hero of learning following terms without feeling guilty: how to give self-compassion in difficult times, toxic relationships and so many psychological things. I wish she can touch more people. Chia-Wei Cheng is one of the weird people (now you’re in the list) I will never ever understand but I can say she has something inside more than she shows. Thank you for teaching, mentoring, advising and showing the realities of academia.

Finally, I would like to express my most sincere gratitude to my family especially my mom Fatma Gündüz who taught me how to be brave against failures in the life and my dad Ramazan Gündüz who taught setting a goal and perseverance even it costs your whole life. My sisters; Hatice Gündüz, Zübeyde Dülger and Gülay Gündüz support and compensate my anxiety with their love and trust. Mustafa Dülger, brother

in-law, however he became a real brother by listening, advising, caring my problems after joining our family. I want to express my undefinable feelings to my nephews, M. Hakan Dülger and Furkan Dülger, who are stem cells of our family and change my mood easily even with a single word. Sometimes, they push me to work harder by reminding our responsibilities to the next generations.

# CONTENTS

<b>ABSTRACT .....</b>	<b>iii</b>
<b>ÖZET .....</b>	<b>v</b>
<b>ACKNOWLEDGEMENT .....</b>	<b>vii</b>
<b>CONTENTS .....</b>	<b>xii</b>
<b>LIST OF FIGURES.....</b>	<b>xvi</b>
<b>LIST OF TABLES.....</b>	<b>xix</b>
<b>ABBREVIATIONS.....</b>	<b>xx</b>
<b>CHAPTER 1 .....</b>	<b>1</b>
1.1 Design, Synthesis and Characterization of Engineered Nanomaterials .....	1
1.2 The Nano-Bio Interface and Intracellular Activity .....	6
1.3 Short- and Long-term Risk Assessments of Engineered Nanomaterials .....	11
1.4 Selected Applications of Engineered Nanomaterials .....	14
1.4.1 Oral Drug Delivery.....	14
1.4.2 Synthetic Enamel Biomineralization.....	16
<b>CHAPTER 2 .....</b>	<b>18</b>
<b>2.1 The objective .....</b>	<b>18</b>
<b>2.2 Introduction.....</b>	<b>19</b>
<b>2.3 Experimental Section .....</b>	<b>22</b>

2.3.1 Chemicals and Reagents .....	22
2.3.2 Synthesis of Gold Nanoparticles .....	23
2.3.3 UV-Vis Spectroscopy .....	23
2.3.4 Transmission Electron Microscopy .....	24
2.3.5 Dynamic Light Scattering (DLS) and Zeta Potential Measurements .....	24
2.3.6 Cell Culture and Maintenance .....	24
2.3.7 Cell Viability and Proliferation .....	25
2.3.8 Imaging of AuNPs within Cells by Silver Staining .....	27
2.3.9 Determination of Cellular Internalization Pathway of AuNPs .....	28
2.3.10 In Vitro Long-term Accumulation Model .....	29
2.3.11 Quantification of AuNPs within Cells by ICP-MS for Accumulation Analysis .....	30
2.3.12 Quantification of AuNPs in Medium by ICP-MS for Exocytosis Analysis .....	31
2.3.13 Imaging of HUVECs with Fluorescent Molecules for Endocytosis Analysis .....	32
2.3.14 Determination of Cellular Stress Levels by qRT-PCR and Dichlorofluorescein Assay .....	32
2.3.15 Statistical Analysis .....	35
<b>2.4 Results and Discussion .....</b>	<b>35</b>
2.4.1 Characterization of AuNPs .....	35
2.4.2 Cytotoxicity and internalization of AuNPs .....	38
2.4.3 <i>In vitro</i> long-term accumulation of AuNPs .....	42
2.4.4 Endocytosis and exocytosis behavior of AuNP accumulated cells .....	44

2.4.5	Determination of the cellular stress during long-term accumulation .....	47
<b>2.5</b>	<b>Conclusion .....</b>	<b>52</b>
<b>CHAPTER 3</b>	<b>.....</b>	<b>54</b>
<b>3.1</b>	<b>The objective .....</b>	<b>54</b>
<b>3.2</b>	<b>Introduction.....</b>	<b>55</b>
<b>3.3</b>	<b>Experimental methods .....</b>	<b>59</b>
3.3.1	Mice and treatments .....	59
3.3.2	$\beta$ -hydroxybutyrate ( $\beta$ OHB) measurements.....	61
3.3.3	Crypt isolation and culturing .....	61
3.3.4	Immunohistochemistry, Immunofluorescence and in situ Hybridization .	64
3.3.5	$\beta$ -hydroxybutyrate encapsulated PLGA nanoparticle synthesis .....	66
3.3.6	$\beta$ -hydroxybutyrate oligomer synthesis .....	66
<b>3.4</b>	<b>Results and Discussion .....</b>	<b>69</b>
3.4.1	Ketogenic enzyme HMGCS2 is enriched in intestinal stem cells.....	69
3.4.2	Loss of <i>Hmgcs2</i> attenuates ISC number and function .....	73
3.4.3	Loss of <i>Hmgcs2</i> impairs intestinal regeneration after irradiation damage	77
3.4.4	Loss of <i>Hmgcs2</i> skews ISC differentiation towards secretory lineage .....	78
3.4.5	Exogenous $\beta$ OHB rescues loss of <i>Hmgcs2</i> .....	79
<b>3.5</b>	<b>Conclusions.....</b>	<b>86</b>
<b>CHAPTER 4</b>	<b>.....</b>	<b>88</b>
<b>4.1</b>	<b>The objective .....</b>	<b>88</b>
<b>4.2</b>	<b>Introduction.....</b>	<b>89</b>

<b>4.3 Experimental Methods.....</b>	<b>92</b>
4.3.1 Chemical and Reagents .....	92
4.3.2 Synthesis and Purification of Peptides .....	92
4.3.3 Transmission Electron Microscopy.....	94
4.3.4 Circular Dichroism .....	94
4.3.5 Enamel Remineralization Assay .....	95
4.3.6 <i>In vitro</i> Cell Viability and Proliferation .....	97
<b>4.4 Results and Discussions.....</b>	<b>98</b>
4.4.1 Design and characterization of the mineralizing peptides.....	98
4.4.2 Enamel regeneration with self-assembling peptides .....	101
4.4.3 Biocompatibility of the mineralizing peptide .....	102
<b>4.5 Conclusion .....</b>	<b>107</b>
<b>CHAPTER 5 .....</b>	<b>108</b>
<b>CONCLUSION &amp; FUTURE PERSPECTIVES .....</b>	<b>108</b>
<b>BIBLIOGRAPHY.....</b>	<b>110</b>
<b>APPENDIX A .....</b>	<b>119</b>
<b>APPENDIX B.....</b>	<b>120</b>

## LIST OF FIGURES

Figure 1.1 Beyond the fold: DNA origami shapes and emerging biomedical applications. ....	4
Figure 1.2 Uptake mechanisms and the intracellular transport of ENMs.....	7
Figure 1.3 Trends in the development of nanomedicines.....	12
Figure 1.4 Schematic diagram of oral insulin delivery methods to different site of body. ....	15
Figure 1.5 The peptide-guided remineralization in carious enamel lesion.....	17
Figure 2.1 Biomedical application of gold nanoparticles after functionalization. ....	21
Figure 2.2 Schematic illustration of citrate-stabilized AuNPs synthesis.....	23
Figure 2.3 Schematic illustration of the long-term AuNP accumulation model.....	30
Figure 2.4 Chemical structure and working principle of DCF assay. ....	34
Figure 2.5 Size and distribution characterizations of AuNPs by TEM and DLS.....	36
Figure 2.6 Colloidal stability and protein corona analysis via UV-vis and zeta-potential.....	37
Figure 2.7 Cytotoxicity and protein corona effects analyses. ....	39
Figure 2.8 Silver enhancement staining of the AuNPs in HUVECs cultured with 10% FBS DMEM. ....	41
Figure 2.9 Silver enhancement staining of the AuNPs in HUVECs cultured with 5% FBS DMEM. ....	42
Figure 2.10 In vitro long-term accumulation of AuNPs in HUVECs. ....	43
Figure 2.11 Cellular uptake of AuNPs. ....	45



Figure 2.12 Uptake profile of the fluorescent-labeled compounds in the AuNP accumulated and non-accumulated cells.....	46
Figure 2.13 Exocytosis behavior of HUVECs during long-term accumulation of the AuNPs.....	47
Figure 2.14 Cellular stress response to long-term accumulation of AuNPs.....	49
Figure 2.15 Cellular response to long-term accumulation of AuNPs.....	51
Figure 3.1 The anatomy of the small intestinal epithelium. ....	57
Figure 3.2 Schematic of the “knockout-first” conditional allele which is generated with gene trapping strategy. ....	60
Figure 3.3 Oligo-βOHB synthesis steps. ....	68
Figure 3.4 HMGCS2 is enriched in <i>Lgr5</i> <sup>+</sup> intestinal stem cells. ....	71
Figure 3.5 Organoid-forming potential of flow-sorted <i>Hmgcs2</i> -lacZ <sup>-</sup> and <i>Hmgcs2</i> -lacZ <sup>+</sup> crypt epithelial cells.....	72
Figure 3.6 Loss of <i>Hmgcs2</i> compromises ISC self-renewal and organoid-forming capacity. ....	75
Figure 3.7 Loss of <i>Hmgcs2</i> compromises ISC self-renewal.....	76
Figure 3.8 Loss of <i>Hmgcs2</i> impairs intestinal regeneration after irradiation damage. ....	78
Figure 3.9 Loss of <i>Hmgcs2</i> skews ISC differentiation towards secretory lineage.....	79
Figure 3.10 βOHB rectifies <i>Hmgcs2</i> -loss in organoids.....	82
Figure 3.11 Oral administration of βOHB improved the regeneration capacity of <i>Hmgcs2</i> -KO mice intestine after irradiation challenge. ....	85
Figure 4.1 Schematic of experimental demineralization and remineralization on tooth enamel.....	91

Figure 4.2 Chemical structures, liquid chromatography and mass spectroscopy results of peptides. ....	99
Figure 4.3 Characterization of the self-assembling peptides and the mechanism of self-assembly.....	101
Figure 4.5 Dose-dependent cytotoxicity in HGFs after 24 h. ....	103
Figure 4.4 Hydroxyapatite formation on demineralized tooth surfaces. ....	104
Figure 4.6 Viability of HGFs treated with mineralizing peptides at 48 h. ....	105
Figure 4.7 Proliferation of HGFs treated mineralizing peptides at 24 h. ....	106

# LIST OF TABLES

Table 1. 1 Common techniques for synthesis of nanomaterials.....	2
Table 1. 2 Common analytical techniques for characterization of physiochemical properties of nanomaterials.....	5
Table 2. 1 Chemical inhibitors used for the inhibition of the endocytosis pathway of cells.....	29
Table 2. 2 Primers used in RT-PCR and qRT-PCR. ....	34
Table 3. 1 Cell labeling antibody cocktail for sorting ISCs and Paneth cells from crypts. ....	63
Table 4. 1 Reagents for preparation of 1X simulated body fluid (pH 7.40 , 1L).....	96

## ABBREVIATIONS

<b>ANOVA</b>	Analysis of variance
<b>AuNPs</b>	Gold nanoparticles
<b>BSA</b>	Bovine serum albumin
<b>CD</b>	Circular dichroism
<b>DCF</b>	2',7'-Dichlorofluorescein
<b>DCM</b>	Dichloromethane
<b>DLS</b>	Dynamic Light Scattering
<b>DMEM</b>	Dulbecco's modified Eagle's medium
<b>DMF</b>	Dimethylformamide
<b>DMSO</b>	Dimethyl sulfoxide
<b>ENMs</b>	Engineered nanomaterials
<b>FBS</b>	Fetal bovine serum
<b>FDG</b>	Fluorescein di- $\beta$ -D-galactopyranoside
<b>GAPDH</b>	Glyceraldehyde 3-phosphate dehydrogenase
<b>HA</b>	Hydroxyapatite
<b>HAuCl<sub>4</sub></b>	Gold (III) chloride trihydrate
<b>HGFs</b>	Human gingival fibroblasts
<b>HMGCS2</b>	Hydroxymethylglutaryl CoA synthase 2
<b>HPLC</b>	High-performance liquid chromatography
<b>HUVEC</b>	Human umbilical vein endothelial cell
<b>ICP-MS</b>	Inductively coupled plasma mass spectroscopy
<b>ISCs</b>	Intestinal stem cells
<b>LC-MS</b>	Liquid chromatography mass spectroscopy
<b>Lgr5</b>	Leucine rich repeat-containing G-protein coupled receptor
<b>MTT</b>	4, 5-dimethylazol-2-yl)-2, 5-diphenyl-tetrazolium bromide
<b>OLFM4</b>	Olfactomedin 4
<b>PBS</b>	Phosphate buffered saline
<b>P/S</b>	Penicillin/streptomycin
<b>PLGA</b>	Poly (lactic-co-glycolic acid)
<b>ROS</b>	Reactive oxygen species
<b>qRT-PCR</b>	Quantitative real-time polymerase chain reaction
<b>SBF</b>	Simulated body fluid
<b>s.e.m</b>	Standard error of mean
<b>SEM</b>	Scanning electron microscopy
<b>TAM</b>	Tamoxifen
<b>TCP</b>	Tissue culture plate
<b>TEM</b>	Transmission electron microscopy
<b>UV-Vis</b>	Ultraviolet visible spectroscopy
<b>XRT</b>	Ionizing radiation
<b>7AAD</b>	7-Aminoactinomycin D

# CHAPTER 1

## 1 INTRODUCTION

Some parts of this chapter were published as a partial content of the following publication:

*Gunduz, N., Arslan, E., Guler, M. O., Tekinay, A. B. Safety of Nanomaterials: Therapeutic Nanomaterials, John Wiley & Sons Inc., 271-298, 2016 [1].*

### 1.1 Design, Synthesis and Characterization of Engineered Nanomaterials

Nanotechnology is an interdisciplinary field having intersection with different fields to develop new materials with new functionalities for various applications. The nanoscale materials are defined as manufactured materials having at least one dimension in the range of 1 to 100 nanometers (nm) by the U.S. National Nanotechnology Initiative (NNI). In addition, there are also nanoscale materials either naturally occurring as seen in magnetotactic bacteria [2] which might be the focus of developing non-toxic smart nanomaterials or unintentionally-produced during industrial process and natural events [3] which are the focus of occupational, health and safety risk assessments. The intentionally-manufactured nanomaterials are also called as engineered nanomaterials which are organized into different categories based on dimension, organic / inorganic or structure. However, general classifications made based on materials used in synthesis; (i) carbon-based materials (e.g. carbon nanotubes), (ii) metal-based materials (e.g. nanogold), (iii) dendrimers (branched nanosized polymers), (iv) composites (two different nanomaterials). The intentionally-

manufactured nanomaterials with controlled chemical, physical, and biological properties are usually produced by two approaches: top-down and bottom-up. Table 1.1 lists some of the commonly used top-down and bottom-up techniques.

**Table 1. 1 Common techniques for synthesis of nanomaterials.**

<b>Top-down</b>	
	Milling (e.g. mechanical)
	Etching (e.g. plasma etching)
I. Solid phase techniques:	Sputtering
	Laser ablation
	Lithography (e.g. photolithography)
II. Aerosol-based techniques	Electrospraying
III. Liquid-phase techniques	Electrospinning
<b>Bottom-up</b>	
IV. Vapor-phase techniques	Deposition techniques (e.g. thermal chemical vapor deposition)
	Chemical vapor condensation (e.g. molecular beam epitaxy)
Solution-phase techniques	Chemical reduction
	Sol-gel
Self-assembly / Self-organization techniques	Self-assembling peptides
	DNA origami

The top-down approaches tailor bulk materials into smaller materials with specific shape and size by using high-tech tools like crushing, milling or grinding. Besides advantages, top-down methods have problems including non-uniform synthesis and imperfections, which might affect the physical properties and surface chemistry of nanomaterials.

The bottom-up approaches utilize small molecular building blocks as atoms or molecules to form more complex and higher-scale nanometer-sized materials via

chemical reactions or self-assembly. Richard Feynman, the father of Nanotechnology, pointed in his famous speech that nature has been working with materials at the levels of atoms and molecules for millions of years. Plenty of nanostructures in nature especially in biological organisms are generated by bottom-up approaches, such as a typical ribosome (20-30 nm in diameter), collagen fibers of extracellular matrix (1.5 nm in diameter and 300 nm in length). The design and synthesis approach chosen for engineered nanomaterials may heavily influence their functionality and biocompatibility. Therefore, engineered nanomaterials with controlled functionalities can best be manufactured by bottom-up approaches through inspiration from sophisticated natural synthesis techniques. Self-assembly / self-organization techniques are superior to chemical reduction / molecular chemistry techniques due to the structural and dynamic control over material formation. Self-assembly mostly utilizes supramolecular chemistry where molecular chemistry information directs noncovalent interactions, such as dispersion forces, hydrogen bonds, and hydrophobic interactions [4]. In recent years, self-assembly improved functional nanomaterial synthesis in nanotechnology. DNA origami is a prime example showing promise to produce three dimensional nanomaterials for a variety of applications (depicted in Figure 1.1) after a decade of its debut [5, 6].

Observation and characterization are essential for analyses and confirmation of different and additional properties of nanomaterials after synthesis. Some parameters including shape, size, aggregation / agglomeration, surface chemistry, surface modification, and crystal structure are widely used to characterize nanomaterials. In addition to the synthesis of nanomaterials, nanotechnology also improves invention and development of sophisticated tools / techniques for nanocharacterizations.

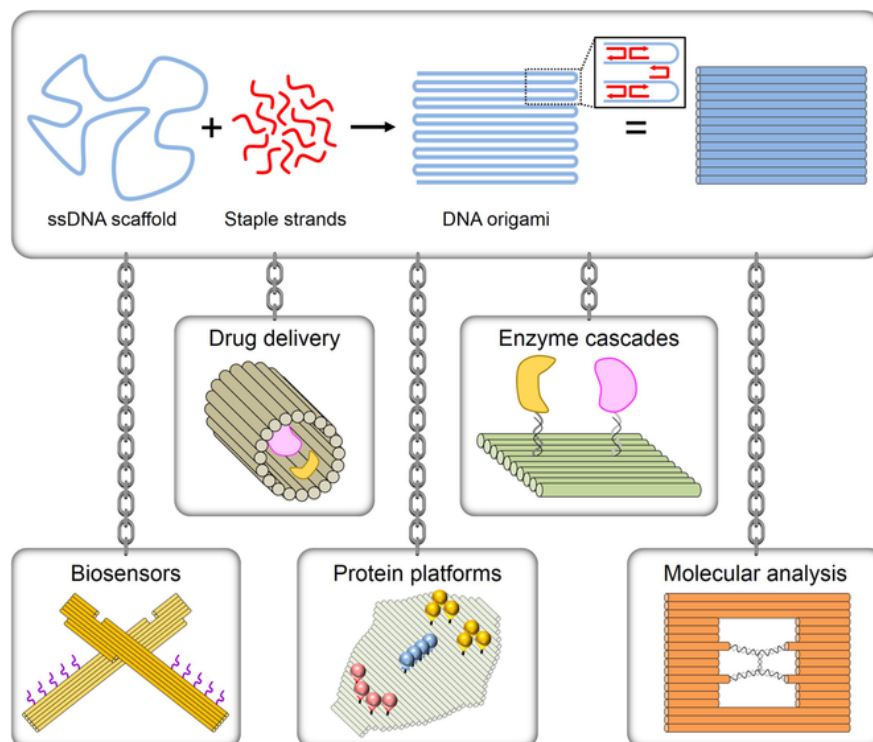


**Figure 1.1 Beyond the fold: DNA origami shapes and emerging biomedical applications.** Origami construction and examples of applications in drug delivery, enzymes cascades, biosensors, protein arrangement, and molecular analysis. Reprinted with the permission from John Wiley and Sons [6].

Many methods have been used for characterization, analysis and evaluation of nanomaterials, including techniques in optical and electron microscopy, scattering, surface scanning, circular dichroism, mass spectroscopy, X-ray spectroscopy, zeta potential, thermal techniques, and mechanical and rheological techniques [7]. Some of these tools and techniques are revised in Table 1.2 (Table was created based reference [7]) and were used in characterization and analyses of engineered nanomaterials described in this thesis.



**Table 1. 2 Common analytical techniques for characterization of physiochemical properties of nanomaterials.**

<b>Imaging Techniques</b>	<b>Characterization parameters</b>
Electron microscopy: Scanning electron microscopy (SEM) Transmission electron microscopy (TEM)	Size, shape, structure, morphology and elemental analysis when coupled with Energy dispersive X-ray analysis (EDX)
Scanning probe microscopy: Scanning tunneling microscope (STM) Atomic force microscope (AFM)	Size, shape, structure, morphology and atomic scale resolution
<b>Spectroscopy Techniques</b>	<b>Characterization parameters</b>
UV-Vis absorption and emission:	Detection of chemical bonds
Vibrational Spectroscopies: Fourier Transform Infrared Spectroscopy (FTIR) Raman Spectroscopy	Chemical composition analysis
X-ray photoelectron spectroscopy (XPS)	Chemical composition
Circular dichroism	Secondary structure
Mass spectroscopy techniques: High-performance liquid chromatography (HPLC) Inductively coupled plasma mass spectroscopy (ICP-MS)	Detection, separation, and quantification Elemental analysis
<b>Scattering Techniques</b>	<b>Characterization parameters</b>
X-Ray diffraction techniques: XRD spectra Small angle X-ray scattering (SAXS) Small-angle neutron scattering (SANS)	Crystal structure, phase, and average particle size
Dynamic Light Scattering (DLS)	Size distribution analyses in liquid phase
Zeta potential analysis	Surface charge analysis in aqueous solutions or suspensions

## **1.2 The Nano-Bio Interface and Intracellular Activity**

The intracellular activity and nano-bio interface are important for biological applications and toxicity of ENMs. The biological milieu plays an important role during cell-nanomaterial interactions. Lipids and proteins cover the surfaces of ENMs immediately after their introduction into biological systems [8] and this effect, in tandem with other physicochemical properties, affects the entry mechanisms of ENMs in all cell types. The localization and intracellular fate of ENMs depend on their internalization pathways, which in turn are affected by the surface chemistry [9], size [10] and shape [11-13] of ENMs, in addition to the biological milieu [14], cell type [15, 16] and other factors. Internalization pathways and interactions at the cell-ENM interface are dependent on the biomolecular corona, which partially blocks the bare material surface from interacting with the cell membrane and therefore reduces the surface free energy of ENMs, resulting in a decrease in their cellular uptake [17]. Other studies have also reported that the thickness of the bio-corona, as directed by changing serum concentrations, may affect the cellular uptake of the ENMs [14].

After cellular entry, the ENMs are transported within the cell and may concentrate in various organelles. However, owing to the lack of information regarding the intracellular transport mechanisms used by the ENMs, there is no uniform consensus regarding the precise series of events that occur following internalization. Thus, the intracellular transport of the ENMs cannot be generalized, especially in view of the structural and biochemical variability of the ENMs themselves [18]. Once inside the cell, ENMs may interact with cellular compartments such as the cytosol, endosome, mitochondria, lysosome, nucleus and Golgi apparatus (Figure 1.2).

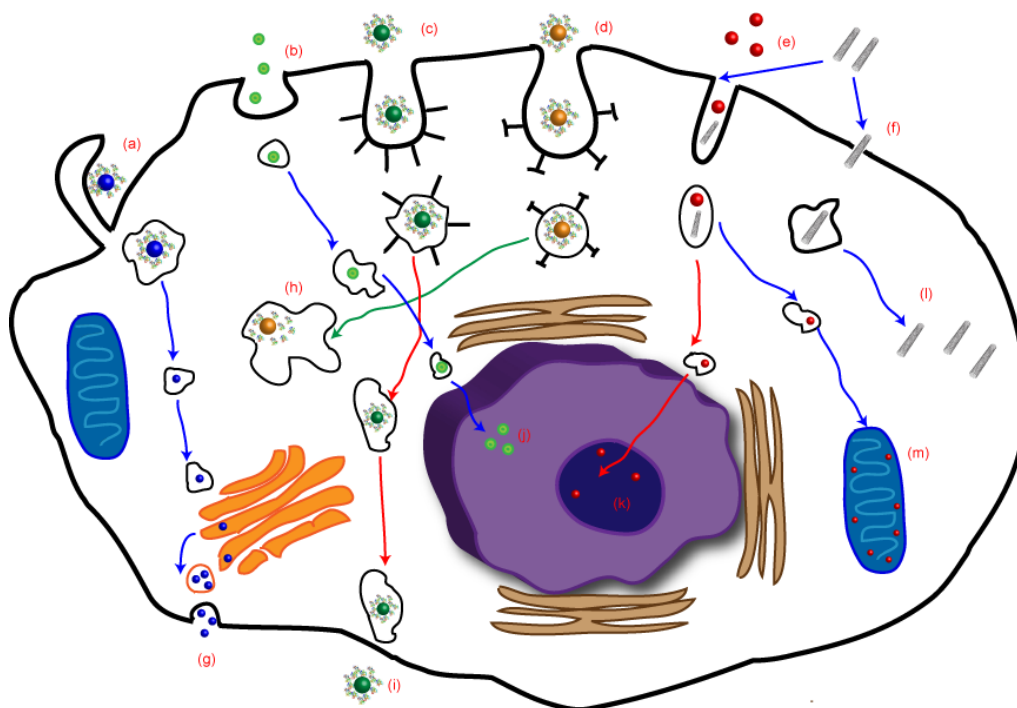


**Figure 1.2 Uptake mechanisms and the intracellular transport of ENMs.** Uptake may occur through micropinocytosis (a), pinocytosis (b), caveolin-mediated endocytosis (c), clathrin-mediated endocytosis (d), unknown endocytic pathways (e) or diffusion/penetration (f). After cellular entry, the ENMs may localize into different organelles and cellular compartments. ENMs that enter into the Golgi apparatus can cause organelle damage and/or leave the cell via vesicles involved in the regular secretion system (g). The ENMs remaining in early endosomes move slowly along cytoskeletal elements, fuse with late endosomes and finally accumulate in the lysosome (h), nucleus (j), nucleolus (k) and mitochondria (m). In addition to these possible endpoints, the ENMs can also accumulate in the cytoplasm (l) after escaping from late endosomes or lysosomes. Ultimately, the ENMs can be excreted from the cell by transcytosis (i). Reproduced from *Safety of Nanomaterials: Therapeutic Nanomaterials*, John Wiley & Sons Inc., 271-298, 2016 [1].

The cytoskeleton is another common target for the cytotoxic ENMs, and plays significant roles in cellular events such as intracellular transport, cell division and motility, all of which can be disrupted by nanoparticle activity. It has been reported that the aggregation state of AuNPs strongly influences their toxicity against human

dermal fibroblast cells: Nanoparticle clusters were four-fold more toxic than their non-aggregated counterparts, and triggered the disruption of F-actin fibers. In addition, the aggregation state of these nanoparticles were closely related to their surface chemistry and the conditions under which the NPs were introduced to the biological milieu [9]. Despite their lack of acute cytotoxicity, single-walled carbon nanotubes (SWCNTs) were also shown to greatly reduce the proliferation of HeLa cells, which was attributed to actin-related cell division defects [19]. Similar effects were observed in neuronal progenitor cells and endothelial cells treated with iron oxide nanoparticles, resulting in concentration-dependent alterations in cellular physiology. High levels of iron oxide nanoparticles affected the actin cytoskeleton through the formation and maturation of focal adhesion complexes (FACs) and resulted in a reduction in cell proliferation [20]. ENMs might also localize in other organelles after escaping from endosomes: Rhodamine-loaded PLGA (polylactic-co-glycolic acid) NPs, for example, were reported to localize in various intracellular compartments such as the Golgi apparatus, cytosol, and endoplasmic reticulum [21].

The mitochondria are another potential endpoint for ENM transport, as the high membrane potential (approximately -200 mV) of the mitochondria would strongly attract positively-charged nanoparticles [22]. The inner membrane of the mitochondrion might be especially suitable for the accumulation of ENMs, due to its hydrophobic, anionic and high-membrane potential characteristics. Mitochondriotropic moieties have been developed to exploit this property for mitochondrial gene therapy and chemotherapy applications. The accumulation or localization of the ENMs inside the mitochondria can be accomplished through surface functionalization via triphenylphosphonium (TTP), which is a mitochondriotropic

moiety. The localization of TPP-conjugated ENMs inside the mitochondria has also been confirmed by experimental reports. It has been demonstrated that polystyrene (PS) nanoparticles functionalized with both TPP and poly-L-lysine (PLL) localize in mitochondria due to the hydrophobic properties of the TPP [23]. Doxorubicin-loaded, TPP-functionalized polyethyleneimine hyperbranched polymer (PEI) nanoparticles likewise triggered rapid and severe cytotoxicity within a few hours of incubation at low concentrations, in contrast to free doxorubicin [24]. Another study detailed the design of a multifunctional envelope-coated nano-carrier system, which consists of mesoporous silica nanoparticles (MSNs) functionalized with TPP, the antineoplastic drug topotecan (TPT) and a charge-conversional shielding layer. This system was shown to target tumor cells and initiate apoptosis through mitochondrial damage [25]. Mitochondrion-mediated apoptotic cell death was also achieved in drug-resistant breast cancer cells via nanoparticle-directed efficient subcellular localization of doxorubicin into the mitochondria [26]. The surface chemistry and size of the ENMs are important parameters for mitochondrial targeting and localization: While carboxylated PS nanoparticles with 20 nm diameters could be located in the mitochondria of different hepatocyte cell lines, the mitochondrial uptake and localizations of 200 nm diameter PS nanoparticles were limited [27].

Lysosomes can also be targeted depending on the functionalization moiety of the nanoparticles. Glycol chitosan nanoparticles decorated with hydrophobic moieties have been reported to eventually localize into the lysosome [28]. The intracellular fate of the AuNPs has also been reported in different studies: Protein coated AuNPs are generally entrapped in endosomes, but can be directed to several cellular compartments by the addition of targeting moieties such as TAT cell penetrating

peptides or a liposome coating [29, 30]. The uptake and localization of the ENMs allow these molecules to interfere with intracellular mechanisms, potentially resulting in organelle damage, membrane leakage or the production of reactive oxygen species. These effects may be medically beneficial if the ENMs are designed to specifically target cancer cells or other diseased cell types. SPIONs covalently coated with the lysosomal protein marker LAMP1 (LAMP1-SPION), for example, were used to apply mechanical stress to the lysosomes of rat insulinoma tumor cells. The activation of the SPIONs was triggered using a dynamic field generator, decreasing the sizes and numbers of the lysosomes and resulting in a corresponding increase in cellular apoptosis. The remote control of apoptosis was therefore achieved through the activation of magnetic ENMs [31].

The excretion and clearance of ENMs have been reported for a variety of materials. It should be noted that the cells themselves respond to the ENMs by activating their exocytosis mechanisms, thus extruding or degrading the ENMs at the subcellular level. The intracellular localization of the ENMs determines whether they can be exocytosed through the activity of lysosomes or the Golgi apparatus. The exocytosis of phosphate-modified mesoporous nanoparticles (P-MSNs) showed a good correlation with the rates of lysosomal exocytosis in different cell lines, which has significant implications for the development of efficient drug delivery agents [32]. The degradation of the ENMs is also a big concern for the delivery of biological cargos. Sahay et al. reported that siRNA-conjugated cationic lipid nanoparticles are eventually degraded in the lysosome [33], which is a common drawback of biodegradable ENMs utilized for gene therapy, cancer treatment or drug delivery. In addition to biodegradable ENMs, exocytosis was observed in AuNPs which are known as inert. Bartczak et al.

characterized the exocytosis trends of AuNPs functionalized with angiogenesis-inhibiting (“inhibitor”) or similar but non-inhibitory (“mutant”) peptides and made the interesting observation that mutant peptides were first exocytosed and subsequently re-uptaken and re-exocytosed from the cell, while inhibitors were progressively removed with no re-uptake [35].

### **1.3 Short- and Long-term Risk Assessments of Engineered Nanomaterials**

Advances in nanotechnology culminated new nanomaterials and some of them have entered in our daily lives as nanomedicine, photocatalyst, food additive / packaging material, personal care products, cosmetics, textile, adhesives, tissue engineering matrix, dental restoration materials, antibacterial agents, medical devices and biosensors. Among all, nanomedicine is a rapidly evolving field and is tightly regulated by authorities such as the U.S. Food and Drug Administration (FDA) and European Agency for the Evaluation of Medicinal Products (EMA). Engineered nanomaterials are designed to provide pharmacokinetic, efficacy, safety, and targeting benefits to drugs. Since 1995, at least 50 nanodrugs have received FDA-approval and are available for clinical use. Meanwhile, some of nanodrugs are in different phases of clinical trials as shown in Figure 1.3 [34, 35].

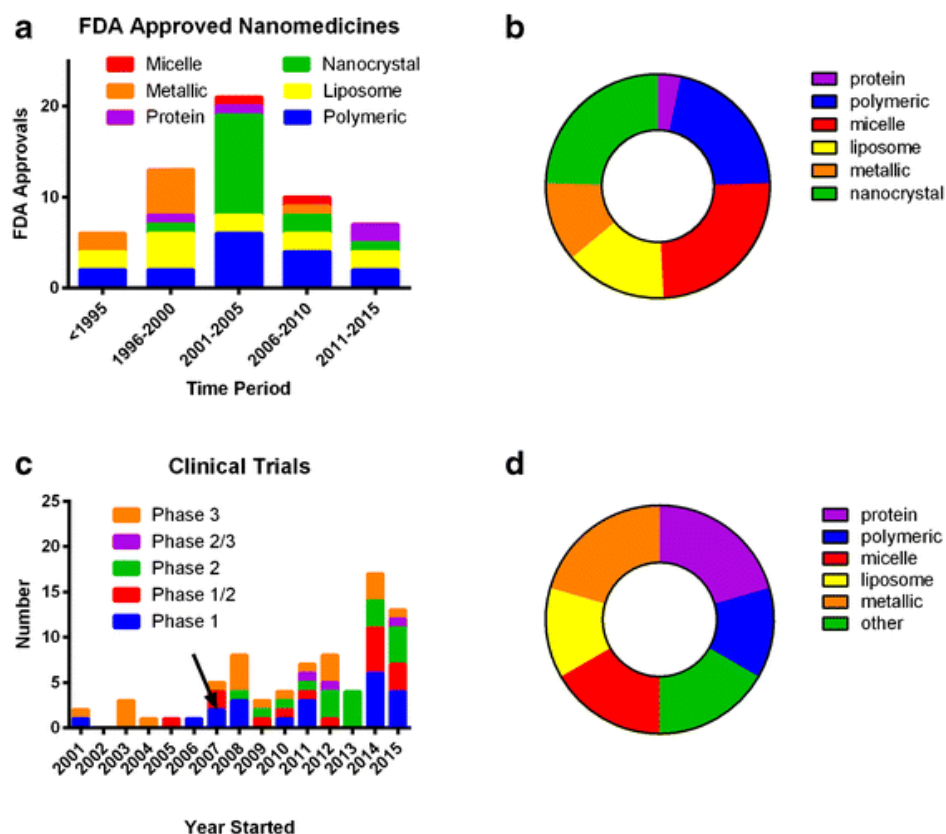


**Figure 1.3 Trends in the development of nanomedicines.** (a) FDA-approved nanomedicines stratified by category; (b) FDA-approved nanomedicines stratified by category overall; (c) clinical trials identified in clinicaltrials.gov from 2001 to 2015 with arrow indicating approximate start date of US law (FDAAA 801) requiring reporting to FDA database; (d) nanomedicines under clinical trial investigation stratified by category overall. Reprinted with permission from Springer Nature [34].

The ENMs that are intended for biomedical purposes are almost universally administered directly into the human body. Examples of such ENM designs include SPIONs and dendrimers for MRI studies; gold nanoparticles for photothermal therapy, imaging and drug and gene delivery; mesoporous silica nanoparticles (MSN) for MRI studies, drug delivery, and topical treatment; and carbon nanotubes for drug delivery, and tumor detection and treatment. These materials are promising for the development of efficient and innovative solutions for the major challenges faced by the biomedical field, especially with regards to the treatment of common disorders such as cancer,



obesity and neurodegenerative diseases. Nevertheless, as with any material intended for human use, their safety must first and foremost be investigated in sufficient detail, through both *in vitro* experiments and animal studies, before they can be administered to patients. Despite the widespread production and application of ENMs, there is a lack of satisfactory information regarding their impact on humans, animals and the ecosystem. Exposure to the ENMs may directly or indirectly cause detrimental effects on the human health. ENMs can be introduced to the human body through inhalation, ingestion, dermal penetration or injection, either unintentionally or through the course of an ENM-based therapy [41]. As with any foreign material, the ENMs may trigger adverse effects following their administration. As such, the biocompatibility, biodistribution, biodegradation, excretion and acute and long-term toxicities of the ENMs must be carefully assessed before their use in clinical trials through short- and long-term risk assessments methods.

The high costs and ethical concerns associated with large-scale animal research have necessitated the development of reliable, high-throughput *in vitro* screening assays and the use of computational models in toxicology studies [36, 37]. Although various *in vitro* assays have been developed for the toxicity analysis of the ENMs, these methods are not widely employed and may yield results inconsistent with *in vivo* studies [38-40]. This is hardly surprising, as *in vivo* systems are directed through a complex multicellular network that connects the actions of cells, tissues and organs, while these interactions are largely lacking in *in vitro* models [41].

The evaluation of the short- and long-term effects of the ENMs is commonly conducted through cell viability and proliferation assays. The ENM toxicity is mainly quantified by metabolic activity assays (*e.g.* MTT, XTT, Alamar blue, LDH) and direct

cell death assays (calcein AM / ethidium homodimer staining). Cytotoxicity screening of an ENM is often a preliminary step that determines whether the material is suitable for further testing. As such, comparative assays have been developed for this process. One particularly stringent example is provided by Kroll et al., who have developed a matrix-based test system to evaluate the cytotoxic effects of 23 ENMs against a set of sensitive cell lines and suggest that such a system can be used to predict *in vivo* nanostructure behavior, minimizing the number of animals used in toxicity assessments by pre-selecting against cytotoxic ENMs [42]. The matrix-based, high-throughput cytotoxicity screening of ENMs is of great importance for the development standardized cytotoxicity assessments and modelling studies.

#### **1.4 Selected Applications of Engineered Nanomaterials**

The unique properties of the ENMs give novel features such as electrical, catalytic, magnetic, mechanical, thermal or imaging which make the ENMs potential candidates for applications in commercial, environmental, military and medical fields [43]. Due to wide range of applications of the ENMs, only oral drug delivery and synthetic enamel biomineralization application (which are related to chapter 3 and chapter 4) areas will be briefly explained in the following sections.

##### **1.4.1 Oral Drug Delivery**

There are different routes of drug administration to body, and oral administration is the most convenient and cost effective one. However, various factors such as physicochemical properties, desired target site, absorption rate, gastrointestinal digestion and condition of the patient determine the route of drug administration.

Although some drugs (small molecules) are suitable for oral drug delivery, however most of the biomolecules (peptide, protein-based drugs) cannot be delivered orally due to poor stability in the gastrointestinal (GI) tract, low solubility and/or bioavailability and poor drug penetration and absorption in intestine as a result of mucus barrier. Despite these limitations, new formulations [44-46] and devices [47] are being developed that protect fragile biopharmaceuticals from poor stability and improve controllable delivery and absorption rate as a result of advances in nanotechnology and nanoscience (Figure 1.4). The efficacy of new formulations and devices are being tested especially by using *in vivo* models due lack of complexity of gastrointestinal systems in *in vitro* models.

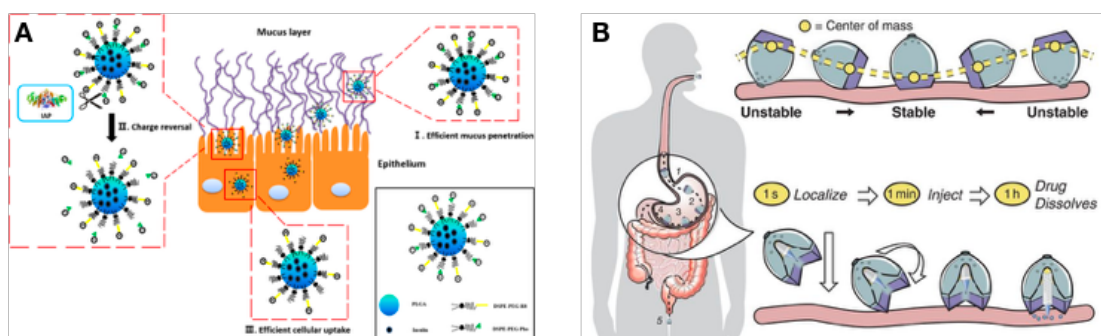


**Figure 1.4 Schematic diagram of oral insulin delivery methods to different site of body.** (A) Poly(lactide-co-glycolide) (PLGA) nanoparticles engineered with cell penetrating peptides to sequentially overcome mucus and epithelial barrier to deliver insulin. Reprinted with permission from [48] Copyright (2018) American Chemical Society. (B) Self-orienting millimeter-scale applicator (SOMA) localizes to the stomach lining, orients its injection mechanism to the tissue wall, and injects a drug payload through the mucosa. Reprinted with permission from [47] Copyright (2019) Science.

In general, rodents are used to understand therapeutic effects or pharmacokinetics of oral delivery of engineered pharmaceuticals. However, the results obtained from *in vivo* studies are discordant in translating to humans [49, 50]. To overcome conflict

between *in vivo* models and human clinical trials, there are some critical points which should be considered during design and synthesis of the ENMs used in pharmaceutical encapsulations. The ENMs used in drug delivery must overcome numerous limitations including endogenous enzymes and acidity in gastric environment and the continuous secretion of protective mucus layer in GI tract. These limitations differ in rodents compared to humans [51]. Rodents and most of animals have less acidic gastric environment compared to humans which affects stability of new formulations. Additionally, frequently used animal models, mice and rats, produce less mucus layers [52]. In addition to these parameters, physiology, anatomy, biochemistry and bacterial colonization should be considered to achieve bench-to bedside transition of the ENMs used in oral delivery [51].

#### **1.4.2 Synthetic Enamel Biomineralization**

Biomineralization is a biochemical process by which organisms form minerals. Biologically controlled mineralization shaped the evolution of living organisms starting last 3500 Myr. While many organisms from different phyla can form high number of minerals [53], hydroxyapatite (HA) in mammals is particularly interesting due to fundamental role in the formation of hard tissues including bone and teeth. The cells in mineralized tissues (e.g. osteocytes in bone, ameloblast in tooth) regulate biomineralization through controlling mineral resorption and deposition. Although both bone and tooth share the same mineral, HA, their mineralization and hierarchical organization are different as a result of presence or absence of regulating cells in mature mineralized tissues. Bones are highly dynamic as result of remodeling, regulation of calcium ion concentration in body and response to applied stress [54]. In

contrast, tooth is highly static after maturation in terms of new mineral formation. Understanding of biomineralization process in mineralized tissue is important for developing advanced materials for their regeneration and repair [55]. Recently, artificial approaches have been developed to repair demineralized enamel to prevent deep lesions and tooth loss. These approaches mostly utilize the ENMs including dendrimer and star polymers [56, 57], microgels [58, 59], peptides [60-62], modified HA powder [63], and apatite nanoparticles [64, 65] to mimic biologically controlled mineralization. Among them most promising ENMs are peptide-based materials due to inspiration or derivation from enamel proteins. Peptide based nanomaterials can provide hybrid organic-inorganic interactions and help to create a hierarchical structure similar to developmental process of enamel as depicted in Figure 1.5.

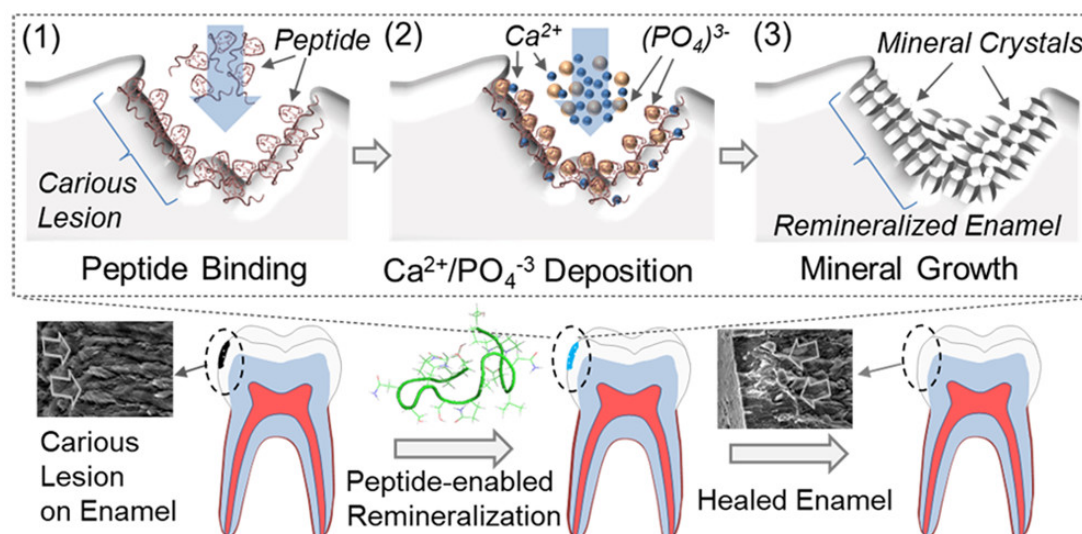


**Figure 1.5 The peptide-guided remineralization in carious enamel lesion.** The amelogenin-derived 15 amino acid long peptide, shADP5, demonstrated newly formed crystalline mineral layer on an artificially created lesion on human enamel in the presence of  $\text{Ca}^{2+}$  and  $\text{PO}_4^{3-}$  ions. Reprinted from permission from American Chemical Society, Copyright © 2018 [61].

## CHAPTER 2

### **2 Intracellular Accumulation of Gold Nanoparticles Leads to Inhibition of Macropinocytosis to Reduce the Endoplasmic Reticulum Stress**

*A partial content of this work was published in the following journal publication [66]. Gunduz, N., Ceylan, H., Guler, M. O., Tekinay, A. B., Intracellular Accumulation of Gold Nanoparticles Leads to Inhibition of Macropinocytosis to Reduce the Endoplasmic Reticulum Stress, Scientific Reports DOI: 10.1038/srep40493, 2017 with permission from Nature Publishing Group.*

#### **2.1 The objective**

Advances in nanotechnology have resulted in the development of a large variety of engineered nanomaterials for numerous applications in chemistry, engineering and biomedical sciences. However, the prospect of ubiquitous use of nanomaterials has also raised concerns regarding the safety of these materials, so the assessment of their potential toxicities has emerged as a major research area. The long-term risk assessment of nanomaterials is typically done using animal models, which assess systemic toxicity and accumulation in organs rather than the behaviors undertaken by individual cells to reduce the local concentration of toxic material. In contrast, cell culture-based toxicity models are generally used for assessment of short-term exposure, while long-term observation is difficult because the high proliferative

capacity of cells imposes constraints on maximum culture time. Thus, there is a detachment between *in vitro* and *in vivo* models of toxicity assessment and a strong need for further research into the cellular processes that are altered during long-term nanoparticle exposure. In this work, I developed a novel nanoparticle accumulation to show the impact of slow, long-run intracellular accumulation of AuNPs on the nanoparticle uptake dynamics and associated intracellular stresses *in vitro*. Continuous exposure to AuNPs nanoparticles in low doses provides a reliable window for dissecting the toxicity stemming from the long-term exposure to nanoparticles, from acute toxicity resulting from high-dose exposure.

## **2.2 Introduction**

Advances in nanotechnology have resulted in the development of a large variety of engineered nanomaterials for numerous applications in chemistry, engineering and biomedical sciences [67-70]. Among them, engineered AuNPs attract special attention because of their rather well-established fabrication methods, low variance in size and shape, convenient means of surface functionalization, high chemical stability, inertness, relative biocompatibility, low acute toxicity and wide-range applications [71]. Although the presence and use of colloidal gold based on ancient times, the most famous example Lycurgus Cup was manufactured in the 5th to 4th century B.C, however they gain more attention after Faraday's investigation on the optical properties of thin films prepared from colloidal gold solutions in 1857. After that, various methods based on chemical (bottom-up) and physical (top-down) principles for the preparation of gold nanoparticles were reported in the 20th century. The well-known and most popular chemical method is developed by Turkevich et al. for

preparation of gold nanoparticles ca. 20 nm, in which boiling chloroauric acid (HAuCl<sub>4</sub>) is reduced with citrate where it acts as both reducing and stabilizing agent [72]. This method is further refined in 1973 by Frens to obtain AuNPs at certain size (between 16 and 147 nm), via changing the gold salt-to-citrate ratio [73]. Alkanethiol-stabilized AuNPs below 5 nm was achieved by Brust and Schiffrin in 1994 by biphasic reduction protocol. Briefly, HAuCl<sub>4</sub> salt is transferred into toluene solution using tetraoctylammonium bromide (TOAB) as the phase-transfer reagent and reduced by NaBH<sub>4</sub> in the presence of dodecanethiol which resulted in low dispersity AuNPs between 1.5 to 5 nm [74]. Further, modification of the size of AuNPs was shown by changing reaction conditions as gold-to-thiol ratio, reduction rate, and reduction temperature [75]. The functionalization of gold nanoparticle surface is generally achieved by ligand exchange reaction which displace the intermediate stabilizers (sodium citrate or tetraoctylammonium bromide) with high affinity disulfide groups in (bio)organic molecules such as antibody, carbohydrates and peptides for biomedical applications [76]. However, this approach of gold nanoparticle functionalization has major drawbacks. For example, nanoparticle aggregation occurs as a result of replacement of highly charged citrate ions with less charged thiols during one-step ligand exchange reaction. In addition, this reaction may not be a complete reaction which reduces ligand density on the surface of nanoparticle and therefore decrease the effectiveness. Moreover, complete elimination of toxic stabilizer after nanoparticle synthesis is difficult, and their timely desorption from the surface of nanoparticles induces cell death [77]. To overcome mentioned drawbacks, robust engineered gold nanoparticle preparation approach is developed with a novel chemical route: one-step synthesis in which biomolecules act as reduction, nucleation and capping agents.



Prominent examples are multidomain peptides for single-step, size-controlled synthesis of biofunctionalized gold nanoparticles [78-80]. Consequently, functionalized AuNPs are now being used with increasing frequency in photothermal therapy [81]; targeted drug [82] and gene delivery [83], magnetic resonance imaging and other biomedical applications, and are also considered therapeutic agents by themselves (e.g. for rheumatoid arthritis) [84] depicted in Figure 2.1.

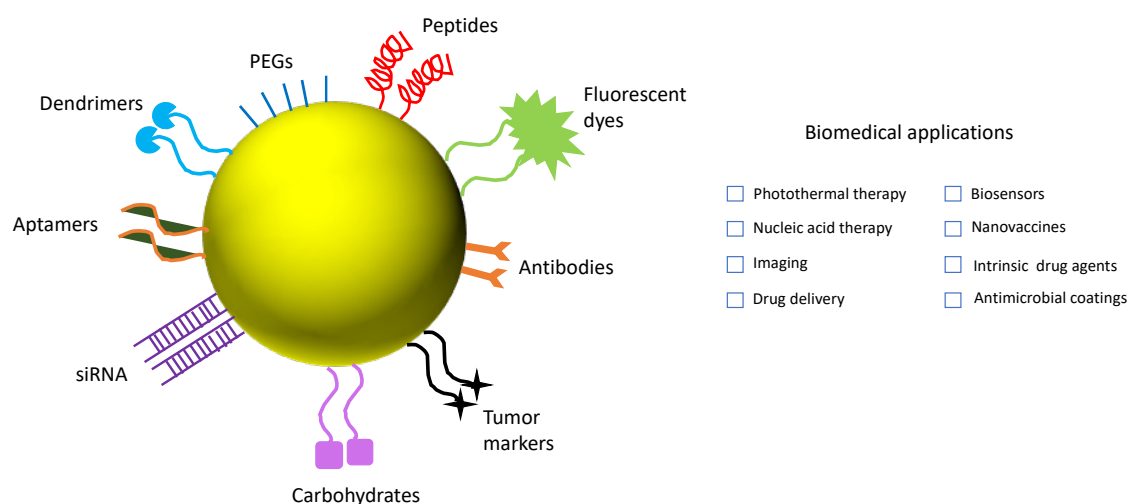


**Figure 2.1 Biomedical application of gold nanoparticles after functionalization.**

Localized surface plasmon resonance (LSPR), easy chemical modification, inertness of gold nanoparticles (e.g. nanospheres, nanorods, nanoshells, nanocages, nanostars) with different variety of biomolecules make them reliable candidates for different biomedical applications.

Immediately following their entry into biological systems, AuNPs interact with various local biomacromolecules to assemble a dynamic protein corona on their surfaces. The formation of this layer has significant effect on the cellular uptake [14, 85, 86], targeting ability [87], accumulation and toxicity of nanoparticles in living systems, and depends strongly on the composition of the environment encountered by the material. In addition, studies that do consider long-term cellular exposure tend to utilize the occupational exposure model [88-92], and more studies are necessary to understand long-term nanoparticle toxicity upon continuous exposure. Recently, chronic and chronic AuNPs exposures at low dose induce gene expression changes in

oxidative stress, cell cycle regulation, inflammation, and unfolded protein response pathways of human dermal fibroblasts (HDFs). Moreover, shape and surface chemistry are key players in driving gene expression changes [93]. Here in this study I developed a novel long-term accumulation model to assess intracellular effect of AuNPs on cellular uptake and stress mechanism such as ER stress which provides very practical and informative for the future studies regarding the accumulation of a wide scope of engineered nanomaterials.

## **2.3 Experimental Section**

### **2.3.1 Chemicals and Reagents**

Gold (III) chloride trihydrate ( $\text{HAuCl}_4 \cdot \text{H}_2\text{O}$ ), 3-(4, 5-dimethylazol-2-yl)-2, 5-diphenyl-tetrazolium bromide (MTT) kit, Nystatin, Amiloride hydrochloride hydrate, Chlorpromazine hydrochloride, Silver Enhancer Kit SE-100, hydrochloric acid fuming 37%, and Nitric acid > 65% were purchased from Sigma-Aldrich Chemical Co. 5 (6)-Carboxy-2', 7'-dichlorofluorescein diacetate (DCF), ethidium homodimer, Calcein Am, Click-iT EdU assay, TRIzol, Alexa Fluor 488 conjugated Cholera toxin subunit B (recombinant), Fluorescein conjugated Dextran (10000 MW) and Alexa Fluor 488 conjugated Transferrin from human serum were purchased from Invitrogen (C34775, D1820, and T13342). All cell culture materials were also purchased from Gibco, Invitrogen. Sodium citrate tribasic were obtained from Codex, Carlo Erba. Amicon® Ultracel centrifugal falcons were purchased from Millipore. Ultrapure water (18.2 MΩ) was obtained from a Sartorius arium® Lab Water System.

### 2.3.2 Synthesis of Gold Nanoparticles

All glassware was carefully cleaned with aqua regia (3:1 mixture of hydrochloric and concentrated nitric acids), and rinsed with distilled water several times before use. AuNPs with 12-nm diameter were synthesized according to the previously published Turkevich protocol [45]. Briefly, 100 mL of  $\text{HAuCl}_4$  (1 mM) in water was boiled under stirring, and 10 mL of sodium citrate trihydrate solution (38.8 mM) was added rapidly to the chloride solution, which resulted in a change in solution color from pale yellow to deep red (depicted in Figure 2.1).

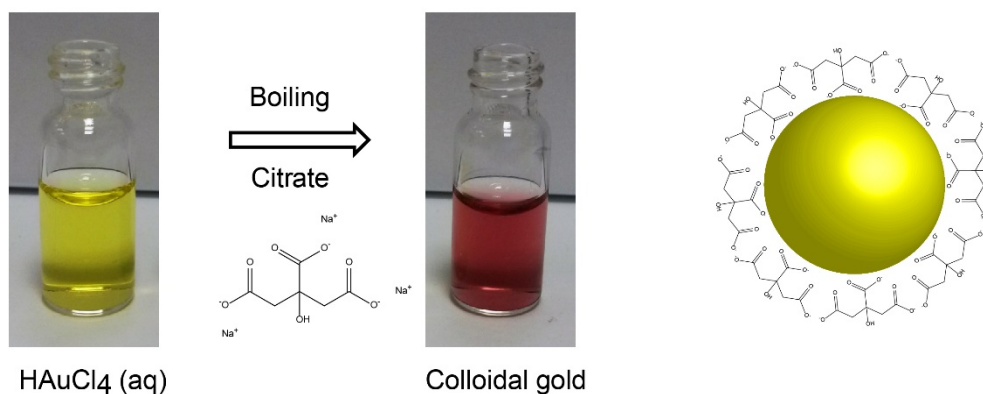


**Figure 2.2 Schematic illustration of citrate-stabilized AuNPs synthesis.** Colloidal gold was prepared with  $\text{HAuCl}_4$  solution under reflux conditions where citrate acts as both the reducing agent and stabilizing ligand.

### 2.3.3 UV-Vis Spectroscopy

UV-Vis spectra of AuNP solutions was measured using a SpectraMax M5 Multi-Mode Microplate Reader. Spectra of freshly prepared AuNPs and water (for baseline subtraction) were collected using quartz cuvettes with 1 cm optical path lengths and in a 250-750 nm range with 2 nm increments.

### **2.3.4 Transmission Electron Microscopy**

Structural characterization of the AuNPs was performed using a FEI Tecnai G2 F30 transmission electron microscope (TEM) at 300 kV. TEM samples were prepared on a fine mesh Cu grid by incubating a drop of AuNP solution for 5 min, washing with a drop of distilled water for 2 min and repeating these steps for two more times prior to drying. Individual particle sizes were measured using ImageJ (NIH) software.

After the characterization of the nanoparticles by TEM and UV-Vis spectroscopy, their initial concentration was calculated by using previously established theoretical calculations [46]. The nanoparticles were then concentrated by using Amicon® Ultracel centrifugal falcons (10 K) at 6000 rpm for 5 min (repeated multiple times for required concentrations).

### **2.3.5 Dynamic Light Scattering (DLS) and Zeta Potential Measurements**

DLS measurements were carried out using a Malvern NanoZS Zetasizer at room temperature. Auto-correction was done as the average of three runs of 10 s each (Malvern Instruments, Southborough, MA, US).

### **2.3.6 Cell Culture and Maintenance**

Immortalized human umbilical cord vein endothelial cells (HUVECs) were donated by Yeditepe University, Istanbul, Turkey (They indicated source of cells as American Type Culture Collection, ATCC, but they could not give an exact catalog number). HUVECs were purified as described and were characterized by staining with CD34, CD31, and CD90 surface markers. These cells were found to be positive for CD31 and

CD34 but negative for CD90. HUVECs were cultured in a humidified, 37 °C, 5% CO<sub>2</sub> incubator using 75 cm<sup>2</sup> polystyrene cell culture tissue flasks containing Low Glucose Dulbecco's modified Eagle's medium (DMEM) supplemented with 5% or 10% heat inactivated fetal bovine serum (FBS, Gibco), 1% penicillin/streptomycin (P/S) and 2 mM L-glutamine. Passaging of cells was performed at cell confluency between 90 to 100% using trypsin/EDTA. Cells were diluted 1:4 for subculturing.

### **2.3.7 Cell Viability and Proliferation**

The toxicity of AuNPs was assessed by a standard colorimetric cellular viability assay, in which 3-(4,5-dimethylazol-2-yl)-2,5-diphenyl-tetrazolium bromide (MTT) dye is converted to insoluble purple formazan crystals and metabolic activity is evaluated through absorbance measurements at 570 nm and a background absorbance of 690 nm using a SpectraMax microplate reader (Molecular Devices, Sunnyvale, CA). HUVECs were seeded at a density of  $7.5 \times 10^3$  cells/well in a 96-well plate. After 4 h of incubation, media were removed and replaced with either 5% FBS or 10% FBS DMEM containing AuNPs at concentrations ranging from 0.5 µg/mL to 64 µg/mL, and cells were incubated for 24 h at 37 °C in a humidified incubator with 5% CO<sub>2</sub>. At the end of the exposure period, AuNPs containing media were removed and washed three times with warm medium to remove AuNPs to prevent their contributions to the result. Then, MTT (reconstituted in phenol-free medium as 5 mg/mL stock concentration) containing phenol and serum free medium was added in an amount of equal to 10% of the culture medium volume. After 4 h incubation period, the resulting formazan crystals were dissolved after adding equal amount of MTT Solubilization Solution to the culture medium volume by gentle pipetting and shaking in a gyratory

shaker. All experiments were performed in quadruplicate and with three independent repeats. For long-term viability assessment via MTT assay, HUVECs from AuNP accumulated and non-accumulated at day 57 were re-seeded at a density of  $7.5 \times 10^3$  cells/glass in a 96-well plate. After 24 h of incubation, same protocol as determined above in detail was followed. Long-term viability assessment of HUVECs was also analyzed by live-dead assay. Briefly, HUVECs from AuNP accumulated and non-accumulated at day 57 were re-seeded at a density of  $5 \times 10^3$  cells/well in a 96-well plate. After 24 h of incubation, plate was centrifuged for 5 min at 2500 rpm to keep dead cells on the surface. Wells were washed with 1x PBS and 2 min centrifugation was done at each step. 2  $\mu$ M calcein AM and 4  $\mu$ M ethidium homodimer reagents were diluted in PBS respectively. After 30 min incubation, cells were observed under a fluorescent microscope.

Proliferative cells were determined using Click-iT EdU assay (Molecular Probes). HUVECs were incubated with a nucleoside analogue of thymine, EdU (5-ethynyl-20-deoxyuridine), in the culture medium. EdU is incorporated into DNA during the synthesis phase (S phase) of the cell cycle, and hence enables direct quantification of proliferation. HUVECs from AuNP accumulated and non-accumulated cultures at day 49 were reseeded on 15 mm cover glasses at a density of  $2.5 \times 10^4$  cells/glass. After 8 h of incubation, one half of the medium was replaced with 20  $\mu$ M EdU-containing fresh media supplemented with 5% FBS. Cells were then post-incubated for 48 h for the incorporation of the thymine analogue to DNA. Following post-incubation, cells were fixed with 4% paraformaldehyde, permeabilized with 0.5% Triton-X, and treated with Alexaflour-488 conjugated azide as recommended by the supplier. Proliferative cells were imaged by fluorescent microscopy. Stained cell nuclei were counted with

ImageJ (NIH) software. The average counts of stained cell nuclei were used to evaluate the relative proliferative cell numbers. Both viability and proliferation results were normalized to non-treated control group.

### **2.3.8 Imaging of AuNPs within Cells by Silver Staining**

HUVECs were seeded on 13 mm cover glasses at a density of  $2.5 \times 10^4$  cells/glass. After 4 h of incubation, media were removed and replaced with media containing AuNPs at concentrations ranging from 0.5  $\mu\text{g/mL}$  to 64  $\mu\text{g/mL}$ , and the cells were incubated for 24 h. Cells were then washed three times with 1x PBS to remove excess AuNPs. After washing, cells were fixed with 4% paraformaldehyde for 15 min, and silver staining was performed using Sigma Silver Enhancer Kit according to the manufacturer's instructions. Briefly, silver enhancement solution was prepared by mixing equal volumes of Silver Enhancement Stain A and Silver Enhancement Stain B (Sigma Aldrich) freshly. After mixing two solutions, 300  $\mu\text{L}$  volume was added to each well to allow reaction of solution with AuNPs inside the cells. The staining was monitored under a light microscope and stopped before seeing background staining (~up to 10 minutes). After incubation, wells were washed with deionized water at least three times and cover glasses were mounted with water based mounting media. Bright field images were taken after staining to visualize the AuNP presence within cells. Silver staining was also performed at different long-term accumulation time points with the identical protocol explained above.

### **2.3.9 Determination of Cellular Internalization Pathway of AuNPs**

Endocytosis inhibitors are often used to determine which endocytosis pathway plays a central role for the cellular uptake of the NPs [4]. The concentrations and treatment times of small molecule chemical inhibitors were optimized in a preliminary experiment to select the maximum non-toxic doses and treatment times. HUVECs were seeded at  $2.5 \times 10^4$  cells/well density in 24 well plates. After 4 h of incubation, cells were treated with chemical inhibitors at final concentrations of 2.5 mM amiloride (inhibits micropinocytosis), 100  $\mu\text{g/mL}$  nystatin (inhibits caveolin-dependent pathway) and 2.5  $\mu\text{g/mL}$  chlorpromazine (inhibits clathrin-dependent pathway) to inhibit specific pathways and to understand the internalization mechanism of the AuNPs (Table 2.1). After 1 h incubation, the inhibitors were removed, and the cells were exposed to 8  $\mu\text{g/mL}$  of AuNPs in 5% FBS DMEM. After 4 h incubation with AuNPs, cells washed three times with 1x PBS to remove excess AuNPs. After washing, cells were detached from the surfaces with trypsinization and collected with centrifugation at 2500 rpm for 5 min. The protein isolation was performed according to instructions of the M-PER® Mammalian Protein Extraction Kit (Thermo Scientific). After that, protein concentrations of samples were determined with Pierce™ BCA Protein Assay (Thermo Scientific). ICP-MS measurement was performed same as mentioned above.



**Table 2. 1 Chemical inhibitors used for the inhibition of the endocytosis pathway of cells**

<b>Inhibitor</b>	<b>Amiloride</b>	<b>Nystatin</b>	<b>Chlorpromazine</b>
<b>Clathrin</b>	No	No	Yes
<b>Caveolin</b>	No	Yes	No
<b>Micropinocytosis</b>	Yes	No	No

### **2.3.10 In Vitro Long-term Accumulation Model**

Following assessment of the cell viability, a non-toxic dose of 8  $\mu\text{g}/\text{mL}$  was chosen for long-term accumulation experiments. HUVECs were seeded in 6 well plates at a density of  $1 \times 10^5$  cells/well, and exposed to AuNPs after their attachment to well surfaces ( $\sim 4$  h). HUVECs were later subcultured after reaching *ca.* 90% confluency and re-seeded again at  $1 \times 10^5$  cells/well density to 6-well plates for further incubation. This process was repeated in three-day intervals, as represented in Figure 2.3. In each passage, the remaining cell pellets were used for RNA isolation, protein isolation, viability and proliferation analyses, silver staining, and ICP-MS measurements. For ICP-MS measurements, cells were counted at least three times with trypan blue to determine the remaining cell amounts for normalization.

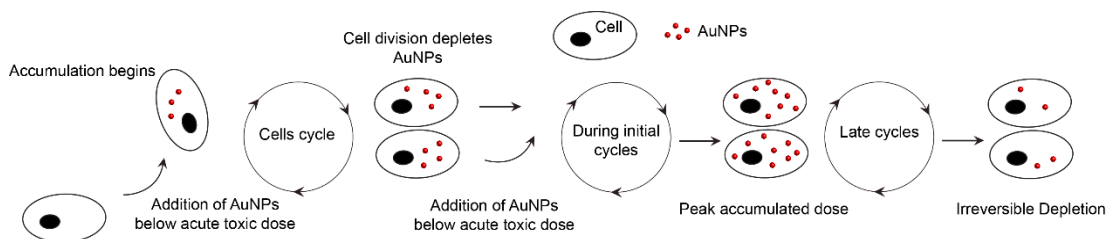


**Figure 2.3 Schematic illustration of the long-term AuNP accumulation model.**

Endothelial cells (HUVECs) are cultivated under standard growth conditions in tissue culture plates. Additionally, their culture media were supplemented with AuNPs at a constant dose of 8  $\mu\text{g}/\text{mL}$ , which is just below the acute lethal level. Based on this model, cells are expected to uptake AuNPs during the growth phase of the cell cycle, and then, typically, undergo mitosis and presumably halve their nanoparticle content into each of the offspring. Nevertheless, the continuous exposure to the nanoparticles in the medium leads to steady intracellular accumulation over time. In the early term, i.e., approximately the first two weeks, cells were observed to steadily accumulate AuNPs until a maximum peak level followed by a steady decrease for the next following weeks approaching to the ground zero level.

### 2.3.11 Quantification of AuNPs within Cells by ICP-MS for Accumulation

#### Analysis

To investigate the protein corona effects on the internalization of the AuNPs, short-term uptake of AuNPs in 5% FBS DMEM and 10% FBS DMEM was performed in HUVECs. The cells were seeded in 6 well plates at a density of  $1 \times 10^5$  cells/well, and exposed to 8  $\mu\text{g}/\text{mL}$  of AuNPs in 5% FBS DMEM and 10% FBS DMEM after their attachment to well surfaces ( $\sim 4$  h). After 4 h incubation with AuNPs, cells were washed three times with 1x PBS to remove excess the AuNPs. After washing, cells were detached from the surfaces with trypsinization and collected with centrifugation at 2500 rpm for 5 min. The protein isolation was performed according to the instructions of M-PER® Mammalian Protein Extraction Kit (Thermo Scientific). After

that protein concentrations of samples were determined with Pierce™ BCA Protein Assay (Thermo Scientific). Then, samples were digested by aqua regia, and diluted in 2% nitric acid immediately prior to measurement. A five-point calibration curve was prepared in a gold concentration range of 1.25-20 ng/mL, and the quantification was performed through linear regression of the measured intensity of the analyte and internal standard (Bi) versus the concentration of calibration standards. All results were reported in ppb or ppm of gold per sample. Gold measurements were performed using a Thermo Scientific X Series 2 ICP-MS.

To investigate the long-term accumulation of AuNPs in HUVECs over time, cells were counted at least three times with trypan blue after each passage to determine the remaining cell amounts for normalization. After that, all cell pellets were kept frozen until analysis, and before analysis they were thawed. The following procedure for ICP-MS measurement was performed same as mentioned above. The number of AuNPs per cell was calculated as:

$$m = \rho \frac{4}{3} \pi r^3 \quad m = \text{mass of one AuNP} \quad \rho = \text{density of gold} \quad r = \text{radius of one AuNP}$$

To obtain number of AuNP in each sample, total ppb determined by ICP-MS was divided to the mass of one AuNP. Total AuNP number was divided to cell number.

### **2.3.12 Quantification of AuNPs in Medium by ICP-MS for Exocytosis Analysis**

During long-term accumulation experiment, all media were collected for exocytosis analysis before AuNPs exposure to the cells. Briefly, HUVECs were seeded in 6 well plates at a density of  $1 \times 10^5$  cells/well, and medium was collected for ICP-MS measurements and replaced with AuNP containing medium after their attachment to

well surfaces (~4 h). All collected medium samples were kept frozen until analysis, and the ICP-MS measurements were performed with the same procedure as mentioned above.

### **2.3.13 Imaging of HUVECs with Fluorescent Molecules for Endocytosis Analysis**

At day 23 of long-term accumulation, HUVECs were seeded on 13 mm cover glasses at a density of  $2.5 \times 10^4$  cells/glass. After 4 h of incubation, media were removed and replaced with media containing 5  $\mu\text{g}/\text{mL}$  Alexa Fluor 488 conjugated Cholera toxin subunit B (recombinant), 100  $\mu\text{g}/\text{mL}$  fluorescein conjugated dextran (10000 MW) and 25  $\mu\text{g}/\text{mL}$  Alexa Fluor 488 conjugated transferrin from human serum and the cells were incubated additional 4 h. Cells were then washed three times with 1x PBS to remove excess molecules. After washing, coverslips were closed on glass slides and immediately imaged with Zeiss LSM 510 Meta before cell death.

### **2.3.14 Determination of Cellular Stress Levels by qRT-PCR and Dichlorofluorescein Assay**

RT-PCR and qRT-PCR were used to quantify the XBP1 and sXBP1 amounts. Total RNA was isolated from remaining cell pellets using TRIzol (Invitrogen) according to the manufacturer's instructions. Briefly, Nanodrop 2000 (Thermo Scientific) was used to assess the yield and purity of the extracted RNA. Primer sequences are listed in Table 2.2. Reaction efficiencies for each primer set were evaluated with standard curves using 2-fold serial dilutions of total RNA. cDNA synthesis from RNA and RT-PCR were performed using SuperScript III One-Step RT-PCR Kit (Invitrogen) according to the manufacturer's instructions. PCR products of XBP1 were

electrophoresed on 10% PAGE at 80 V for 5 h. The size difference between spliced and unspliced XBP1 is 26 nucleotides. sXBP1 gene expression profiles were analyzed at each time point of accumulation. Reaction conditions were briefly as follows: 55 °C for 5 min, 95 °C for 5 min, 40 cycles of 95 °C for 15 s, 60 °C for 30 s, and 40 °C for 1 min, followed by a melting curve to confirm product specificity. For gene expression analysis a comparative Ct method was used with the formula of (primer efficiency)<sup>ΔΔCt</sup> where ΔΔCt and ΔCt were explained as:

$$\begin{aligned}\Delta\Delta Ct &= \Delta Ct(AuNP (Acc)) - \Delta Ct(AuNP (Non acc)) \text{ and } \Delta Ct \\ &= Ct(sXBP1) - Ct(GAPDH)\end{aligned}$$

Reactive oxygen species (ROS) formation was analyzed with dichlorofluorescein (DCF) assay after 57 days of accumulation. First 5-(6)-Carboxy-2', 7'-dichlorofluorescein diacetate (DCF) was dissolved in DMSO as 10 mM concentration. Briefly, HUVECs from AuNP accumulated and non-accumulated groups at day 57 were passaged and re-seeded at a density of 5 x 10<sup>3</sup> cells/well in a 96-well plate. After 4 h attachment, 10 μM DCF dye (The optimal working concentration of DCF dye should be determined separately for HUVEC cells and AuNP treated and/or accumulated cells) in prewarmed phenol-free DMEM was laid on cells and incubated for 1 h. After incubation, excess amount of DCF was washed three times with phenol-free DMEM. The cells were recovered in optimal temperature and fluorescent intensity was measured with a microplate reader at Ex/Em ~492-495/517-527 nm wavelengths. 100 μM hydrogen peroxide (H<sub>2</sub>O<sub>2</sub>) was used as positive control and unstained cells were chosen as negative control. Concentration of H<sub>2</sub>O<sub>2</sub> as positive control and recovery time after incubation with DCF were optimized for HUVECs prior to the main experiment.

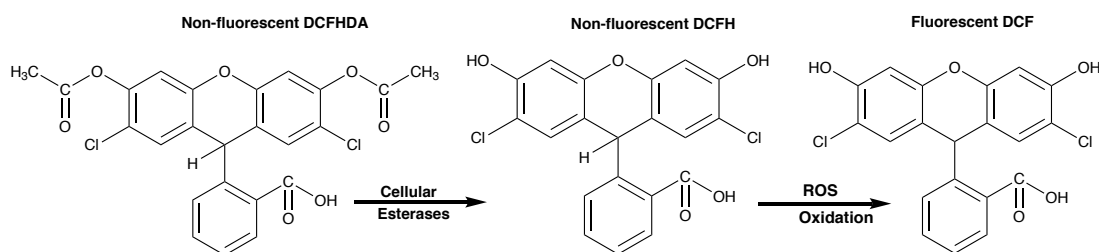


**Figure 2.4 Chemical structure and working principle of DCF assay.** DCFHDA dye is taken by cells and non-specific cellular esterases cleave off the lipophilic groups (acetyl groups), after which the resulting charged compound is trapped inside the cells. Oxidation of DCFH by ROS converts the molecule to DCF, which is highly fluorescent.

Basic working principle of DCF dyes is depicted in Figure 2.4. Reduced and acetylated DCF dyes are non-fluorescent until the acetate groups are cleaved by intracellular esterases and oxidation by reactive oxygen groups inside the cells. Oxidation of this probe can be detected by flow cytometer, microplate reader, a fluorescence microscope at Ex/Em ~492-495/ 517-527 nm wavelengths.

**Table 2. 2 Primers used in RT-PCR and qRT-PCR.**

Gene	Primer Sequence (Forward/Reverse)	Product size (bp)
<b>ER-stress Markers</b>		
<b>XBP1 [94]</b>	TTACGAGAGAAAACATGGCC GGGTCCAAGTTGTCCAGAATGC	289 for unspliced 263 for spliced
<b>sXBP1 [95]</b>	TGCTGAGTCCGCAGCAGGTG GCTGGCAGGCTCTGGGGAAG	263
<b>Reference Gene</b>		
<b>GAPDH</b>	GTGCCAGCCTCGTCTCATA AACTTGCCGTGGGTAGAGTC	186

### 2.3.15 Statistical Analysis

All experiments were independently repeated at least twice, with at least four replicas for each experimental and control group in each independent assay. All quantitative results were expressed as means  $\pm$  s.e.m. Statistical analyses were carried out by one-way analysis of variance (ANOVA) or Student's t test, whichever applicable. Degrees of significance are indicated in graphs when necessary (\*  $p < 0.05$ ; \*\*  $p < 0.01$ ; \*\*\*  $p < 0.001$ ).

## 2.4 Results and Discussion

### 2.4.1 Characterization of AuNPs

Morphology, size and size distribution of citrate-capped AuNPs were confirmed with TEM which showed spherical nanoparticles that are around *ca.* 12 nm in diameter ( $12.2 \pm 1.0$  nm by TEM, Figure 2.5A and B). The hydrodynamic size of citrate-capped AuNPs was found to be  $11.8 \pm 2.3$  nm via DLS measurement in water. This result further confirmed that there was no aggregation in the solution (Figure 2.5C). Moreover, similarities in size and size distribution histograms between TEM and DLS further confirmed the monodisperse synthesis of AuNPs via Turkevich method.

The UV-Vis spectrum of citrate-capped AuNPs displayed a distinct surface plasmon resonance peak (SPR) at 518 nm (in ultrapure water). The location of the SPR signal is informative about the electronic properties of the surrounding medium and the state of nanoparticle aggregations that may potentially result from the formation of surface corona from macromolecular species. A slight red shift in the absorption spectrum of

the AuNPs when placed in fetal bovine serum suggested the formation of a corona on the nanoparticle surface that is caused by the displacement of weakly-bound citrate ions with multivalent macromolecules present in the serum (Figure 2.6A, B, and C). A concomitant increase in zeta potential (from -30 mV to -10 mV) was also observed, further suggesting the alteration in the surface chemistry of the nanoparticles following introduction into the biological environment.

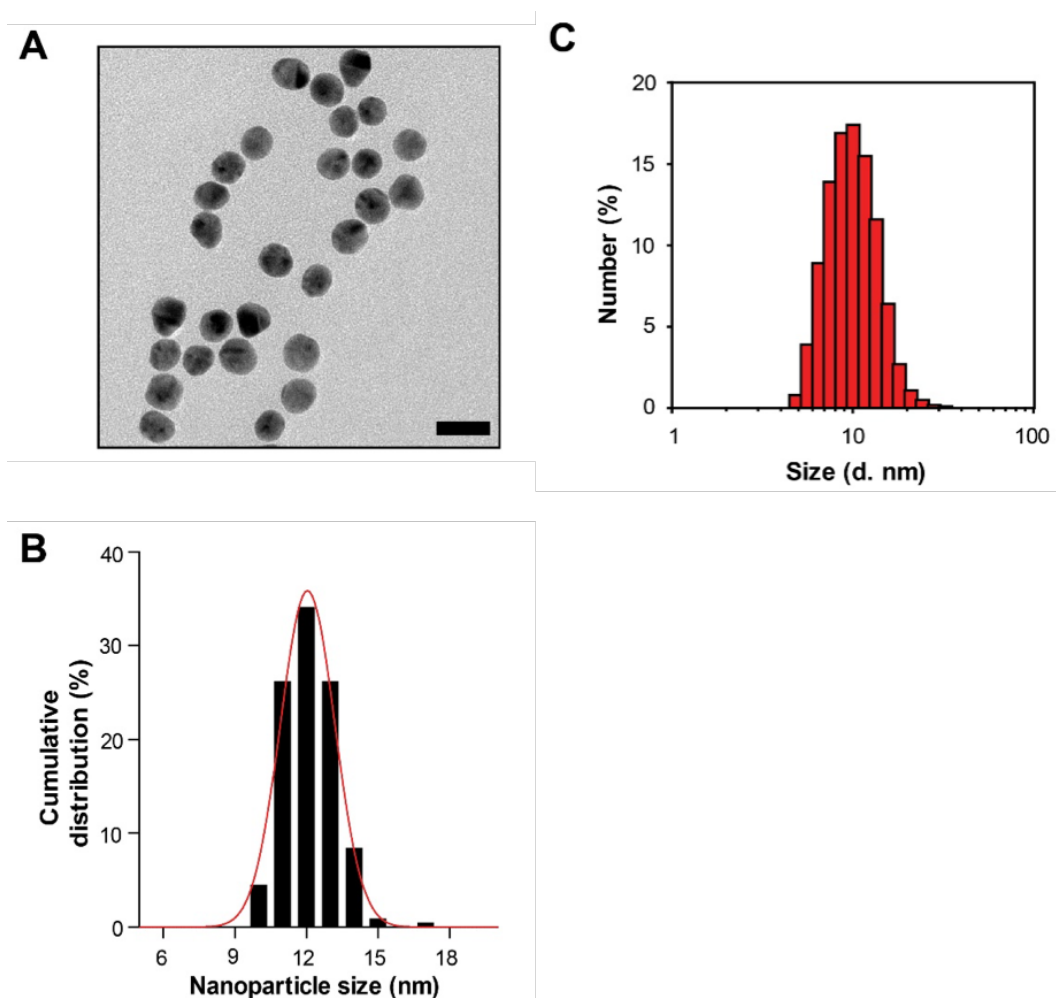


**Figure 2.5 Size and distribution characterizations of AuNPs by TEM and DLS.** TEM image (A), particle size distribution histogram of AuNPs in TEM (B) and DLS (C). Scale bar is 20 nm.



A fluctuation in zeta potential was also observed in time-dependent measurements, which was attributable to the mobile elements of the dynamic corona (Figure 2.6D). Such alterations on the surface chemistry of the AuNPs suggest a new biological identity (in addition to its chemical identity determined by its size and surface characteristics) that could influence its interactions with the cells. The significance of this biological identity was further observed in the viability experiments in order to determine the exposure dose of AuNPs for accumulation studies.

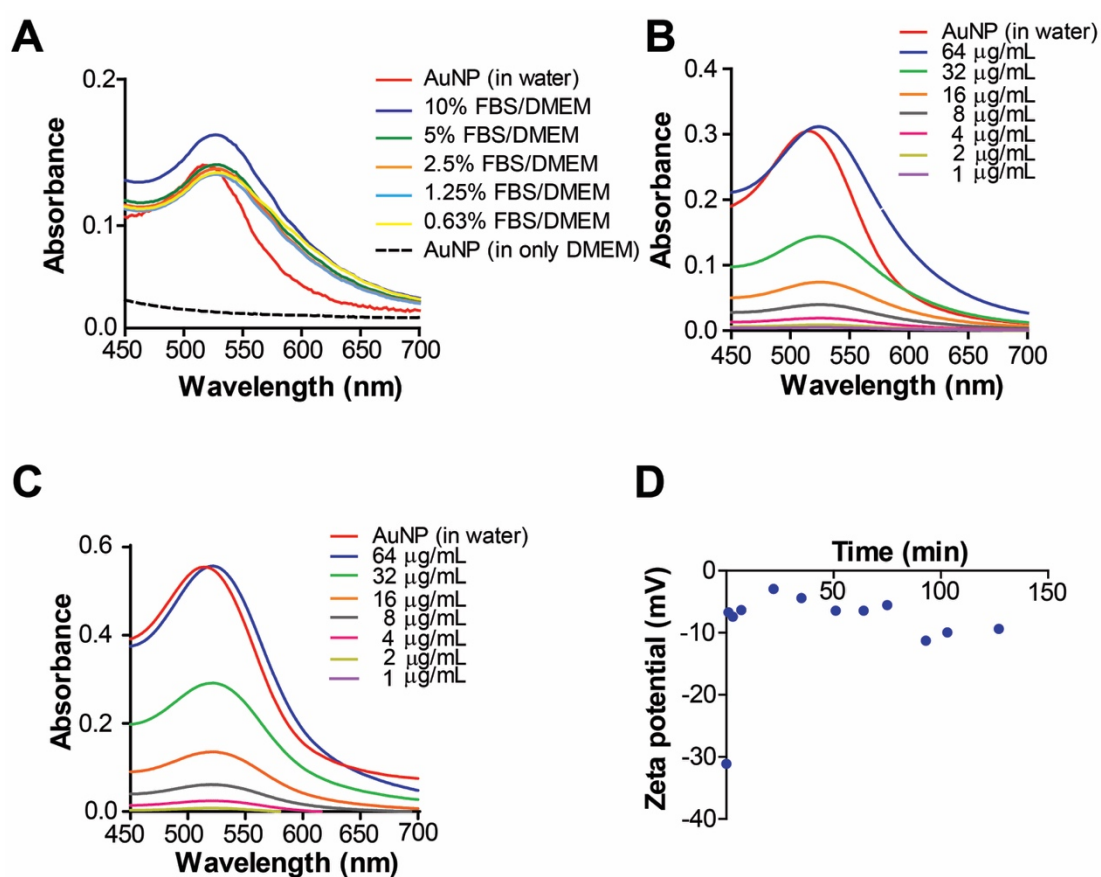


**Figure 2.6 Colloidal stability and protein corona analysis via UV-vis and zeta-potential.** Colloidal stability of the AuNPs in media containing different amounts of FBS (A), UV-vis spectra of the AuNPs in a concentration range of 1-64 µg/mL in 10% FBS containing media (B), UV-vis spectra of the AuNPs in a concentration range of 1-64 µg/mL in 5% FBS containing media (C), and zeta potential of AuNPs in 5% FBS containing media (D).

#### 2.4.2 Cytotoxicity and internalization of AuNPs

Human umbilical vein endothelial cells (HUVECs) were cultured in serially-diluted concentrations of nanoparticles in 5% or 10% serum-containing media. In 5% serum containing medium, AuNPs at 8  $\mu\text{g}/\text{mL}$  and below concentrations were found to have no detrimental effect on the cell viability after 24 h (Figure 2.7B). Higher concentrations, however, resulted in significant decrease in the cell viability because of increased nanoparticle uptake (Figure 2.7B). In 10% serum containing medium, cell viability was *ca.* 80% at 64  $\mu\text{g}/\text{mL}$  administered dose of AuNPs, whereas it was found to be *ca.* 40% in 5% serum containing medium (Figure 2.7A and B). Interestingly, the acute lethality of AuNPs was found to be highly dependent on the concentrations of the biomacromolecules present in the medium, especially at elevated AuNP concentrations.

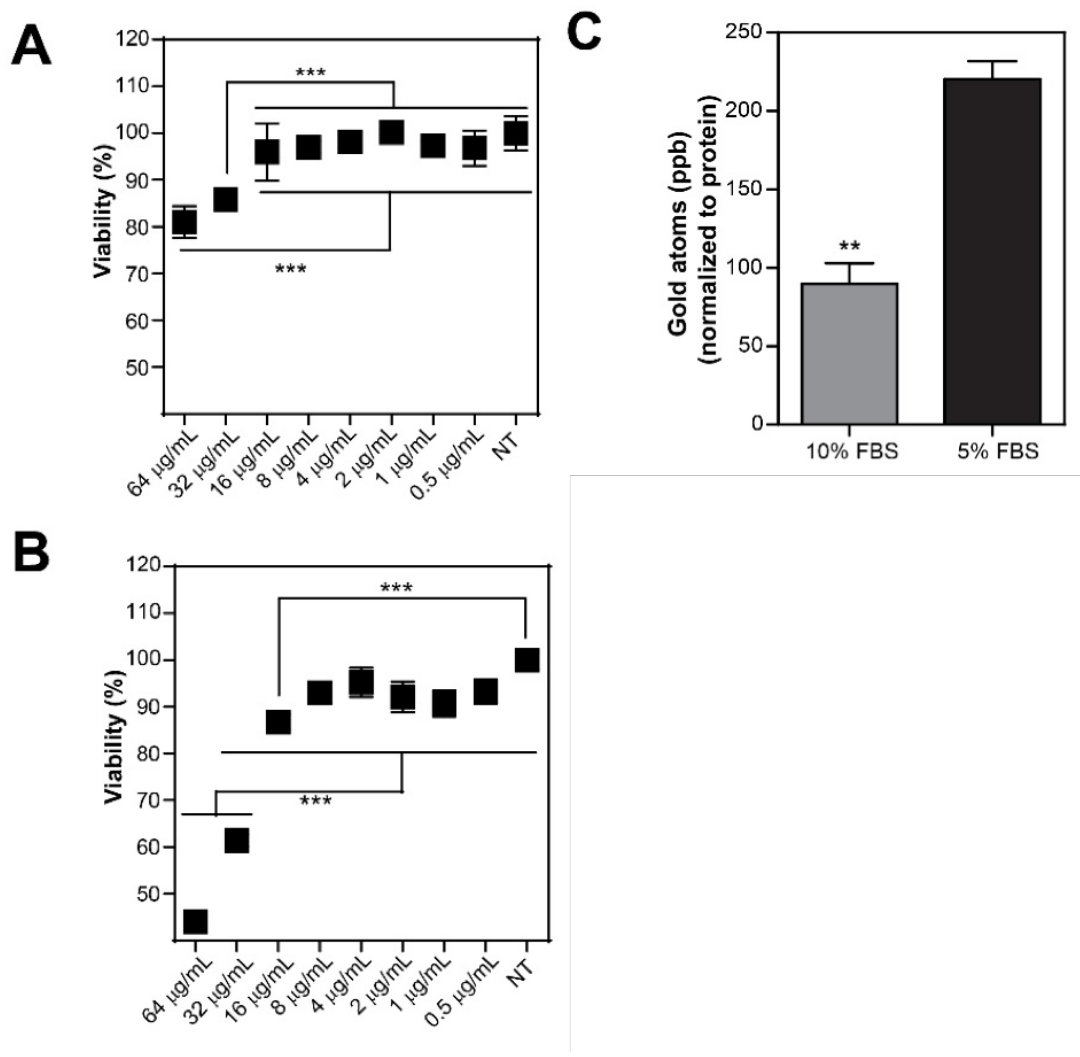


**Figure 2.7 Cytotoxicity and protein corona effects analyses.** Dose-dependent cytotoxicity in HUVECs after 24 h of AuNPs exposure in 10% FBS DMEM (A) and 5% FBS DMEM (B) (Error bars show s.e.m., two independent experiments were repeated with n=4 in 10% FBS DMEM cytotoxicity and n=8 in 5% FBS DMEM cytotoxicity experiments. One-way ANOVA with Tukey’s Multiple Comparison Test was used to show statistical significance at \*\*\* p < 0.001 and \*\* p < 0.01.). Relative uptake of 8 µg/mL AuNPs exposed in 10% FBS DMEM and 5% FBS DMEM in HUVECs after 4 h of incubation (C) (Error bars show s.e.m, two independent experiments were repeated with n=3 in each experiment. Student’s t-test was used to show statistical significance at \*\*p < 0.01.)

The serum and concentration dependent uptake of the AuNPs in HUVECs were also visualized with silver staining. 5% serum containing medium showed higher staining when compared to 10% FBS group (Figure 2.7 and Figure 2.8). Therefore, interactions at the cell-nanoparticle interface appear to be strongly influenced by the altered biological identity of the AuNPs. It is well-known that the high surface energy of AuNPs allow unfolding of coronal proteins, which exposes previously unavailable domains to the biological environment [4]. The cellular uptake of nanoparticles, a very initial step towards the cytotoxic response, may then change considerably depending upon the biological environment and on the concentration of the biomacromolecular components in which the nanoparticles are presented [5]. Indeed, the number of nanoparticles taken up by cells is considerably higher when cells were exposed to the nanoparticles in 5% serum, which is in parallel with the higher cell death caused by AuNPs in 5% serum (Figure 2.7C). Consequently, the altered uptake and viability are likely to be caused by the altered characteristics of the protein corona, which is tremendously influenced by the concentration of the macromolecular species inside serum even though, both mediums are the same.

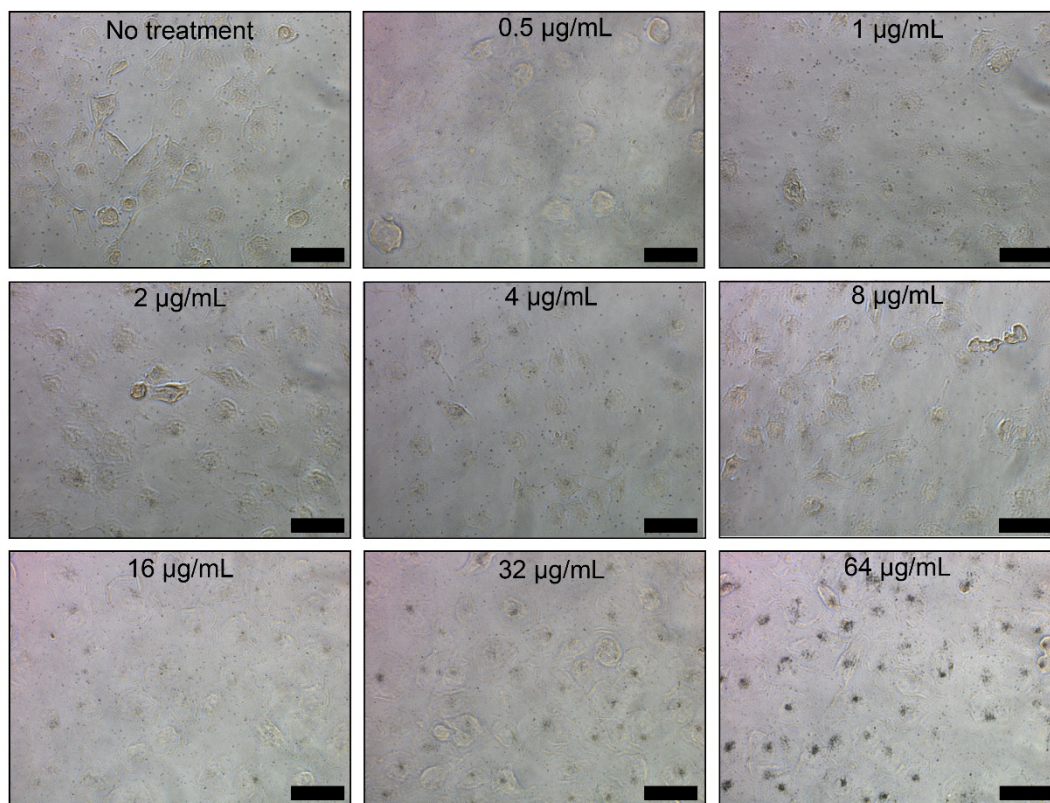


**Figure 2.8 Silver enhancement staining of the AuNPs in HUVECs cultured with 10% FBS DMEM.** After 24 h of incubation of the cells with increasing concentrations of AuNPs in 10% FBS DMEM, silver enhancement staining was performed and bright-field images were taken. Scale bars are 50  $\mu\text{m}$ .

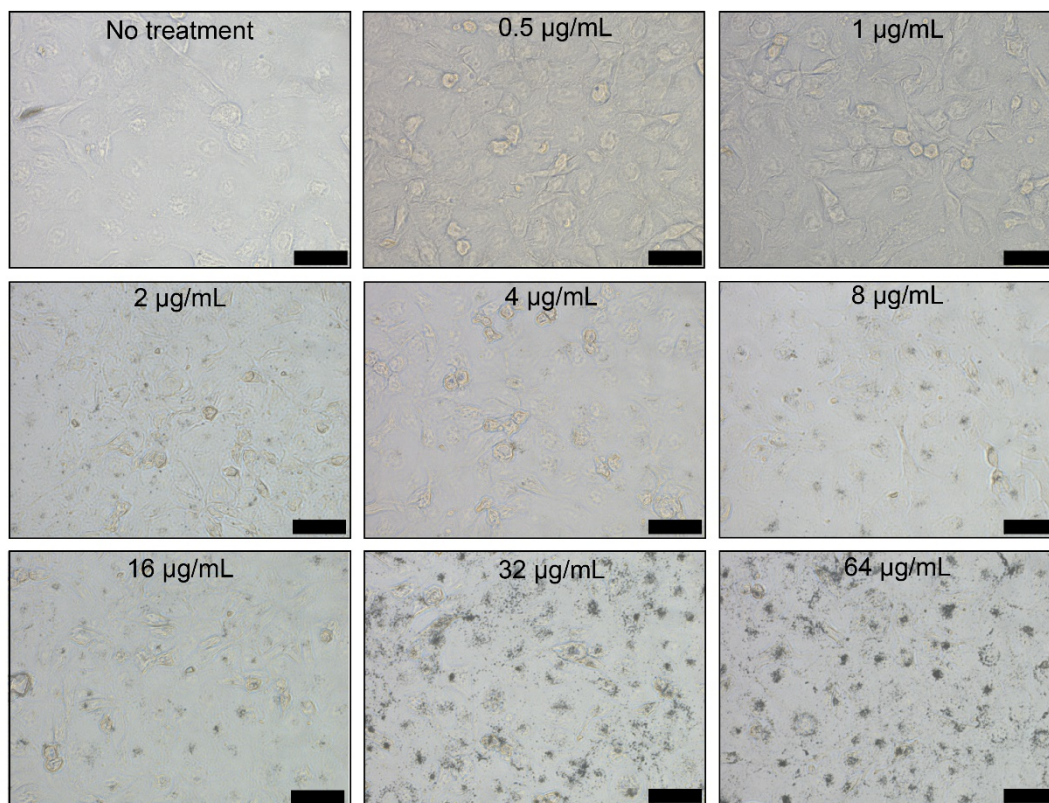


**Figure 2.9 Silver enhancement staining of the AuNPs in HUVECs cultured with 5% FBS DMEM.** After 24 h of incubation of the cells with increasing concentrations of AuNPs in 5% FBS DMEM, silver enhancement staining was performed and bright-field images were taken. Scale bars are 50  $\mu\text{m}$ .

### 2.4.3 *In vitro* long-term accumulation of AuNPs

In the next step, the intracellular accumulation pattern of AuNPs in cultured HUVECs was investigated. Due to the elevated uptake of the AuNPs, from here on, the rest of the accumulation studies were carried out in 5% serum containing medium. HUVECs were seeded and exposed to 8  $\mu\text{g/mL}$  AuNPs; after reaching ca. 90% confluency, they were subcultured and re-seeded again. This process was repeated over time to obtain the long-term accumulation model (see Figure 2.3 and Experimental section). In order to dissect the impact of the long-term nanoparticle accumulation from the acute toxic effects, the AuNPs were introduced to cells below the acute lethal dose, which was

determined as 8  $\mu\text{g/mL}$  from the viability assay (Figure 2.7B and C, Figure 2.8). During the first two weeks, the AuNPs rapidly accumulated inside HUVECs (Figure 2.10A). Intracellular accumulation was further evidenced by silver staining, which enables visualization of the AuNPs under light microscope. Independent repeats of this experiment showed that this initial accumulation period could extend until 20 days, with the same pattern in each repeat. Nonetheless, no further accumulation was observed after this period. Strikingly, the peak accumulation was followed by a steady decline in the amount of intracellular AuNPs (Figure 2.10B). Furthermore, repeatable fluctuations were observed in the intracellular AuNP amount even though the overall trend was down, during the decline period (Figure 2.10A). There are two possible explanations for the decline in the intracellular AuNP accumulation: a) the uptake of new AuNPs was inhibited by inhibiting the endocytosis process, or b) AuNPs inside the cells were actively transported from the cells to the outside environment. There are few reports on the exocytosis of surface-functionalized AuNPs [96-98] despite the fact that the inhibition of the uptake process has not been previously reported.

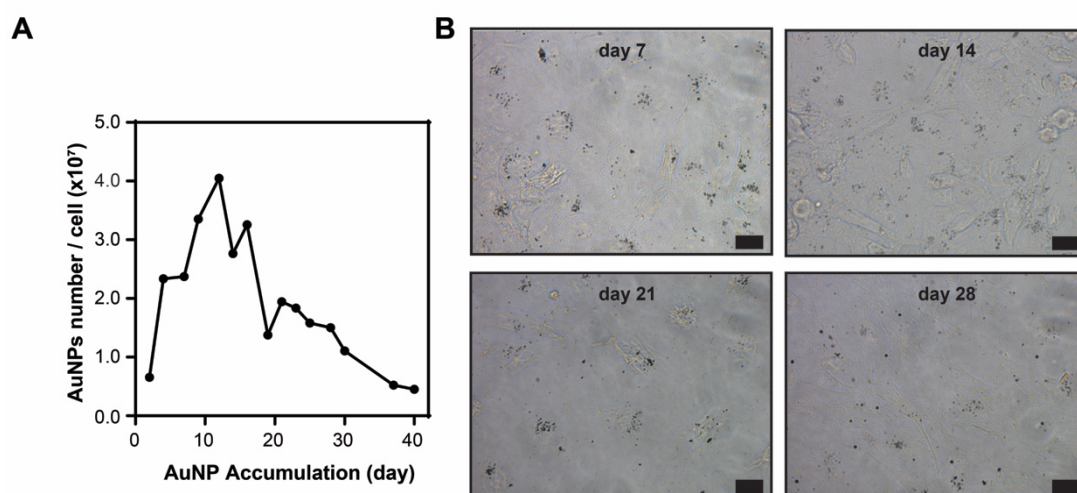


**Figure 2.10 In vitro long-term accumulation of AuNPs in HUVECs.** The amount of the internalized AuNPs in HUVECs quantified from the data measured by ICP-MS

at each passage and its normalization to cell number. The number of AuNPs is expressed as AuNPs per cell (A). Silver staining of the cells at different accumulation time points (day 7, 14, 21, and 28) (B). Scale bars are 20  $\mu\text{m}$ .

#### **2.4.4 Endocytosis and exocytosis behavior of AuNP accumulated cells**

To understand the endocytosis and exocytosis behavior, first, the AuNP uptake mechanism in HUVECs was investigated. Although the uptake mechanisms of bare and surface-functionalized AuNPs in a variety of sizes and shapes have been characterized in the literature, their internalization is difficult to generalize and may depend on processes such as micropinocytosis [78], phagocytosis [99, 100], receptor mediated endocytosis [101] (clathrin- or caveolae-mediated endocytosis) and transcytosis [102]. Therefore, three of these major pathways (micropinocytosis, caveolae-mediated endocytosis, and clathrin-mediated endocytosis) were blocked by inhibitor treatment to observe whether the AuNP uptake depended on any of these mechanisms (Table 2.1). The uptake of the AuNPs was observed to greatly (*ca.* 30 %) diminish following the inhibition of micropinocytosis while this decrease was not as pronounced after inhibition of the caveolae- or clathrin-mediated endocytosis (Figure 2.8). This result suggests that the AuNPs were predominantly entering into HUVECs via micropinocytosis. Gulsuner et al, showed that MDP-AuNPs which contains RGD sequence as targeting moiety enters into breast cancer cells via both clathrin-mediated endocytosis and micropinocytosis pathways [78]. The cells might use non-specific entry routes for endocytosis of non-functionalized AuNPs. Therefore, lack of targeting moiety might activate the micropinocytosis pathway for nanoparticle endocytosis.



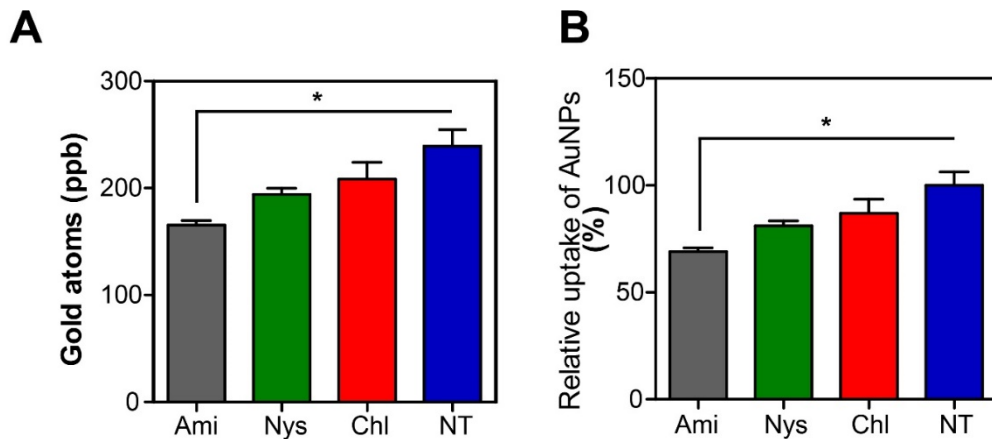


**Figure 2.11 Cellular uptake of AuNPs.** ICP-MS analysis of HUVECs treated with chemical inhibitors of endocytosis and incubated with 8  $\mu\text{g/mL}$  of AuNPs. After 4 h of incubation, total gold atoms (A) and relative uptake (B) in HUVECs were calculated by normalization to protein amounts and untreated (NT) group. (Error bars show s.e.m, two independent experiments were repeated with  $n=3$  in each experiment. One-way ANOVA with Tukey's Multiple Comparison Test was used to show the statistical significance at  $*p < 0.05$ .) (Amiloride blocks micropinocytosis; chlorpromazine prevents the formation of clathrin pits and nystatin disrupts caveolae function).

In order to understand if any of these major routes of uptake is impaired during the accumulation process, the endocytosis competency of cells on day 23, one of the early days of the decline in the intracellular AuNP amount (Figure 2.10A) was analyzed. For this purpose, cells were incubated with fluorophore-conjugated molecules that enter cells through specific endocytosis pathways and then checked if these molecules are inside the cells. Among these molecules, cholera toxin enters cells through caveola-mediated endocytosis, transferrin enters via clathrin-mediated endocytosis, and dextran enters via micropinocytosis. While cholera toxin and transferrin entries were observed in both Accumulated and Non-accumulated groups, dextran entry was observed only in the Non-accumulated group, indicating that micropinocytosis, the

main route of AuNP uptake, ceased altogether (Figure 2.12). Nevertheless, the complete inhibition of macropinocytosis is far from explaining the drastic decrease in the intracellular AuNP.

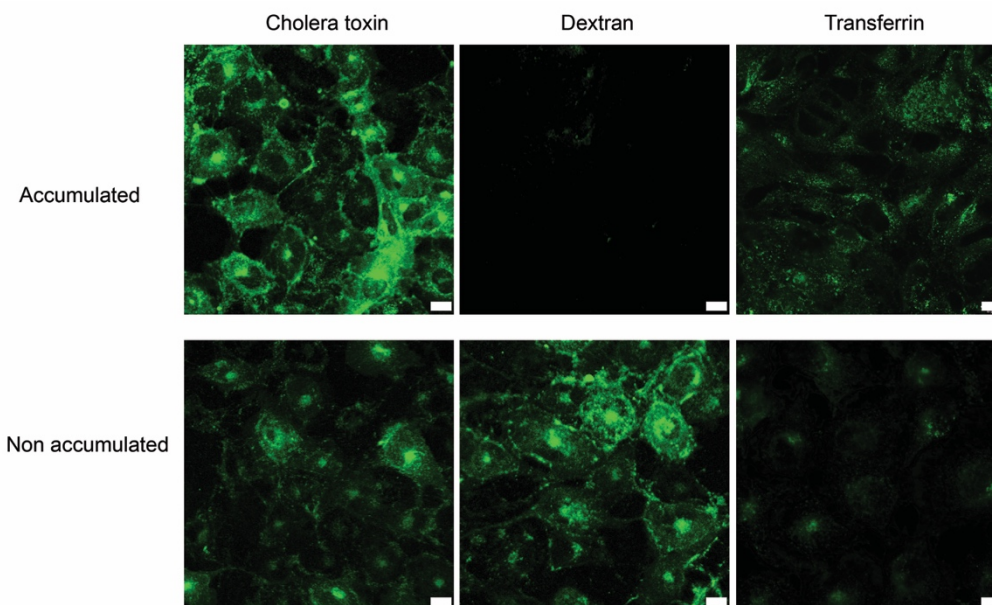


**Figure 2.12 Uptake profile of the fluorescent-labeled compounds in the AuNP accumulated and non-accumulated cells.** After 23 days accumulation of the AuNPs in HUVECs, cells were passaged and incubated with fluorescent-labeled compounds which enter through specific endocytosis pathways. Cholera toxin enters through caveolin-mediated endocytosis, dextran enters through micropinocytosis, and Transferrin enters through clathrin-mediated endocytosis. Scale bars are 10  $\mu\text{m}$ .

As a result, the potential role for exocytosis for the active transport of AuNPs out of the cells was explored, however, no evidence that exocytosis plays a significant role for the removal of AuNPs inside the cells was observed (Figure 2.13). It is likely that cell division plays a predominant role for the dilution of the AuNPs in the new offspring cells [103]. Because the micropinocytosis is inhibited, these two effects were combined to culminate in a gradual decrease of AuNPs inside the cells.

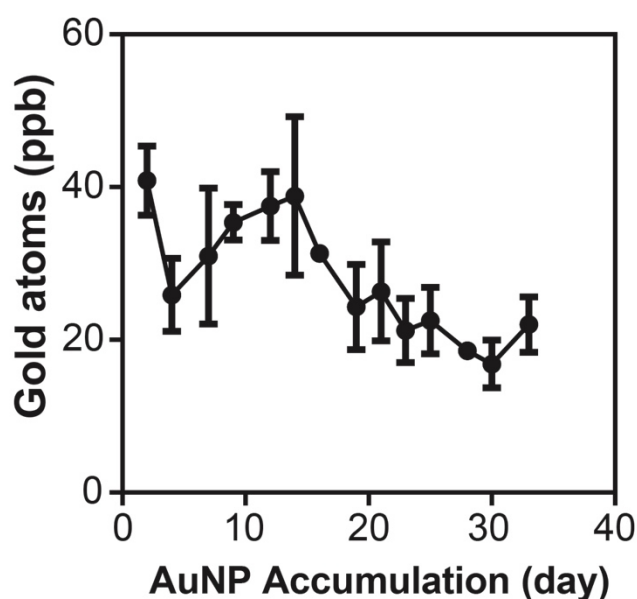


**Figure 2.13 Exocytosis behavior of HUVECs during long-term accumulation of the AuNPs.** ICP-MS analysis of total gold atoms in medium collected before the AuNP exposure. (Error bars show s.e.m, experiments were performed with n=3.)

#### 2.4.5 Determination of the cellular stress during long-term accumulation

Engineered nanomaterials bound to biomacromolecules can cause conformational changes [104] in the structure of proteins, which might result in ER stress through the unfolded protein response (UPR), and trigger oxidative stress [105] through ROS formation. ER stress is generally considered as an adaptive reaction of cells to external stress, and serves as a survival mechanism. This complex stress response is mediated by several molecules, such as PKR-like ER kinase (PERK), activated transcription factor 6 (ATF6), inositol-requiring enzyme 1 (IRE1), and spliced X box-binding protein 1 (sXBP1) [94]. IRE1 is activated in response to the accumulation of unfolded proteins, and acts as a site-specific endonuclease splicing out a 26-nucleotide intron in XBP1 mRNA. Spliced XBP1 mRNA is translated to produce the spliced XBP1 protein, which is a transcription factor and one of the key regulators of the protein-

folding capacity of the cells and ER homeostasis [94]. Therefore, cellular levels of XBP1 and its spliced form, sXBP1 were monitored through polyacrylamide gel electrophoresis (PAGE) and qRT-PCR to evaluate the ER stress at different accumulation time points (Table 2.2). Interestingly, a slight sXBP1 band was observed at the point of highest accumulation (day 12), which became more pronounced at day 16 in the Accumulated group but not observed in the Non-accumulated group (Figure 2.14A). Moreover, there were also slight bands at day 28 and 30 in the accumulated group which were not observed in the non-accumulated group. This result was also confirmed using only the sXBP1 primer in qRT-PCR, where a sharp peak with significant increase of  $201.94 \pm 6.29$  folds of non-accumulated group was seen at day 16. sXBP1 expression was statistically significant to other AuNP accumulated days (Figure 2.14B). Expression profile of sXBP1 correlates with accumulation of the AuNPs inside the cells, which suggests that peak accumulation occurs at day 12 due to slight ER stress, while increased ER stress at day 16 triggers a decline in AuNP accumulation. A recent study [93] implicated more changes in the expression of unfolded protein response gene (*HSPA5*) in one-shot non chronic AuNP (18 nm citrate and PAA coated nanospheres and PAA coated nanorods) exposure model compared to 20 week chronic exposure which contrasts with these findings. The discrepancy might arise from cell type [15, 16] and nanoparticle size [10], shape [11-13] and surface chemistry [9] which were previously shown to be important for cellular response. In addition, another UPR gene *ATF6* was not upregulated in both chronic and non-chronic exposures, which shows that their microarray results might need further confirmation at protein level.

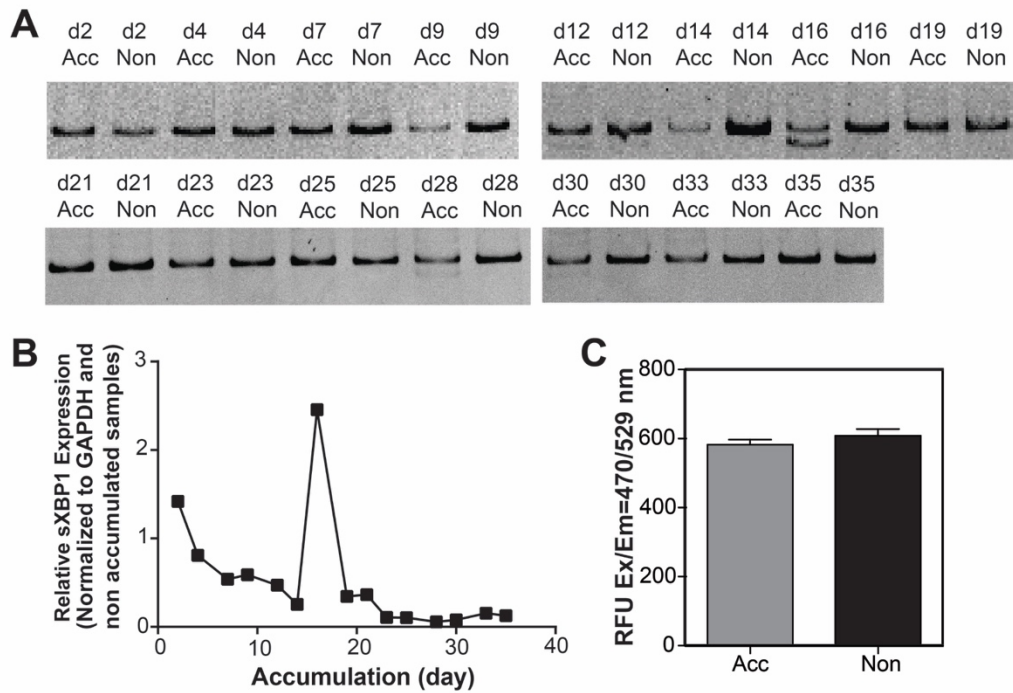


**Figure 2.14 Cellular stress response to long-term accumulation of AuNPs.** RT-PCR analysis of an ER stress indicator (XBP1) in HUVECs at different accumulation time points following 10% polyacrylamide gel electrophoresis (A). qRT-PCR analysis of spliced XBP1 (sXBP1) in HUVECs at different accumulation time points, where expression of sXBP1 was normalized to GAPDH and non-accumulated samples (B). ROS levels were analyzed in AuNP-accumulated and non-accumulated cells after 57 days of accumulation by DCF assay (C) (Error bars show s.e.m, experiment was performed with n=3. Student t-test was applied for statistical analysis.)

Under prolonged ER stress, cells typically ignite a specific cell death program, apoptosis [106]. At the end of 57 days of accumulation, both viability and ROS levels in accumulated and non-accumulated groups were comparable, indicating that long-term accumulation of AuNPs did not induce cell death and ROS formation (Figure 2.15A and Figure 2.14C). Thus, it is likely that the cells exposed to the AuNPs for longer periods develop a survival mechanism via short-term on/off of ER stress followed by inhibition of their micropinocytosis pathway, and thereby control the intracellular concentration of the AuNPs. A link was previously established between

ER stress and endocytosis inhibition in the literature [107], and this cooperative mechanism might possibly serve to control intracellular concentration of engineered nanomaterials.

On the other hand, the proliferative capacity of cells in accumulated group decreased slightly, but significantly, when compared to non-accumulated cells (Figure 2.15B).

One week exposure of low dose of citrate-capped AuNPs (~18 nm in diameter) has previously been reported to trigger a similar decrease in cell proliferation without compromising cell viability [108].

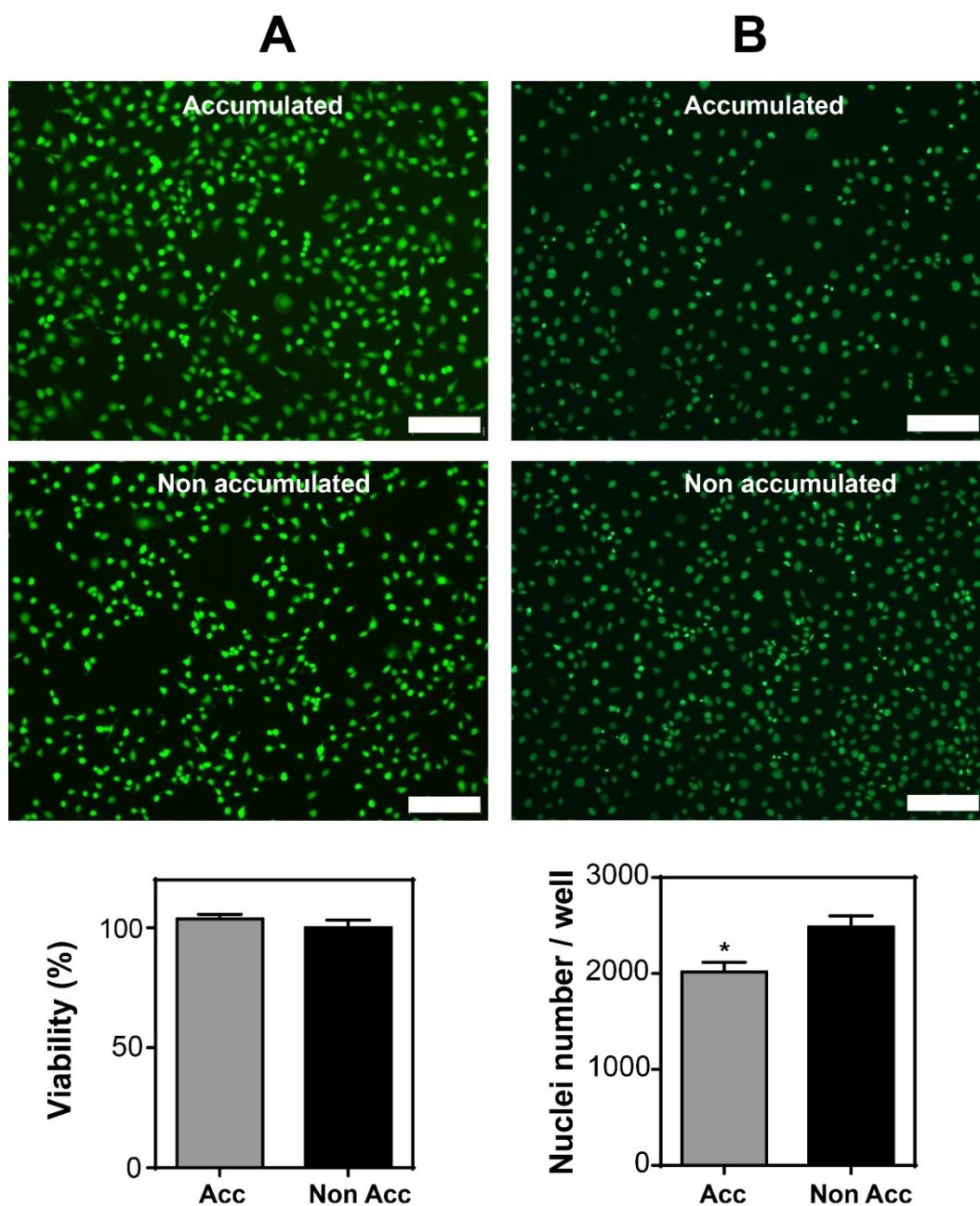


**Figure 2.15 Cellular response to long-term accumulation of AuNPs.** Cytotoxicity of AuNPs after 57 days was assessed with Live / Dead (calcein Am / ethidium homodimer staining) and MTT assay. Live cells were stained green and dead cells were stained red. Student t-test was used for statistical analysis and significance was not found (A). Proliferation of cells after 49 days of accumulation was assessed with Click-iT EdU assay. The nuclei of proliferating cells were stained green. Student t-test shows statistical significance with  $*p < 0.05$  (B). Error bars show s.e.m in all graphics, experiments were repeated with  $n=3$  in both viability and proliferation experiments. Scale bars are  $200 \mu\text{m}$  in all image.

## 2.5 Conclusion

In this work, the toxic impact of chronic exposure and accumulation of the AuNPs on endothelial cells was shown. Even though the AuNPs are largely considered “non-toxic” and “safe” based on the short-term exposure assays, their long-term interaction with the cellular machinery is highly complex and creates major challenges for cells to eliminate the stress caused by its accumulation. To elucidate this, a new *in vitro* accumulation model, which enables assessment at non-lethal exposure doses over an extended period of time, was designed. This platform emulates certain aspects of *in vivo* exposure conditions as well as utilizes a simple-to-implement cell culture model that can be used to directly analyze the long-term effects of other types of nanoparticles accumulated in the cellular environment. The information deduced from the accumulation experiments demonstrates the strength of the model, thereby, paving the way of improving risk assessment methods and extending protocols for the development of alternate cell-based models to better understand the nanomaterial safety and the associated risks. Nevertheless, there are still important challenges and questions that remain to be addressed for the optimal evaluation of long-term nanomaterial toxicity. For example, a more robust method could be developed where cell division and proliferation are inhibited, so the effect of cell division on diluting the intracellular nanoparticles is eliminated. However, the challenge here is to keep cells alive and healthy under the cell cycle arrest conditions for extended periods of time. Ultimately, this and other complementing *in vitro* toxicity models are expected to provide invaluable mechanistic information about cell-nanomaterial interactions at the molecular level as well as enormous practical flexibility for experimental setup



design, thereby significantly reducing the need for animal-based models and the number of animals being sacrificed.

## CHAPTER 3

### 3 Pro-regenerative effects and application of ketone body beta-hydroxybutyrate in intestinal stem cell maintenance and regeneration

*This work is a partial content of a publication under preparation with the following authors:*

*Cheng C.W., Biton M., Haber A.L., **Gunduz, N.**, Eng G., Gaynor L.T., Tripathi S., Kocal-Calibasi G., Rickelt S., Gebert N., Butty V., Moreno M., Iqbal A.M., Bauer-Rowe K.E., Mylonas C., Whary M.T., Levine S.S., Hynes, R.O., Kenudson M.O., Deshpande V., Boyer L.A., Mihaylova M.M., Ori A., Fox J.G., Regev A. and Yilmaz O.H. Endogenous ketones instruct intestinal stem cell fate through Notch signaling. (submitted)*

#### 3.1 The objective

After identification of the *Lgr5*<sup>+</sup> intestinal adult stem cell (ISCs), diverse signaling pathways have been shown to balance stem cell self-renewal and differentiation in response to tissue homeostasis, disease, damage and aging. For example, whether physiological variations in nutrient levels can alter these signaling pathways to regulate stem cell function is less clear. Recent studies show that there are interconnections between physiology, stem cell function and colorectal cancer initiation. For instance, high fat diet enhances stemness and tumorigenicity of intestinal progenitors. Understanding the effects of regulatory mechanisms driven by

dietary nutrients, metabolism, and metabolic intermediates on stem cell function may help development of safer anti-cancer and anti-aging therapies. A metabolic enzyme, hydroxymethylglutaryl CoA synthase 2 (HMGCS2), was highly enriched in *Lgr5*<sup>+</sup> ISCs in previous RNA-seq and proteomics results. HMGCS2 along with carnitine palmitoyltransferase-1 A (CPT1A) determine the metabolic fate of fatty acids in different physiological states such as starvation, fasting, high fat diet, and ketogenic diet. Here, the following questions were investigated : 1)What is the function of this metabolic enzyme in highly cycling *Lgr5*<sup>+</sup> ISCs without physiological stimulation? 2) Does HMGCS2 function in ketogenesis and produce ketone body? 3) What are the consequences in *Lgr5*<sup>+</sup> ISCs and intestine when HMGCS2 is not expressed? 4) Can ISC function and regeneration capacity of intestine be rescued with exogenous ketone body  $\beta$ OHB administration? Therefore, here in this study, the role HMGCS2 and its product  $\beta$ -hydroxybutyrate ( $\beta$ OHB) was interrogated in intestinal tissue via deletion of *Hmgcs2* with a genetically engineered mouse model and compensation capacity of engineered forms of  $\beta$ -hydroxybutyrate ( $\beta$ OHB) in irradiation injury model.

### **3.2 Introduction**

Although it starts with a single cell, fertilized egg, our body consists of different organs, tissues and cell types working in a harmony. Every organ has two main tasks: utilization of metabolites and protection against tissue damage. Neither of these tasks are unique to one organ in our body, however intestine has to perform these tasks continuously while withstanding mechanical forces due to migrating motility complexes, extreme pH variations for chemical digestion and colonization of more than  $10^{13}$  bacteria. These insulting tasks require continuous tissue maintenance and

regeneration to balance tissue protection and efficient nutrient and water absorption. The intestine which has the largest surface area in our body, adopt two important features which are linked closely to fulfill tissue maintenance and regeneration: crypt-villus structure and continuous proliferation. The crypt-villus structure is first described in dissertation of Jonathan Nathanael Lieberkühn in 1745. The intestinal epithelium is covered by millions of crypt-villus units. Later on, in 1893, Bizzozero noticed mitoses occur in the crypt region and newly formed daughter cells move from the crypts to the villi to contribute to the maintenance of intestinal epithelium. Another study in 1947 by Leblond and Stevens showed the self-renewal mechanism and rate of intestinal epithelium by using a mitosis inhibitor, colchicine. After that, Leblond lab investigated the crypt stem cell identity and origin of different epithelial cells in intestine [109]. In agreement with Austrian physician Joseph Paneth, they showed that the crypt base is not only populated by Paneth cells. There is another cell type intermingled between granular post-mitotic large Paneth cells which is very small and narrow and continuously cycling, so-termed as crypt base columnar cells (CBCs). Although Leblond showed CBCs are clonal origin of different cell types in the intestinal epithelium as depicted in Figure 3.1, yet due to lack of sophisticated tools to trace lineage differentiation from a common source, their finding was not the final proof of CBCs as stem cells [110].

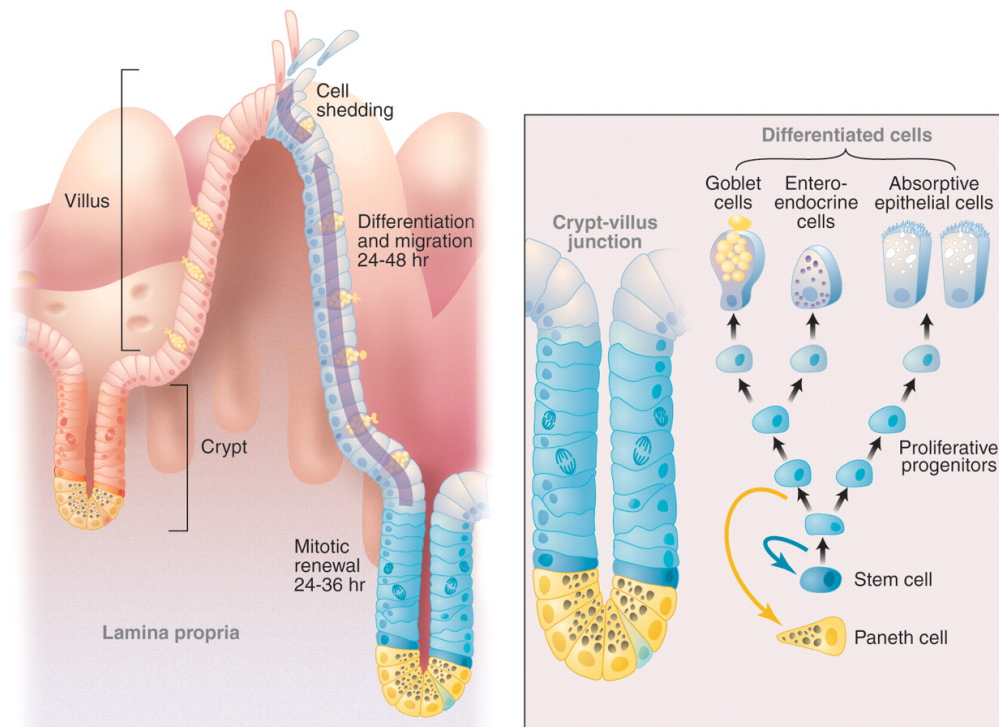


**Figure 3.1 The anatomy of the small intestinal epithelium.** The epithelium is shaped into crypts and villi (**left**). The lineage scheme (**right**) depicts the stem cell, the transit-amplifying cells, and the two differentiated branches. The right branch constitutes the enterocyte lineage; the left is the secretory lineage. Relative positions along the crypt-villus axis correspond to the schematic graph of the crypt in the center. Reprinted with the permission from [111] Copyright (2019) Science.

Substantial progress was done with mutagenesis studies by Winton and Bjerknes to show clonal origin of cells in the intestinal epithelium [112, 113]. After accelerated researches about crypts, stem cell zone and cellular compositions, different signaling pathways control stemness and differentiation in intestinal epithelium [114]. Wnt pathway is one of them and shown deregulated in colon cancer cell line which confirms driver role of Wnt in CBCs stemness and crypt proliferation. With the transcriptomics and proteomics studies showed Wnt-controlled genes and prominent one is *Lgr5*, Leucine rich repeat-containing G-protein coupled receptor which later defined as stem cell marker of intestinal epithelium. Identification of *Lgr5* as stem cell marker brought

new insight into intestinal stem cell biology through coupling *Lgr5* locus with inducible Cre recombinase [115]. In addition to Wnt and Wnt-target genes, BMP, Notch, Hippo, and EGF/EphB signaling pathways are also major regulators of stem cell maintenance and differentiation [114]. Deregulations in these signaling cascades as a result of mutation are the main reasons of cancer and other pathophysiological states of intestine. In addition to these molecular mechanisms, recent studies demonstrate the role of dietary nutrients, the physiological state of body and metabolites in the maintenance of stem cell and homeostasis of tissues [116]. Systemic dietary regimens such as calorie restriction controls stem cell numbers and functions through regulating mTORC1 and SIRT1 both in ISCs and Paneth cells [117, 118]. Furthermore, high-fat diet modulated peroxisome proliferator-activated receptor delta (PPAR-d) program activation augments not only the number and function of *Lgr5*<sup>+</sup> ISCs but also their tumor initiating capacity [119]. High-fat diet also controls ISC function through phospholipid remodeling, cholesterol biosynthesis, and Notch signaling [120, 121]. Vitamins are also important in stem cell function and low level of vitamin D compromises the function of *Lgr5*<sup>+</sup> ISCs [122]. Recently, fasting induced fatty acid oxidation through PPAR/CPT1a was found to augment ISC function in aging and regeneration [123]. Although the effects of diet on ISC function have also been demonstrated with these recent studies, the effect of endogenous metabolites is not well understood. Here, in this study, the role of the ketogenic enzyme HMGCS2 and its product  $\beta$ -hydroxybutyrate ( $\beta$ OHB) were investigated in intestinal stem cell maintenance and differentiation via deletion of *Hmgcs2* in a genetically engineered mouse model and compensation capacity of the engineered forms of  $\beta$ OHB in an irradiation injury mouse model.

### 3.3 Experimental methods

#### 3.3.1 Mice and treatments

Mouse strains. Functional validation studies widely utilize genetically engineered mouse models (GEMMs) to manipulate the genes of interest in mouse genome. For this purpose, conditional alleles are used to analyze the function of a gene in a tissue-specific or temporal manner during different development time points. To validate whether *Hmgcs2* expressing cells have ISC function and whether *Hmgcs2* is necessary for ISC function and maintenance, *Hmgcs2-lacZ* reporter and conditional loxP mice were generated using a knockout-first strategy depicted in Figure 3.2 [124]. In contrast to other standard designs, knockout-first strategy has advantage of combining both a reporter and conditional mutation. Briefly, vector design was achieved by a gene trapping cassette consisting of mouse *En2* splicing acceptor (SA), reporter (*LacZ*) and promoter-driven selection (Neomycin, Kanamycin) genes that were inserted into upstream of a critical exon of a gene (intron region) between two identical FRT sites. The initial allele (*Hmgcs2*-Vector, V) (KOMP: PG00052\_Z\_4\_A06) can be modified in embryonic stem (ES) cells or crosses to *Flp* or *cre* mice. Conditional allele (*Hmgcs2*-loxP, L) was generated by flanking FRT sites with Flippase (Flp) recombinase or by crossing vector mice with Flippase mice (FLPe knockin mice, Jackson Labs #003946). Null allele (*Hmgcs2*<sup>-/-</sup>, KO) was generated through splicing of the *LacZ* trapping element and a critical exon by FLP and/or CRE recombinases. To validate the function of *Hmgcs2* in ISCs and intestine, conditional *Hmgcs2*<sup>L/L</sup> mice were crossed to *Lgr5-eGFP-IRES-CreERT2* [115] and to *Lgr5-CreERT2; tdTomatoLSL* [125] reporter mice

separately. CRE-mediated excisions in sorted GFP<sup>+</sup> cells and in tdTomato<sup>+</sup> crypt cells were both confirmed by PCR. The *Lgr5-eGFP-IRES-CreERT2* mice were previously described [115]. *Lgr5-CreERT2*; *tdTomatoLSL* were generated by crossing *Lgr5-IRES-CreERT2* mice (a gift from Dr. Hans Clevers) to *tdTomato<sup>LSL</sup>* mice (Jackson labs #007909).

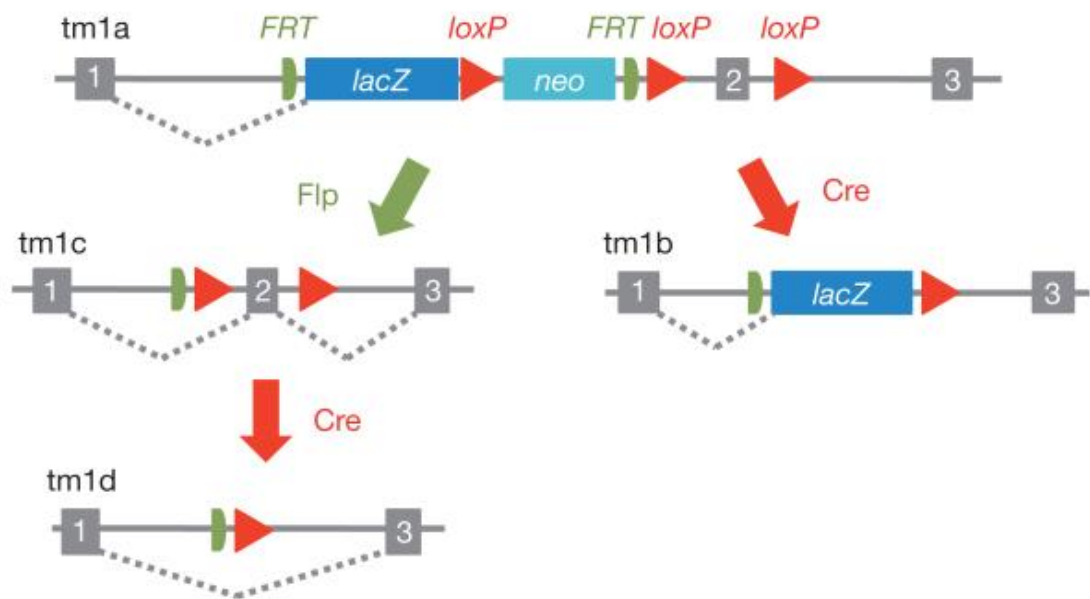


**Figure 3.2 Schematic of the “knockout-first” conditional allele which is generated with gene trapping strategy.** The initial allele (tm1a) contains a reporter (LacZ) and selection (Neomycin) cassettes inserted into upstream of a critical exon of a gene (intron region) to create a null allele of the gene. LacZ tagged null allele, tm1b, produced by deletion of the critical exon and the Neomycin cassette using a Cre recombinase that recognizes loxP sites. Conditional allele, tm1c, is generated by deletion of LacZ and Neomycin cassettes by using a site-specific Flippase (Flp) recombinase that recognizes identical two FRT sites. Tissue specific Cre recombinase deletes the critical exon between loxP sites to generate a frameshift mutation, tm1d. The figure is adapted from Skarnes, W.C., et al. with the permission of Springer Nature [124].

Tamoxifen treatment. 1% (wt/v) Tamoxifen (Sigma, T5648) was dissolved in 10:90 Ethanol: Sunflower oil (v/v) mixture in room temperature. Intraperitoneal (i.p)



tamoxifen injections were administered as 2 mg per 25 g of body weight and indicated in figure legends.

*Irradiation experiments.* A lethal dose of ionizing irradiation at 7.5 Gray was administered to mice twice with 6 h intervals by using <sup>137</sup>-caesium source (Gammacell 40E, Theratronics). Mice were monitored every day and intestine tissues were collected for histology ~4-5 days after ionizing irradiation (XRT). Lineage tracer, *Lgr5-IRES-CreERT2; Rosa26<sup>LSL-tdTomato</sup>* reporter mouse model was used in irradiation experiments for tracing permanent tdTomato labeling of the stem cells and their progeny over time upon induction after 24 h with Tamoxifen. All *in vivo* experiments were performed with approval from the Committee for Animal Care at MIT and under supervision of the Department of Comparative Medicine at MIT.

### **3.3.2 $\beta$ -hydroxybutyrate ( $\beta$ OHB) measurements**

Intestinal crypts were isolated as described above and aliquoted into two samples. Samples were pelleted (centrifuged at 300 g for 5 min) and re-suspended in lysis buffer of BCA assay (Thermofisher, 23225) for measuring total proteins and for  $\beta$ OHB measurements (Cayman, #700190). Level of crypts  $\beta$ OHB was normalized to total proteins of each sample.

### **3.3.3 Crypt isolation and culturing**

Crypt isolation was performed as previously reported [119, 126]. Briefly, small intestines were removed, flushed with cold PBS, opened longitudinally and the mucous layer was scraped with fingers gently. Then, small intestines were chopped

into big pieces and incubated on ice with PBS+/- EDTA (10 mM) for 30-45 min. Incubated tissues were washed with cold PBS to remove EDTA and crypts were mechanically separated from the connective tissue by shaking or scraping with glass, and then filtered with a 70  $\mu\text{m}$  mesh into a 50 mL conical tube to remove villus material and tissue fragments. After centrifugation at 300g for 5 min, crypts were dissociated in crypt culture media and embedded in Matrigel<sup>TM</sup> (Corning 356231, growth factor reduced) at 5-10 crypts per  $\mu\text{L}$  and 50  $\mu\text{L}$  or 20  $\mu\text{L}$  Matrigel<sup>TM</sup> / crypt droplets were placed onto flat bottom of 24- or 48- well plates (Corning 3548). Then, Matrigel<sup>TM</sup> crypt culture was placed into 37 °C incubator for polymerization for around 20-30 minutes. 600 or 300  $\mu\text{L}$  of crypt culture medium was then overlaid onto the Matrigel<sup>TM</sup> drops, changed every three days, and maintained at 37 °C in fully humidified chambers containing 5% CO<sub>2</sub>. Unless otherwise noted, crypt culture media was prepared as following based on previous studies [119, 126, 127]. Advanced DMEM (Gibco) was supplemented with EGF 40 ng ml<sup>-1</sup> (R&D), Noggin 200 ng ml<sup>-1</sup> (Peprotech), R-spondin 500 ng ml<sup>-1</sup> (R&D, Sino Bioscience or [128]), *N*-acetyl-L-cysteine 1  $\mu\text{M}$  (Sigma-Aldrich), N2 1X (Life Technologies), B27 1X (Life Technologies), CHIR99021 3  $\mu\text{M}$  (LC laboratories), and Y-27632 dihydrochloride monohydrate 10  $\mu\text{M}$  (Sigma-Aldrich). Colony-forming efficiency was calculated by dividing healthy organoid number to crypt number per well at specified time points of culture (~3-7 days).

Crypts were also used for isolation of ISCs, progenitor and Paneth cells. Isolated ISCs and Paneth cells were used for organoid initiation assay. Briefly, after isolating crypts from *Lgr5-eGFP-IRES-CreERT2* knockin mice [115], crypts were dissociated with 1X TrypLE<sup>TM</sup> Express Enzyme (Gibco 12604013, no phenol red)

at 32°C incubator for 1 min and gently quenched with S-MEM (Gibco, 11380037, without calcium and L-glutamine) and then centrifuged at 300 g for 5 min, 4 °C. The pellet was resuspended in cell labeling antibody cocktail (Table 3.1) and incubated on ice for 20 min. After washing with S-MEM, the individual cell pellet was resuspended in the S-MEM containing the viability dye 7-AAD (Life Technologies) and filtered twice with 40 µm mesh. ISCs were isolated as  $Lgr5-EGFP^{hi}Epcam^{+}CD24^{low/-}CD31^{-}Ter119^{-}CD45^{-}7-AAD^{-}$ .  $EGFP^{low}$  progenitors were isolated as  $EGFP^{low}Epcam^{+}CD24^{low/-}CD31^{-}Ter119^{-}CD45^{-}7-AAD^{-}$ , and Paneth cells from small intestine were isolated as  $CD24^{hi}SSC^{hi}Lgr5-EGFP^{-}Epcam^{+}CD31^{-}Ter119^{-}CD45^{-}7-AAD^{-}$  with a BD FACS Aria cell sorter into supplemented crypt culture medium for culture.

**Table 3. 1 Cell labeling antibody cocktail for sorting ISCs and Paneth cells from crypts.**

<b>Antibody</b>	<b>Brand</b>	<b>Dilution / Purpose</b>
CD45-PE	eBioscience, 30-F11	1:500 / Lymphocyte common antigen (myeloid cells)
CD31-PE	Biologend, Mec 13.3	1:500 / Endothelial cells in blood vessels
Ter119-PE	Biologend, Ter119	1:500 / Red blood cells
CD24-PacBlue	Biologend M1/69	1:300 / Paneth and endocrine cells
CD117-APC/Cy7	Biologend 2BS	1:300 / Paneth and endocrine cells
EPCAM-APC	eBioscience, G8.8	1:300 / Epithelial cells
7-AAD	Life Technologies	1:500 / Dead cells

$Lgr5-GFP^{hi}$  ISCs and  $CD24^{+}c-Kit^{+}$  Paneth cells were sorted into separate tubes and centrifuged at 300 g for 5 min and mixed in a 1:1 ratio and re-suspended in the

appropriate volume of crypt culture medium seeded onto 20-25  $\mu\text{L}$  Matrigel<sup>TM</sup> (Corning 356231 growth factor reduced) containing 1  $\mu\text{M}$  JAG-1 protein (AnaSpec, AS-61298) in a flat bottom 48-well plate (Corning 3548). After polymerization of the Matrigel<sup>TM</sup> and cells at 37 °C in incubator for 30 min, 300  $\mu\text{L}$  of crypt culture medium was added on top of each well. The crypt media was changed every third day.

### **3.3.4 Immunohistochemistry, Immunofluorescence and in situ Hybridization**

Tissue preparation for paraffin embedding: As previously described [117, 119], small intestines were first flushed with 1X PBS and then 10% formalin. Tissues were placed in cassettes after spiral-rolling and fixed in 10% formalin ON (~18 h). Next day, tissue cassettes were placed in 70% ethanol and dehydrated ON (~18 h). After paraffin embedding, tissues were sectioned for haematoxylin-and-eosin-staining (H&E), Alcian Blue Periodic Acid Schiff staining (AB/PAS), immunohistochemistry (IHC), immunofluorescence (IF) and in situ hybridization (ISH).

Organoid preparation for paraffin embedding: Cultured and treated organoids were harvested by dissolving Matrigel<sup>TM</sup> with cold PBS and centrifuged at 300 g for 5 min at 4 °C. Supernatant was removed and pelleted organoids were carefully resuspended in a small amount of pre-heated (60 °C) HistoGel (Thermo Scientific) and droplets were placed on a pre-cooled weighing boot and incubated on ice or -20 °C for rapid polymerization. Then, solid HistoGel droplets were carefully placed in tissue cassettes and fixed in 10% formalin ON (~18 h). Next day, tissue cassettes were placed in 70% ethanol and dehydrated ON (~18 h).

For IHC and IF staining: Briefly, for IHC and IF, antigen retrieval was performed with Borg Decloaker RTU solution (Biocare Medical) in a pressurized Decloaking Chamber (Biocare Medical) for 3 min. Antibodies used for IHC were: rabbit anti-Hmgcs2 (1:500, Abcam ab137043), rabbit monoclonal OLFM4 (1:10,000, gift from CST, clone PP7), rabbit polyclonal lysozyme (1:250, Thermo RB-372-A1), and rabbit polyclonal anti-RFP (1:500, Rockland 600-401-379). Biotin-conjugated secondary donkey anti-rabbit antibodies were used from Jackson ImmunoResearch. The Vectastain Elite ABC immunoperoxidase detection kit (Vector Labs PK-6101) followed by Dako Liquid DAB+ Substrate (Dako) was used for visualization. Antibodies used for IF were: goat anti-GFP (1:500, gift from Abcam), and rabbit anti-Hmgcs2 (1:500, Abcam ab137043). TSA<sup>TM</sup> Alexa Fluor 488 tyramide signal amplification kit (Life Technologies, T20948) was used for signal amplification for HMGCS2 and 568 secondary antibody (Invitrogen) for GFP. Slides were stained with DAPI (2 µg/mL) for 1 min and covered with Prolong Gold (Life Technologies) mounting media. All antibody incubations involving tissue or sorted cells were performed with Common Antibody Diluent (Biogenex).

Organoids were fixed with 4% PFA, permeabilized with 0.5% TritonX-100/PBS, rinsed with 100 mM glycine/PBS, blocked with 10% Donkey serum/PBS, incubated overnight with primary antibody at 4 °C, rinsed and incubated with Alexa Fluor 568 secondary antibody (Invitrogen), and mounted with Prolong Gold (Life Technologies) mounting media.

For IHC and ISH co-staining: Single molecule ISH was performed using Advanced Cell Diagnostics RNAscope 2.0 HD Detection Kit (Fast Red dye) for the following probe: *Mm-Lgr5*. For IHC and ISH co-staining, after signal detection of *Lgr5* ISH,

slides were dried and proceeded with regular IHC for HMGCS2 staining.

### **3.3.5 $\beta$ -hydroxybutyrate encapsulated PLGA nanoparticle synthesis**

$\beta$ OHB encapsulated poly (lactic-co-glycolic acid) (PLGA) nanoparticles were synthesized via double emulsion technique [129] as depicted in Figure 2. Briefly, 0.5 g of PLGA (LG 50:50 Mn 5,000-10,000 Da acid endcap) was dissolved in 2.5 mL of dichloromethane (DCM), and 1 mL  $\beta$ OHB solution (500 mg/mL) was added to the solution and sonicated for 30 sec (Hanchen Instrument, 300 w 3 mm probe). The emulsion was then transferred to 50 mL of cold soy lecithin (Alfa Aesar) (10 mg / mL in PBS) and was sonicated for 30 s twice, with a 30 sec wait interval. The DCM was then removed from the solution via stirring for 12 h at 4 °C. The particles were isolated and washed via centrifugation (5000 g for 30 min x 3 times) and frozen for long term storage.

### **3.3.6 $\beta$ -hydroxybutyrate oligomer synthesis**

Poly( $\beta$ -hydroxybutyrate) (PHB) is polymerized form of  $\beta$ -hydroxybutyrate and produced and stored by a large number of bacteria as an energy source similar to lipid storage in mammals. Despite monomer form of  $\beta$ -OHB, PHB is water-insoluble and resistant to degradation. PHB can serve as biodegradable polymers for biomedical applications and thermos plastic [130]. PHB has 3 different subtypes based on different numbers of  $\beta$ -OHB monomer units: (i) high molecular weight PHB (storage PHB) with over >10000 monomers (ii) low molecular weight PHB (oligo-PHB) with 100-300 monomers (iii) short-chain PHB (cPHB) with low numbers of monomers < 30 [131]. With the inspiration from nature, oligomer form of  $\beta$ -OHB (oligo- $\beta$ OHB) between 5-

7 monomer residues was synthesized as depicted in Figure 3.3. Anhydrous solvents were saturated with argon and purified with two alumina-activated columns. Schlenk techniques were used for air sensitive reactions and compounds.

First, *R* configuration of  $\beta$ -OHB, (*R*)-3-hydroxybutanoic acid was synthesized. NaOH (3.52 g, 88 mmol) in water (20 mL) was slowly added to a solution of methyl (*R*)-3-hydroxybutyrate (9.45 g, 80 mmol) in MeOH (10 mL). The mixture was stirred at RT for 24 h. Later, the reaction mixture was acidified to pH = 1 (pH paper) by using 4 M HCl. The acidified mixture was concentrated under vacuum to about 30 mL. NaCl was then added to this solution until saturation. The mixture was extracted with EtOAc (40 mL X 5). The combined organic phase was dried over MgSO<sub>4</sub>. The solvent was removed under vacuum to give a colorless liquid (6.86 g, 82% yield). The material was stored at -80 °C until used in the next step.

Second, the pentolide, hexolide, and heptolide of (*R*)-3-hydroxybutyric acid were synthesized according to a procedure reported by Seebach and co-workers [132]. Et<sub>3</sub>N (1.26 g, 1.73 mL, 12.4 mmol) was added to (*R*)-3-hydroxybutanoic acid (1.00 g, 9.6 mmol) in anhydrous THF (1.6 mL) which resulted with a large amount of precipitate formation. Then 2,4,6-trichlorobenzoyl chloride (2.34 g, 1.50 mL, 9.6 mmol) was added to precipitate at 0 °C. The reaction was stirred at 0 °C for 30 min and gradually warmed to RT over a period of 1.5 h. The thick white slurry was diluted with toluene (10 mL) and suction-filtered. The solid was then washed with another portion of toluene (10 mL). The filtrate (20 mL) was then added by a syringe pump to a solution of DMAP (122 mg, 1.0 mmol) in anhydrous toluene (400 mL) over 4 h. The reaction mixture was diluted with Et<sub>2</sub>O (200 mL) and washed with HCl (1 M, 100 mL  $\times$  2). The organic phase was then washed with saturated NaHCO<sub>3</sub> aq. (100 mL) and brine

(100 mL). The organic phase was dried over  $\text{MgSO}_4$ . The solvents were removed under vacuum to give a slightly yellow mixture of oil and white crystalline solid. The crude product was purified by column chromatography (silica gel,  $\text{Et}_2\text{O}:\text{hexanes}=7:3$ ). The product was visualized on TLC using  $\text{KMnO}_4$  stain.

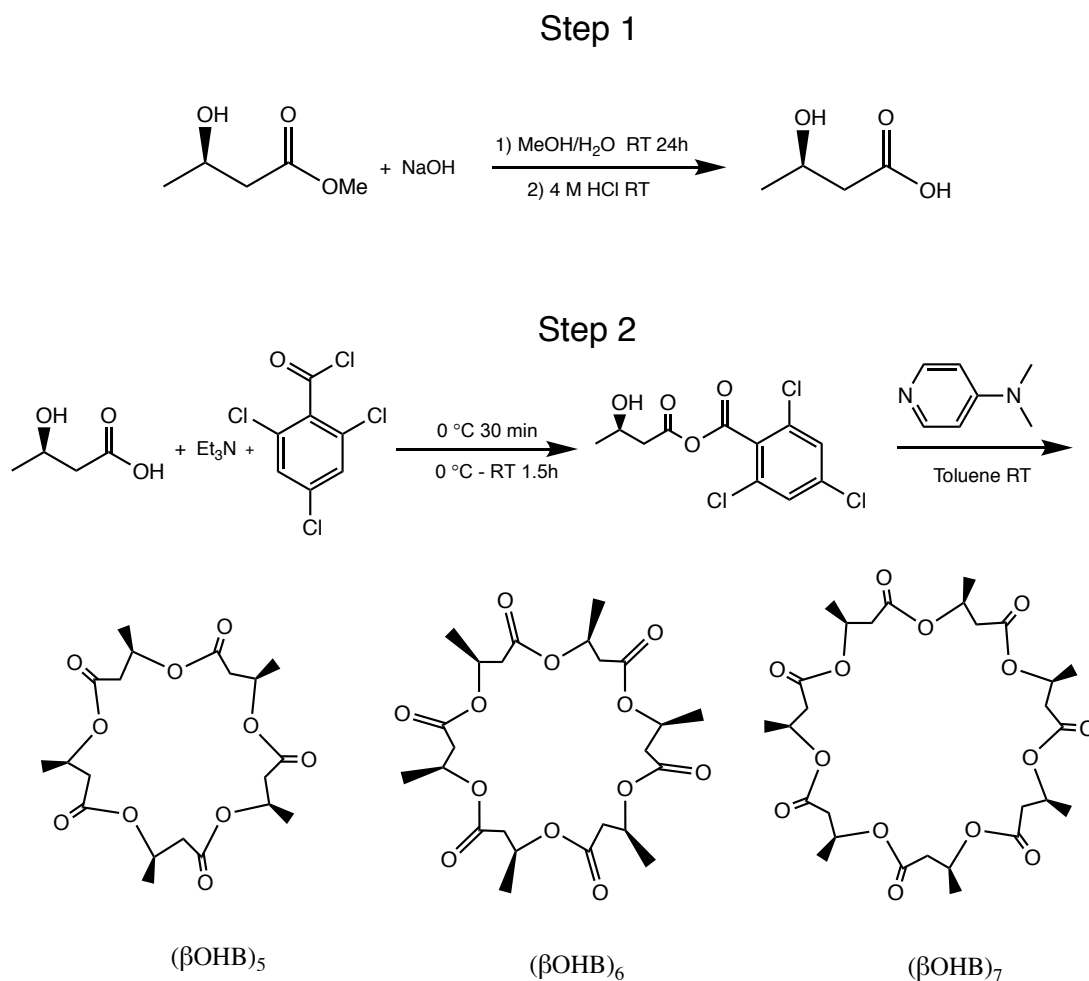


**Figure 3.3 Oligo- $\beta\text{OHB}$  synthesis steps.** Step 1 depicts synthesis of (*R*)-3 hydroxybutanoic acid and Step 2 depicts synthesis of pentolide, hexolide and heptolide of (*R*)-3 hydroxybutanoic acid.



### 3.4 Results and Discussion

#### 3.4.1 Ketogenic enzyme HMGCS2 is enriched in intestinal stem cells

Specific pathways are enriched in stem cells and their definition improves understanding of the molecular mechanisms that control stem cell self-renewal and differentiation. Precision and sensitivity of molecular analysis are increasing with developing technologies / techniques in science. One of these techniques is RNA-seq which is widely used to reveal expression patterns of genes in a biological sample. To identify enriched genes in ISCs, previously published RNA-seq data [119, 123] from populations of flow sorted *Lgr5*-GFP<sup>hi</sup> ISCs, *Lgr5*-GFP<sup>low</sup> progenitors [133], and CD24<sup>+</sup> c-Kit<sup>+</sup> Paneth cells [134] from *Lgr5-eGFP-IRES-CreERT2* knock-in mice was analyzed [115]. The focus of analysis was the genes that were differentially expressed between ISCs and progenitors (filtered by two group comparison  $p/\rho_{\max}=5e-4$ ;  $p<0.14$ ,  $q<0.28$ ). Paneth cells were excluded from analysis because Paneth cells are a highly specialized cell type of crypt and display different molecular programs. From population-based RNA-seq results 3-Hydroxy-3-Methylglutaryl-CoA Synthase 2 (*Hmgcs2*) showed a different expression pattern ( $p=0.002$ ;  $q=0.046$ ) between *Lgr5*<sup>+</sup> ISCs (GFP<sup>hi</sup> cells) and progenitors (GFP<sup>low</sup> cells) (Figure 3.4B). HMGCS2 is a metabolic enzyme that resides in mitochondria and regulates ketogenesis (Figure 3.4A). Although previously published data did not show expression of HMGCS2 in intestine, they did not explain which part of the intestine was used for immunoblotting [135]. This result exhibits excellent agreement with the published data about definitive *Lgr5*<sup>+</sup> ISC signatures [136] where differential expression of HMGCS2 in ISCs confirmed both transcriptomic and proteomic techniques. The enrichment of *Hmgcs2*

expression in *Lgr5*<sup>+</sup> ISCs was verified with co-staining procedures at both the mRNA level and protein levels. Dual ISH / IHC and IHC / IHC confirmed that HMGCS2 expression is restricted to crypt base cells and overlap with *Lgr5*<sup>+</sup> cells (Figure 3.4D and 3.4E). On the other hand, ketogenesis mostly occurs in hepatic tissue and its products, ketone bodies, are exported to extra-hepatic tissues in specific physiological states such as fasting, ketogenic diet, and starvation. Therefore, expression of metabolic genes often fluctuates depending on physiological states and dietary regimens. To validate whether expressed HMGCS2 is metabolically functional or not,  $\beta$ OHB levels were measured in sorted cells.  $\beta$ OHB levels were highest in *Lgr5*-GFP<sup>hi</sup> ISCs followed by *Lgr5*-GFP<sup>low</sup> progenitors and then Paneth cells (Figure 3.4C). However high  $\beta$ OHB levels in ISCs and progenitors dropped below the level of Paneth cells after *Hmgcs2* loss (dotted line Figure 3.4C). Up to now, enrichment of *Hmgcs2* in *Lgr5*<sup>+</sup> ISCs is shown at only transcriptomic and proteomics levels, however, expression of *Hmgcs2* was previously shown in colon of mice [135] and this expression is regulated through short-chain fatty acid (SCFA) in germ-free and conventional rats [137]. Based on these results *Hmgcs2* might play an important role in the maintenance of *Lgr5*<sup>+</sup> ISCs in intestine. To investigate the role of *Hmgcs2*, heterozygous *Hmgcs2-lacZ* (i.e. *Hmgcs2*<sup>V/+</sup>) reporter mice were engineered to sort *Hmgcs2-lacZ*<sup>+</sup> cells from crypts for organoid assay. Crypts were dissociated to single cells and stained with EpCAM, a fluorescein di- $\beta$ -D-galactopyranoside (FDG) substrate of *lacZ* and 7AAD. Live crypt cells (7AAD<sup>-</sup>EpCAM<sup>+</sup>) were sorted into two populations as FDG<sup>+</sup> or FDG<sup>-</sup> cells and cultured in Matrigel. FDG<sup>+</sup> cells are capable of organoid forming while FDG<sup>-</sup> cells could not generate organoids (Figure 3.5A and

B). These results along with population RNA-seq and co-expression of HMGCS2 in *Lgr5*<sup>+</sup> ISC confirm that HMGCS2<sup>+</sup> cells have functional stem cell feature.

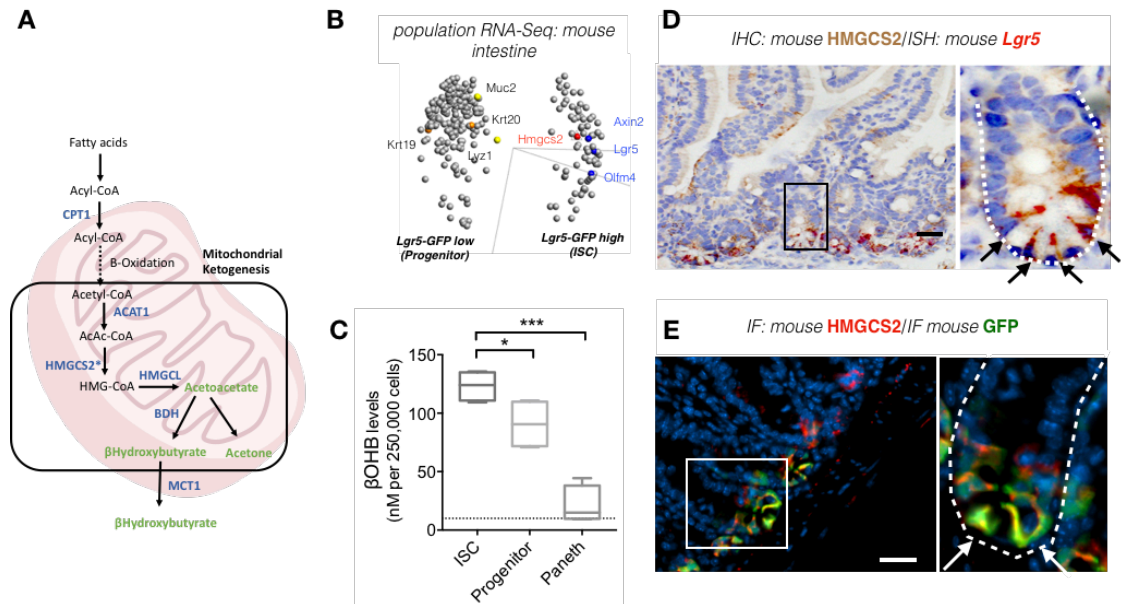


**Figure 3.4 HMGCS2 is enriched in *Lgr5*<sup>+</sup> intestinal stem cells.** **A**, Schematic representation of mitochondrial ketogenesis and enzymes \* indicates the rate-limiting step. **B**, Principal component analysis (PCA) for genes differentially expressed in *Lgr5*-GFP<sup>low</sup> progenitors versus *Lgr5*-GFP<sup>hi</sup> ISCs. Variance filtered by  $(\rho/\rho_{\max})=5e-4$ ;  $p=0.14$ ,  $q=0.28$ ; plot/total: 253/45578 variables. *Axin2*, axin-like protein 2; *Hmgcs2*, 3-Hydroxy-3-Methylglutaryl-CoA Synthase 2; *Lgr5*, Leucine-rich repeat-containing G-protein coupled receptor 5; *Olfm4*, Olfactomedin 4; n=4 mice. **C**, Relative  $\beta$ -hydroxybutyrate ( $\beta$ OHB) levels in flow-sorted *Lgr5*-GFP<sup>hi</sup> ISCs, *Lgr5*-GFP<sup>low</sup> progenitors and Paneth cells. 250,000 cells of each cell population were directly sorted into the assay buffer and immediately processed for  $\beta$ OHB measurement. Dashed line indicated the detection limit of the colorimetric assay. n=8 samples per population from 4 mice. The data was expressed as box-and-whisker 10 to 90 percentiles. \* $p<0.05$ , \*\* $p<0.01$ , \*\*\* $p<0.005$ , n=5 mice. **D**, HMGCS2 protein expression by immunohistochemistry (IHC, brown) and *Lgr5* expression by ISH (red). White-dashed line defines the intestinal crypt and black arrows indicate HMGCS2<sup>+</sup> cells. The image represents one of the 3 biological replicates. Scale bar, 50  $\mu$ m. **E**, HMGCS2 protein expression by immunohistochemistry (IHC, brown) and *Lgr5*-GFP expression by IHC (green). The white-dashed line defines the intestinal crypt and black arrows indicate



### 3.4.2 Loss of *Hmgcs2* attenuates ISC number and function

Cre-lox recombination system is widely used to manipulate and study a gene of interest *in vivo* with tissue specific promoters. Validation studies showed that *Hmgcs2* marks *Lgr5*<sup>+</sup> ISCs. To investigate the role *Hmgcs2* and its loss on stem cell maintenance, a conditional knockout mouse model was used. However up to now, intestinal deletion of *Hmgcs2* was not shown in literature. For this purpose, two separate tamoxifen-inducible conditional alleles were designed (for detail, see Materials and Methods, section 3.3.1 Mouse strains): The first model is the *Hmgcs2*<sup>loxP/loxP</sup>; *Lgr5-EGFP-IRES-CreER*<sup>T2</sup> reporter mouse, where the *Lgr5* knock-in allele has mosaic expression in the intestine [115] and permits isolation of *Lgr5*-GFP<sup>hi</sup> ISCs by flow cytometry [133] and the deletion of *Hmgcs2* in the GFP<sup>hi</sup> subset of ISCs upon induction with. This model is widely used in intestinal stem cell biology field to quantify GFP<sup>hi</sup> ISCs and GFP<sup>low</sup> progenitors and isolate ISCs for organoid culture [117, 119, 123]. Complete deletion of *Hmgcs2* in ISCs is not possible with this model due to mosaic expression of *Cre* recombinase in *Lgr5*<sup>+</sup> ISCs. Although there are other CreER mouse strains such as *Villin-CreER*<sup>T2</sup>, *Olfm4-CreER*<sup>T2</sup> to manipulate genes for functional analysis in intestinal development, physiology, aging, and disease. Analysis of the function of gene in ISCs specifically requires deletion in ISCs. Therefore, a second model, *Hmgcs2*<sup>loxP/loxP</sup>; *Lgr5-IRES-CreER*<sup>T2</sup>; *Rosa26*<sup>LSL-tdTomato</sup> reporter mouse (lineage tracer mouse model) (kind gift of Hans Clevers ) was used in which *Cre* recombinase deletes *Hmgcs2* upon tamoxifen administration in nearly all *Lgr5*<sup>+</sup> ISCs and labels *Hmgcs2*-null stem cells and their progeny over time with tdtTomato [125]. 3 weeks ablation of *Hmgcs2* in *Lgr5-GFP* reporter mice (Figure 3.7A) caused a 50% decrease in the frequencies of *Lgr5-GFP*<sup>hi</sup> ISCs and *Lgr5-GFP*<sup>low</sup> progenitors (Figures 3.6B and

3.6C). When flow sorted *Hmgcs2*-null ISC were co-cultured with WT Paneth cells, they showed 42.9% fewer and 34.6% smaller organoids compared to WT ISCs, which indicates that loss *Hmgcs2* in ISCs impairs organoid initiating capacity (Figures 3.6D and 3.6E). Moreover, after tamoxifen administration in the *Lgr5*-tdTomato lineage tracer mice, intestine tissues were collected at different time points and the number of stem cells were analyzed with Olfactomedin 4 (OLFM4) staining, a marker co-expressed by *Lgr5*<sup>+</sup> ISCs and early progenitors. *Hmgcs2* loss caused a gradual reduction in the number of OLFM4 positive cells, which was 37% fewer compared to the controls at the end of 17 days of tamoxifen induction (Figure 3.7).

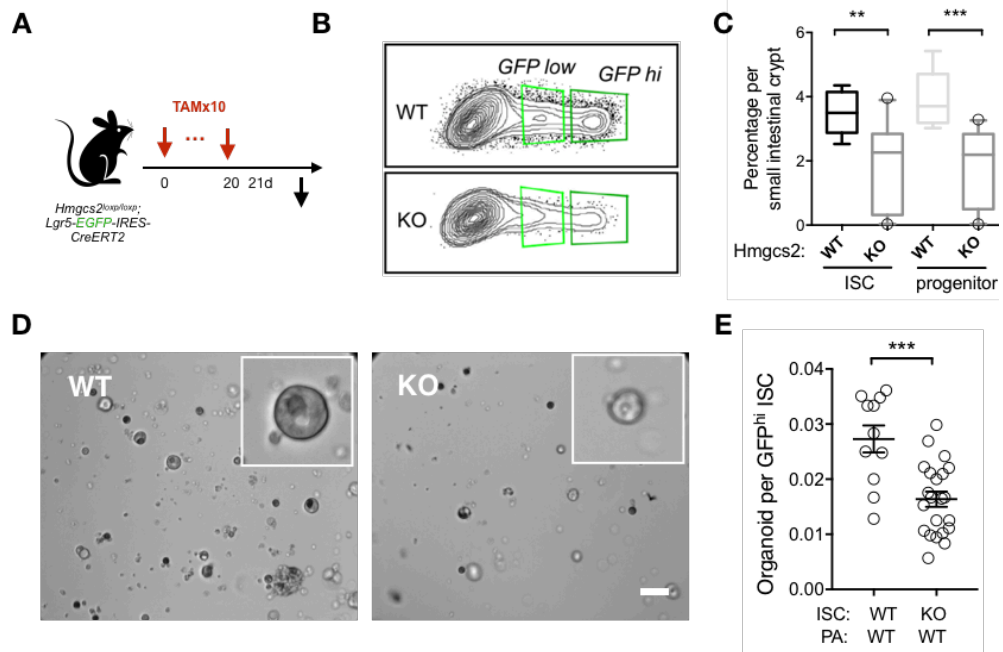


**Figure 3.6 Loss of Hmgcs2 compromises ISC self-renewal and organoid-forming capacity.** **A**, Schematic of the mouse model including the timeline for tamoxifen (TAM) injections and tissue collection. 1 day after last TAM injection (Day 21<sup>st</sup>), intestinal crypts were isolated from mice and the WT and *Hmgcs2*-KO ISCs were analyzed and sorted using flow cytometry. **B**, Flow plot and **C**, Frequency of 7AAD<sup>-</sup>/EpCAM<sup>+</sup>/CD24<sup>-</sup>/*Lgr5*-GFP<sup>hi</sup> ISCs and *Lgr5*-GFP<sup>low</sup> progenitors in crypt epithelial cells from WT and *Hmgcs2*-KO mice by flow cytometry.  $n > 10$  mice per group. **D**, Representative images and **E**, Quantification of organoid-forming assay for sorted WT and *Hmgcs2*-KO ISCs co-cultured with WT Paneth cells at day 5 and quantification.  $n > 10$  mice per group. For box-and-whisker plot, the data was expressed as 10 to 90 percentiles. For dot plot, the data was expressed as mean  $\pm$  s.e.m. \* $p < 0.05$ , \*\* $p < 0.01$ , \*\*\* $p < 0.005$ , \*\*\*\* $p < 0.001$ . Scale bar is 100  $\mu$ m.

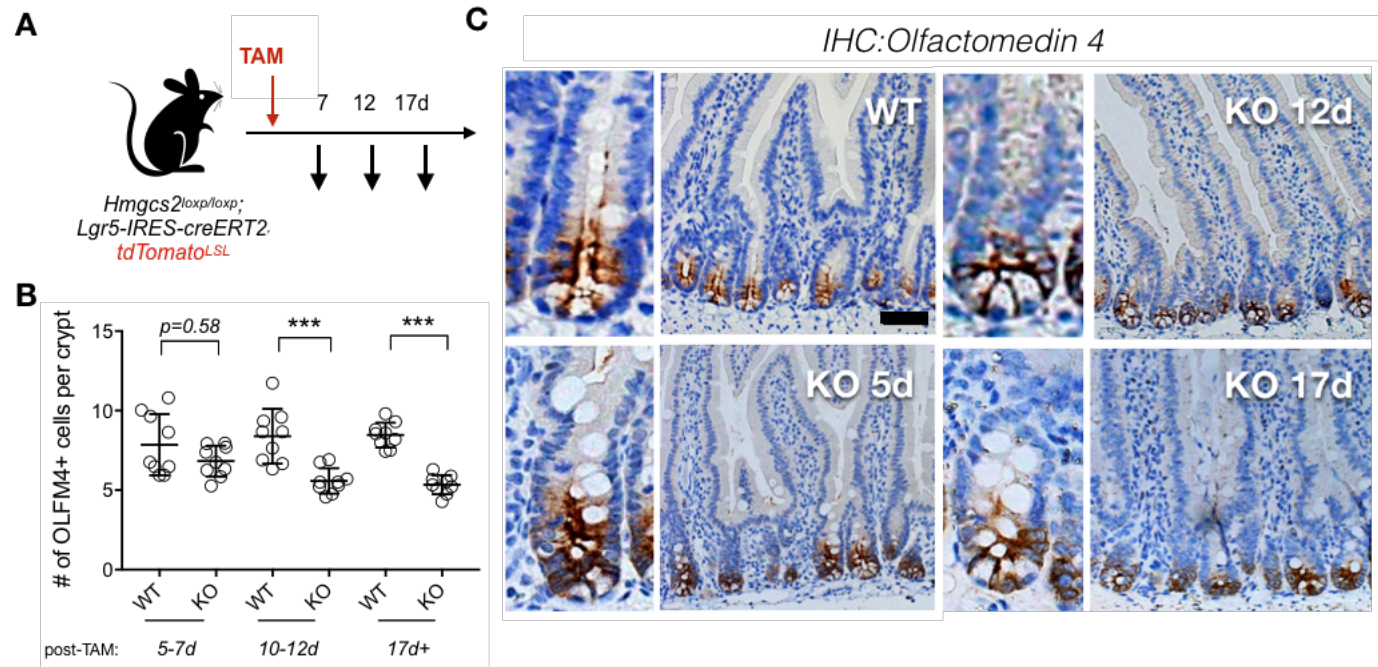


**Figure 3.7 Loss of *Hmgcs2* compromises ISC self-renewal.** **A**, Schematic of the mouse model including the timeline for TAM injection and tissue collection. 7, 12 and 17 days after a single TAM injection, small intestine tissues were collected for histology. **B**, Quantification and **C**, representative images of OLFM4<sup>+</sup> cells in proximal jejunal crypts by IHC.  $n > 25$  crypts per measurement,  $n > 3$  measurements per mouse and  $n > 5$  mice per group. The data was expressed as mean  $\pm$  s.e.m. \* $p < 0.05$ , \*\* $p < 0.01$ , \*\*\* $p < 0.005$ , \*\*\*\* $p < 0.001$ . Scale bar is 100  $\mu$ m.



### 3.4.3 Loss of Hmgcs2 impairs intestinal regeneration after irradiation damage

Proliferative and self-renewing organs are very sensitive to DNA damaging agents such as ionizing radiation and chemotherapy which are widely used in clinics. Skin, hematopoietic system and intestinal epithelium have high self-renewing capacity. Although high doses of radiation (~10-12 Gy in mice) cause complete hematopoietic system failure, the intestinal epithelium can recover from this dose. *Lgr5*<sup>+</sup> ISCs with higher mitotic index drive intestinal maintenance in homeostasis and regeneration in response to injury such as from radiation-induced damage [138]. To compare regenerative capacity of HMGCS2-KO to control group, radiation induced injury model with a tracer mouse to track stem cell driven progeny was used. Briefly, *Hmgcs2*<sup>loxp/loxp</sup>; *Lgr5-IRE5-creERT2*; *Rosa26*<sup>LSL-tdTomato</sup> mice were induced with tamoxifen one day prior to radiation administration to investigate whether HMGCS2 loss affects the regenerative capacity of *Lgr5*<sup>+</sup> ISCs *in vivo* (Figure 3.8A). Intestine tissue was collected after 5 days from irradiation and stained with tdTom. The number of tdTomato<sup>+</sup> clonal progeny was quantified to assess regeneration efficiency of the *Lgr5*<sup>+</sup> ISCs. *Hmgcs2*-null ISCs generated 5-fold fewer labeled tdTomato<sup>+</sup> crypts (Figure 3.8B and 3.8C) compared to controls. These data demonstrate that *Hmgcs2* is critical in *Lgr5*<sup>+</sup> ISC-mediated repair *in vivo* after injury.

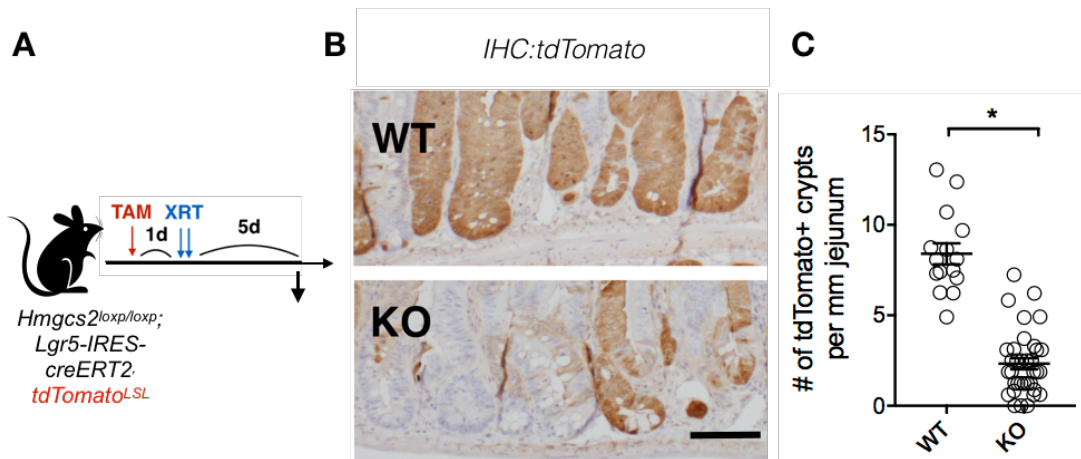


**Figure 3.8 Loss of *Hmgcs2* impairs intestinal regeneration after irradiation damage.** **A**, Schematic of the mouse model including the timeline of TAM injection, irradiation challenge (XRT, two doses of 7.5 Gy with 6 h interval) and tissue collection. **B**, Representative images and **C**, Quantification of tdTomato+ *Lgr5*<sup>+</sup> ISC-derived lineage (cell progeny) by tdTomato IHC. The data was expressed as mean  $\pm$  s.e.m. \* $p < 0.05$ , \*\* $p < 0.01$ , \*\*\* $p < 0.005$ , \*\*\*\* $p < 0.001$ .  $n > 25$  crypts per measurement,  $n > 3$  measurements per mouse and  $n > 5$  mice per group. Scale bar is 100  $\mu$ m.

#### 3.4.4 Loss of *Hmgcs2* skews ISC differentiation towards secretory lineage

In contrast to decrease in the numbers of OLFM4<sup>+</sup> cells post 17 days of tamoxifen induction in intestine of *Hmgcs2*-KO mice (Figure 3.9A), the number of Lysozyme 1 (LYZ1)<sup>+</sup> Paneth cells increased 70% compared to controls (Figure 3.9B). Similarly, the number of Alcian Blue (AB) / periodic acid-Schiff (PAS)<sup>+</sup> goblet cells increased 40% compared to controls (Figure 3.10C). Recently a study showed that differentiation markers such as CDX2, Villin, p21 were significantly decreased by knockdown of HMGCS2 in Caco-2 cells. In addition to that, overexpression of HMGCS2 increased differentiation markers. Although these results do not agree with our results, Caco-2 cells are not stem cells and their differentiation process is spontaneous as indicated in the study [139]. In contrariety, two loss-of-function mouse models (i.e. the LacZ and

loxp models) were utilized to investigate the expression and function of HMGCS2 both *in vitro* and *in vivo*.

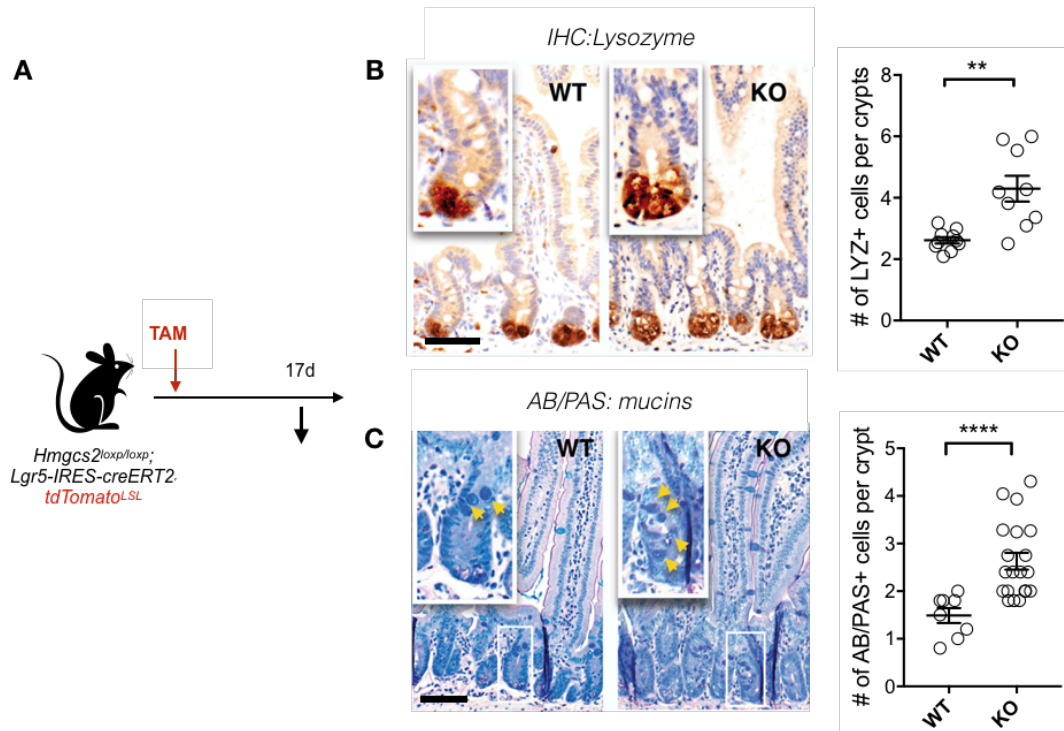


**Figure 3.9 Loss of *Hmgcs2* skews ISC differentiation towards secretory lineage.**

**A**, Schematic of the mouse model, TAM injection and tissue collection time. 17 days after a single TAM injection, small intestine tissues were collected for histology. **B**, Representative LYSOZYME (LYZ) IHC images of proximal jejunal crypts and quantification of numbers of LYSOZYME<sup>+</sup> (LYZ<sup>+</sup>) Paneth cells. **C**, Representative of Alcian Blue (AB) and Periodic Acid Schiff's (PAS) staining images of proximal jejunal crypts and quantification of Mucin<sup>+</sup> goblet cells. n>25 crypts per measurement, n>3 measurements per mouse and n>5 mice per group. The data are expressed as mean +/-s.e.m. \**p*<0.05, \*\**p*<0.01, \*\*\**p*<0.005, \*\*\*\**p*<0.001. AB/PAS stains glycoproteins, mucins, and carbohydrates.

### 3.4.5 Exogenous $\beta$ OHB rescues loss of *Hmgcs2*

After deciphering the critical role of *Hmgcs2*-loss on stemness through observing decrease in the frequencies of *Lgr5*-GFP<sup>hi</sup> ISCs and *Lgr5*-GFP<sup>low</sup> progenitors, organoid

forming capacity in *Hmgcs2*-null ISCs, and regeneration in *Hmgcs2*-KO after irradiation injury and secretory lineage decision through analyses of the frequencies of the Paneth and Goblet cells, we investigated whether providing exogenous  $\beta$ OHB rescues stem cell maintenance and secretory differentiation phenotype both in *Hmgcs2*-null organoids and *Hmgcs2*-KO mice. To address this question, crypts were isolated from control and *Hmgcs2*<sup>loxp/loxp</sup>; *Lgr5*-tdTomato lineage tracer mice after 24 h of tamoxifen administration (Figure 3.11A). Crypts with *Hmgcs2*-null ISCs were then cultured in standard media, with 10  $\mu$ M and 50  $\mu$ M of or without  $\beta$ OHB. Organoids were cultured between 5-7 days and organoid per crypt ratio was analyzed to show organoid forming capacity. Crypts from *Hmgcs2*-KO mice were 34.4% less capable of forming organoids compared to control. In addition to a decrease in organoid forming capacity, *Hmgcs2*-null organoids also showed a 64.3% decline in generation of tdTomato<sup>+</sup> clones per organoid. However, 50  $\mu$ M of exogenous  $\beta$ OHB treatment rescued functional deficiency of *Hmgcs2*-null crypts (Figure 3.10B, Figure 3.10E and F). Lineage bias and effect of exogenous  $\beta$ OHB treatment on goblet cell number were analyzed. After encapsulation of organoids into Histogel, they were embedded into paraffin for sectioning and Alcian blue staining. *Hmgcs2*-null organoids showed a 40.5% increase in goblet cells compared to control and 50  $\mu$ M exogenous  $\beta$ OHB treatment rectified the number of goblet cells (Figure 3.10C and D). These results agree with the *in vivo* results (Figure 3.7 and Figure 3.8) which indicate that *Hmgcs2*-null ISCs *in vitro* are less functional and are biased towards secretory differentiation. A recent study by Wang et al., [139] showed that  $\beta$ OHB treatment with increasing concentration in immortal colon cancer cells (HT29) increases the expression of secretory cell markers, MUC2 and LYZ. However, HT29 cells are an

immortal cell line and the concentrations of  $\beta$ OHB (between 2.5 mM and 10 mM) were very high compared to our dose of 50  $\mu$ M. In addition to cellular energy source, ketone bodies have signaling functions through inhibiting histone deacetylases (HDACs) [140]. Similar to small molecule HDAC inhibitors, the concentration of  $\beta$ OHB might be important for HDAC inhibition [127].

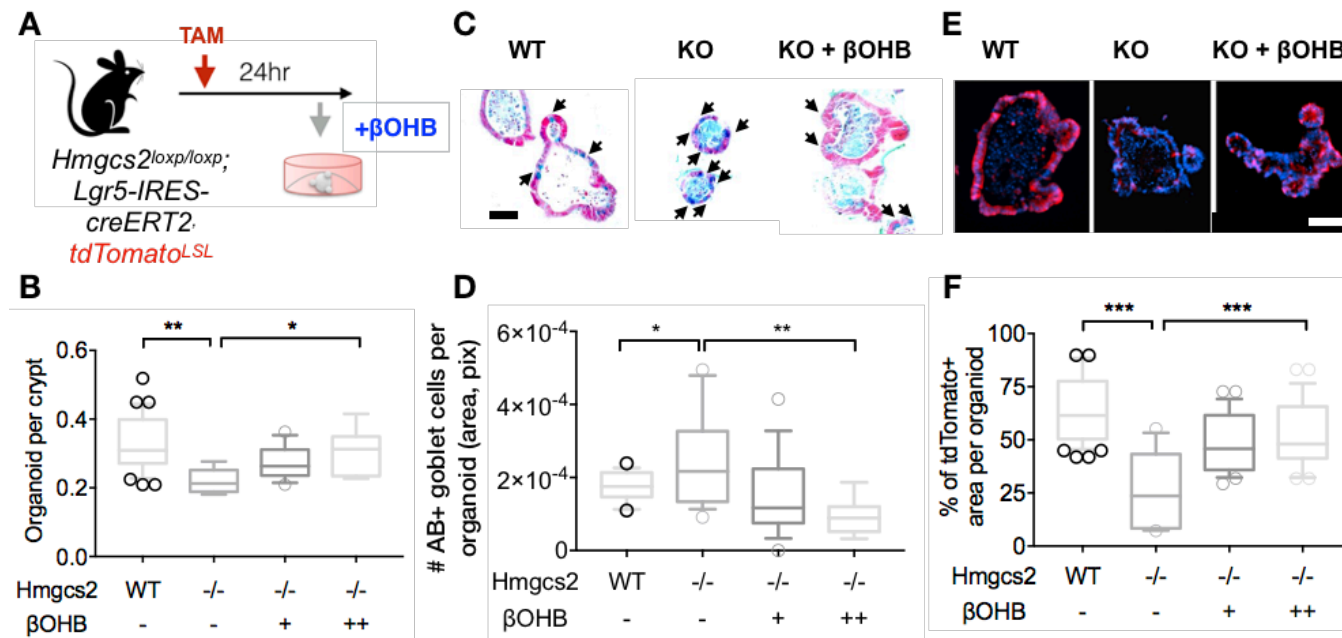


**Figure 3.10 βOHB rectifies *Hmgcs2*-loss in organoids.** **A**, Schematic of the mouse model of *Hmgcs2* loss. After tamoxifen (TAM) injection, intestinal tissues were harvested and intestinal crypts were isolated for organoid-forming assay to assess the effect of βOHB treatment. **B**, Organoid-forming assay and number of organoids per intestinal crypts. **C**, Representative Alcian Blue (AB) images of cultured organoids. **D**, Quantification of Alcian blue<sup>+</sup> goblet cells (black arrows) in organoids. **E**, Fluorescence images of organoids. Red represents tdTomato<sup>+</sup> cells and blue represent nucleus stained with DAPI. **F**, Percentage of tdTomato<sup>+</sup> area per organoid from WT and *Hmgcs2*-KO (*Hmgcs2* <sup>-/-</sup>) ISCs, ± βOHB treatments are +, 10 μM and ++ 50 μM. Representative images were taken from day-5-to-7 organoids. Scale bar is 50 μm. n=5 mice

After observing the rescue effect of exogenous  $\beta$ OHB in *Hmgcs2*-null organoids, we investigated whether  $\beta$ OHB can also compensate the loss of intestinal HMGCS2 activity *in vivo*. For this purpose, radiation challenge experiment was repeated with modified forms of  $\beta$ OHB to deliver gastrointestinal tract of *Hmgcs2*-KO mice (Figure 3.11A). Modified forms of  $\beta$ OHB was used due to two important issues: First issue was technical limitations encountered with fasting or ketogenic diet rescue models in which deletion of *Hmgcs2* was not successful. 24 h fasting and 4-6 weeks ketogenic diet are widely used to increase ketogenesis and blood ketone levels. However, they also elevate expression of *Hmgcs2* which led non-efficient deletion of the gene after tamoxifen injection. Second issue is  $\beta$ OHB is water soluble and is easily absorbed by the gastrointestinal tract and elevate blood ketone levels. Ketone esters or salts are widely used to model a ketogenic diet or fasting and elevates  $\beta$ OHB levels *in vivo* in one week [141]. However, the serum  $\beta$ OHB levels increase rapidly and cause renal elimination, which make them non-ideal fasting or ketogenic diet mimicking models for gastrointestinal tract. For the rectifying effect, a more stable form of  $\beta$ OHB is required to increase the retention time and have slow-release properties in intestine. Poly(lactide-co-glycolide) (PLGA) is widely used in FDA-approved drug products to reduce dosing frequency and potential drug toxicity [142]. Encapsulation of different compounds in PLGA polymer nanoparticles and their successful delivery into gastrointestinal system was shown [48]. Poly- $\beta$ -hydroxybutyrate (PHB) is a linear polymer of  $\beta$ OHB with three types, and its different functions were first discovered in prokaryotes. However, recent studies showed the presence of PHB in mammalian cells and their important physiological roles with proteins and inorganic polyphosphate. PHB is an ideal candidate of oral delivery of  $\beta$ OHB into gut as a result of its

insolubility in water and easy degradation to monomers by esterase [131]. Previously, dietary PHB altered the composition and diversity of gut microbiota in *Litopenaeus vannamei*. Dietary PHB increased the abundance of beneficial bacteria such as *Bacillus*, *Lactobacillus* and activate mTOR pathway [143]. Therefore, two modified forms of  $\beta$ OHB, PLGA encapsulated and oligomer were used to investigate the compensatory effect of exogenous  $\beta$ OHB on intestinal regeneration of *Hmgcs2*-KO mice challenged with irradiation. Oral administration of  $\beta$ OHB encapsulated poly(lactic-co-glycolic acid) (PLGA) nanoparticles or  $\beta$ OHB oligomers partially restored intestinal regeneration after irradiation-induced damage, which otherwise was severely impaired in *Hmgcs2*-KO mice (Figure 3.11B and C). Serum  $\beta$ OHB levels in irradiated mice was not measured due to critical body conditions of the mice which might barely stand invasive approaches after irradiation. Youm et al., utilized from both ketone diesters and engineered nanomaterials complex of  $\beta$ OHB to elevate the blood levels in mice via oral and intraperitoneal injection routes. Nano-lipogels helped to reduce the clearance of  $\beta$ OHB and increase its retention time and bioavailability in body without toxicity [141].



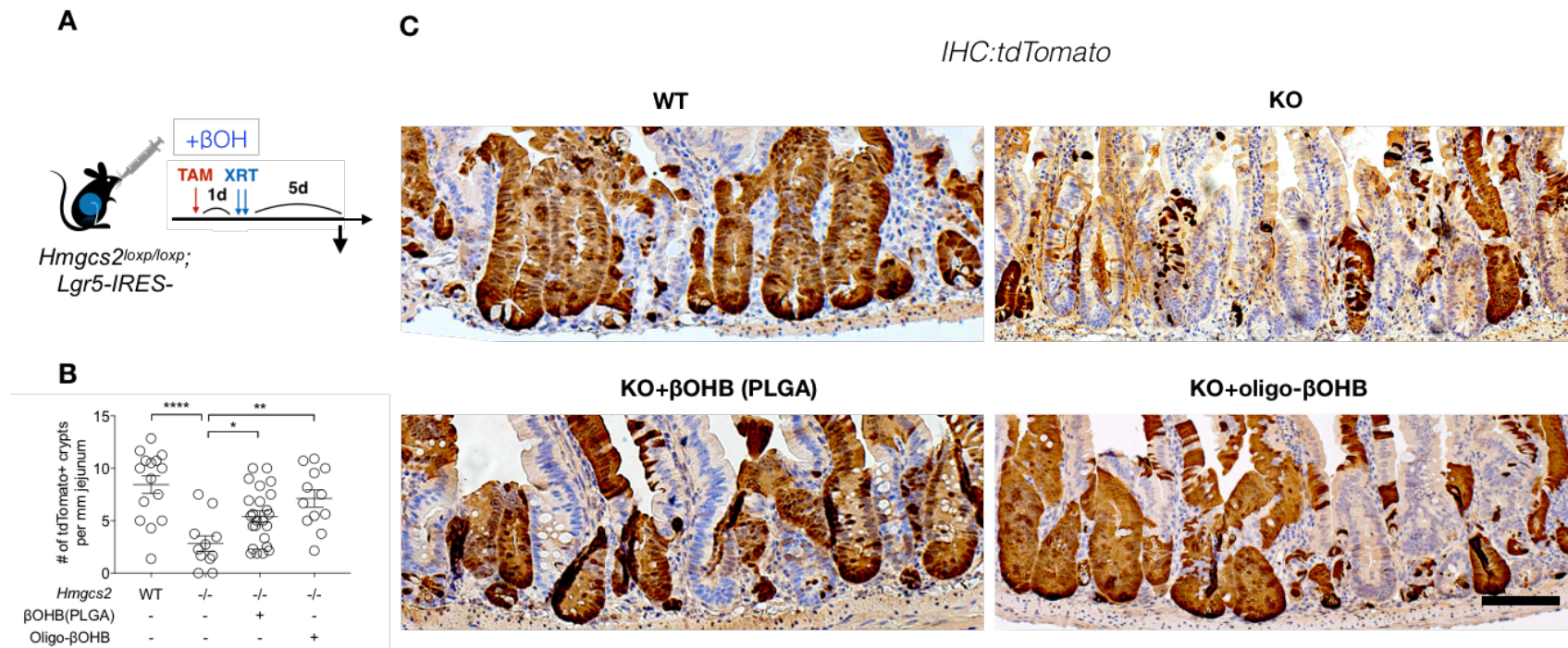


**Figure 3.11 Oral administration of  $\beta$ OHB improved the regeneration capacity of *Hmgcs2*-KO mice intestine after irradiation challenge.** **A**, Schematic of the mouse model including the timeline of tamoxifen (TAM) injection, oral administration of nanoparticle  $\beta$ OHB encapsulated PLGA or  $\beta$ OHB oligomers, irradiation (XRT, two doses of 7.5 Gy with 6 h interval) and tissue collection. **B**, Quantification and **C**, representative images of tdTomato<sup>+</sup> *Lgr5*<sup>+</sup> ISC-derived lineage (cell progenies) by IHC.  $n > 25$  crypts per measurement,  $n > 5$  measurements per mouse and  $n > 3$  mice per group. The data was expressed as mean  $\pm$  s.e.m. \* $p < 0.05$ , \*\* $p < 0.01$ , \*\*\* $p < 0.005$ , \*\*\*\* $p < 0.001$ . Scale bar is 100  $\mu$ m.

### 3.5 Conclusions

Intestinal tissue is the most rapidly self-renewing tissue driven by crypt base residing stem cells. Understanding the biology of intestinal epithelium and regulatory mechanisms may provide a therapeutic benefit for the pathophysiological conditions in intestine. A large number of recent studies uncovered signaling pathways which control stem cells. Wnt and Notch are principal controller of stem cell maintenance and differentiation of the intestinal epithelium. Although the principal signaling pathways are well defined, the role of the metabolism on intestinal epithelium homeostasis is not clear yet. Here in this study, enrichment and co-expression of a metabolic gene 3-Hydroxy-3-Methylglutaryl-CoA Synthase 2 (*Hmgcs2*) were observed *Lgr5*<sup>+</sup> intestinal stem cells (ISCs). HMGCS2 is a rate-limiting enzyme in ketogenesis and controls the synthesis of ketone bodies such as  $\beta$ OHB and acetoacetate (AcAc). A robust genetically engineered mouse model with knockout-first technology was generated to interrogate the function of this metabolic gene in ISCs and intestinal epithelium. HMGCS2<sup>+</sup> cells have capacity to form organoids and the number of both ISCs and the progenitors decreased upon loss of *Hmgcs2*. A decrease in the number of OLFM4<sup>+</sup> cells, another stem cell marker, *in vivo* was observed. In addition, *Hmgcs2*-null ISCs showed less capacity to form organoids and less regenerative capacity after irradiation challenge. Whereas the number of secretory cell types are increased in organoids (Alcian blue<sup>+</sup> goblet cells) and intestine (LYZ<sup>+</sup> Paneth cells and Mucin<sup>+</sup> goblet cells). Compromise of ISC function is rectified by exogenous  $\beta$ OHB in organoids and engineered  $\beta$ OHB forms, PLGA-encapsulated and oligomer, *in vivo*. It was recently shown that ketone bodies act as endogenous histone deacetylase (HDAC)

inhibitors in addition to their role as an energy source in specific physiological states. HDACs are epigenetic regulators of gene expression and are known to regulate intestinal epithelial differentiation through Notch signaling. This thesis is the first study showing the epigenetic role HMGCS2 on ISC self-renewal and differentiation. Further efforts should be directed towards a mechanistic understanding of HMGCS2- $\beta$ OHB-HDAC target genes in different physiological states of intestine. Understanding metabolic regulation of genes through epigenetic mechanism might offer a promise about improvement of human health and therapeutic approaches.

# CHAPTER 4

## 4 Self-assembling peptides for remineralization of enamel

### 4.1 The objective

Human enamel is a highly mineralized tissue with unique morphological structures and mechanical properties compared to other mineralized tissues such as bone and dentin. Enamel formation (amelogenesis) occurs during early stages of development through accumulation of highly organized crystalline minerals. At the end of amelogenesis, mineralized enamel is mature and has highly organized three-dimensional micro- and nano-structures of hydroxyapatite (HA) which determine the enamel hardness. Healthy oral environment has a key role in enamel protection through balancing mineral dissolution and deposition. However, enamel becomes susceptible to caries due to bacterial metabolism or acidic foods in the oral cavity. Damaged enamel is scarcely self-repaired. Therefore, artificial strategies have been developed to repair the defects and cavities in enamel before it moves to the dentin and pulp region of the tooth. Instead of artificially synthesized apatite, unstructured non-apatite substitutes such as amalgams, metal alloys, and ceramics are widely used to refill enamel decays due to better bonding and strong mechanical strength of non-apatite substitutes. Scientists develop new biomimetic alternatives of enamel-like apatite for enamel repair. In this study, I developed self-assembling peptides to enhance mineralization of demineralized enamel surface under physiological conditions and tested their biocompatibility on human gingival fibroblasts.

## 4.2 Introduction

Teeth are the most distinctive organs in the evolution of mammals with similar developmental stages to humans. The human tooth is the mastication organ in body with specialized structures. These structures may be classified into three groups as (i) dentin and enamel which are the characteristic structures of tooth and are not found in any other part of the body, (ii) the pulp initiates formation of tooth and contains nerves, blood vessels, and immune cells, (iii) supporting structures of the tooth such as the alveolar bone, gingiva, and cementum. The tooth development is a complex process and starts in very early stages of the embryonic development (~6-8 weeks) with iterative use of evolutionarily conserved molecular pathways such as transforming growth factor  $\beta$  (TGF $\beta$ ), fibroblast growth factor (FGF), sonic hedgehog (Shh) and Wnt signaling [144]. During development, tooth development starts with formation of dentin layer and is followed by enamel formation. Enamel formation (amelogenesis) occurs in two stages: Secretory stage and maturation stage. In the secretory stages, ameloblasts secrete enamel proteins to form an organic matrix which is then partially mineralized by the enzyme alkaline phosphatase. In the maturation stage, ameloblasts change their functions from secretion to transportation of substances which play an important role in the formation of the enamel. At the end of this stage, the mature enamel is composed of 95-97% hydroxyapatite (HA) by weight and less than 1-2% organic materials after degradation of most enamel proteins. In addition, ameloblasts are degraded and tooth is ready for eruption into the oral cavity. Mature enamel is the hardest mineralized tissue in our body with unique robust mechanical properties [145, 146]. Unlike rodent incisors, teeth do not grow continuously in most of the mammals including humans due to the lack of stem cell-like cells. Consequently, acellular

enamel cannot regenerate itself after injuries and decays, which results in total tooth loss if protective treatments are not applied. Currently, the effective treatment for dental caries is to fill the decayed tissue with unstructured non-apatite substitutes such as amalgams, metal alloys, or ceramics etc. However, promoting remineralization in small lesions is preferred to decrease mineral dissolution before tooth decay increases. Therefore, enamel remineralization is an attractive target of biomimetic and bioinspired therapeutic approaches. Enamel proteins are one of the main sources of the inspiration to mimic protein-mineral interaction and develop novel engineered nanomaterials. Many proteins associated with mineralized tissues in bone, dentin, and enamel contain acidic moieties such as glutamic acid, aspartic acid, and serine. Engineered nanomaterials mimic acidic residues of proteins to enhance remineralization on the enamel surface [55]. Recent studies developed a large variety of engineered nanomaterials for enamel regeneration including amorphous calcium phosphate, casein phosphopeptide- amorphous calcium phosphate nanocomplexes [147], apatite nanoparticles [65], peptides [62, 64], hydroxyapatite-dendrimer complex [148], and amelogenin-chitosan hydrogels [149]. Some of these engineered nanomaterials (peptide P<sub>11-4</sub>) are approved and are commercially available for clinical use in the treatment of early small enamel lesions under brand name Curodont Repair (Credentis AG, Windisch, Switzerland) [62]. As a supramolecular platform, self-assembling peptides are gaining more attention due to easy incorporation of bioactive epitopes and chemical moieties that can to initiate the mineralization process. In this study, I designed self-assembling peptides mimicking acidic residues of amelogenin to direct hydroxyapatite formation on eroded enamel when incubated with simulated body fluid (ionic substitute of human plasma) as depicted in Figure 4.1.

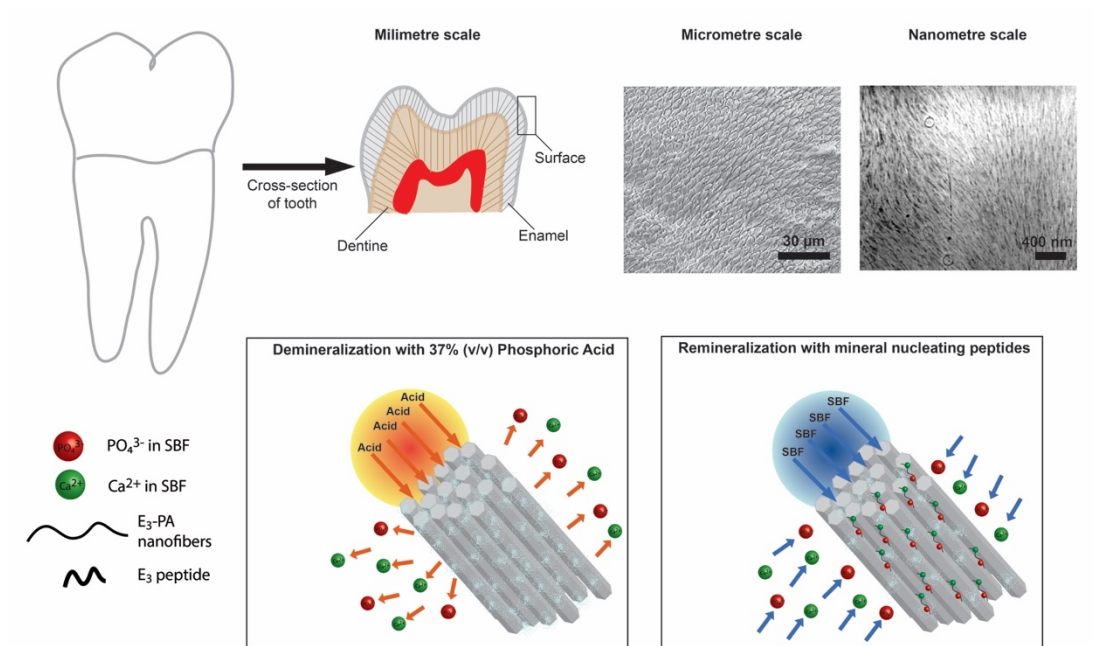


**Figure 4.1 Schematic of experimental demineralization and remineralization on tooth enamel.**

Carboxylate groups of glutamic acid attract  $\text{Ca}^{2+}$  and  $\text{PO}_4^{3-}$  ions onto existing crystalline hydroxyapatites and induce oriented aggregation of newly formed hydroxyapatite. Here, two different forms of self-assembling peptide with (C12-VVAGEEEE-NH<sub>2</sub>) or without alkyl tail (VVAGEEEE-NH<sub>2</sub>) were used. Covalently attached alkyl tails in amphiphilic peptides increase packing of hydrophobic amino acids in aqueous environment and enhance mechanical characteristic of peptide nanofibers. Therefore, the effect of mechanical characteristic and length of peptides on mineral deposition and biocompatibility were compared. The biocompatibility of soluble self-assembling peptides was also investigated by using, human gingival fibroblasts in the oral cavity, to show a potential safe clinical use of mineralizing peptides in enamel restoration agents.

### 4.3 Experimental Methods

#### 4.3.1 Chemical and Reagents

All 9-fluorenylmethoxycarbonyl (Fmoc) and tert-butoxycarbonyl (Boc) protected amino acids, lauric acid, [4-[ $\alpha$ -(20,40-dimethoxyphenyl) Fmoc-aminomethyl] phenoxy] acetamidonorleucyl-MBHA resin (Rink amide MBHA resin) and 2-(1H-benzotriazol-1-yl)-1,1,3,3-tetramethyluronium hexafluorophosphate (HBTU) and diisopropylethylamine (DIEA) were purchased from NovaBiochem, Merck and ABCR. All other chemicals for peptide amphiphile synthesis were analytical grade and were purchased from Fisher, Merck, Alfa Aesar, or Sigma Aldrich. 3-(4,5-dimethylazol-2-yl)-2,5-diphenyl-tetrazolium bromide (MTT) kit, and hydrochloric acid fuming 37% were purchased from Sigma-Aldrich Chemical Co. All cell culture materials and ethidium homodimer, and calcein Am were also purchased from Gibco, Invitrogen. BrdU Kit was purchased from Roche. Cellulose ester dialysis membranes were purchased Spectrum™ Spectra/Por™. Ultrapure water (18.2 M $\Omega$ ) was obtained from a Sartorius arium® Lab Water System.

#### 4.3.2 Synthesis and Purification of Peptides

Lauryl-VVAGEEEE-NH<sub>2</sub> (E3-PA) and VVAGEEEE-NH<sub>2</sub> (E3-Peptide) peptide molecules were synthesized using solid phase peptide synthesis method on Rink amide MBHA resin at 0.5 mmol scale. Initially, resin was swelled with 30 min dichloromethane (DCM) shaking for coupling. DCM and dimethylformamide (DMF) were used for washing steps. Activation of 2 mole equivalents (equiv.) of amino acids



was achieved by 1.95 mole equiv. of N,N,N',N'-tetramethyl-O-(1H-benzotriazole-1-yl) uranium hexafluorophosphate (HBTU), and 3 mole equiv. of diisopropylethylamine (DIEA) for 1 mole equiv. of rink amide resin in 10 mL dimethylformamide (DMF). Each amino acid coupling was restricted to 4 h and acetylation of unreacted amine groups after each coupling step was done by 10% acetic anhydride–DMF solution. Fmoc-protecting group was removed with 20% piperidine/DMF solution for 20 min. Coupling of lauric acid was performed similarly to amino acid coupling except that coupling time was overnight. Acetylation was performed with 10% acetic anhydride–DMF solution after cleavage of the Fmoc group from the final valine residue of E3-Peptide. Peptide cleavage from the resin and deprotection were carried out with 95% cleavage cocktail (95:2.5:2.5 trifluoroacetic acid (TFA):triisopropylsilane (TIS):water) for 2 h at room temperature. Excess TFA was removed by rotary evaporation. Ice-cold diethyl ether for E3-PA, and ice-cold diethyl ether with 10 % citric acid for E3-Peptide solutions were used to precipitate the remaining peptide solutions overnight at  $-20\text{ }^{\circ}\text{C}$ . White precipitates were collected with centrifugation at 6000 rpm 20 min  $4\text{ }^{\circ}\text{C}$ . The excess diethyl ether was removed by drying under fume hood and peptides were dissolved in ultrapure water with sonication. Solution was frozen at  $-80\text{ }^{\circ}\text{C}$  and then lyophilized for 3 days. The lyophilized product was characterized by Agilent 6530 quadrupole time of flight (Q-TOF) mass spectrometry with electrospray ionization (ESI) source equipped with reverse-phase analytical high-performance liquid chromatography (HPLC) with Zorbax Extend-C18  $2.1 \times 50\text{ mm}$  column for basic conditions and Zorbax SB-C8  $4.6 \times 100\text{ mm}$  column for acidic conditions. In order to purify the peptide amphiphile molecules and remove the residual TFA, a preparative HPLC system (Agilent 1200

series) was used with a mobile phase of a gradient of 0.1% ammonium hydroxide/water and 0.1% ammonium hydroxide/acetonitrile. Residual TFA was removed from the peptides with a subsequent dialysis procedure using cellulose ester dialysis membrane with a molecular-weight-cut-off of 100–500 Da. After purification, peptide amphiphiles were lyophilized and stored at  $-20\text{ }^{\circ}\text{C}$  until further use.

### **4.3.3 Transmission Electron Microscopy**

1 mM E3-PA and E3-Peptide solutions were prepared with ultrapure water at pH 7 using 1 mM NaOH or 1 mM HCl. Then peptides solutions were diluted to 100  $\mu\text{M}$  for TEM sample preparation. One drop from 100  $\mu\text{M}$  of E3-PA and E3-Peptide was laid on a 200-mesh carbon TEM grid for 2 min followed by 2 wt% uranyl acetate staining for 40 s. Later, TEM grids were washed with ultrapure water (3 times for 2 min) to remove excess uranyl acetate and dried under flow hood. TEM and STEM (HAADF mode) images were acquired at 300 kV with FEI Tecnai G2 F30 TEM.

### **4.3.4 Circular Dichroism**

CD (JASCO J815 CD spectra polarimetry) was used to analyze the secondary structures of peptide molecules. 1 mM E3-PA and E3-Peptide solutions were prepared with ultrapure water at pH 7 using 1 mM NaOH or 1 mM HCl. Then peptide solutions were diluted to  $1 \times 10^{-4}\text{ M}$  for CD measurement. Scanning was done between 190 nm to 300 nm using a digital integration time of 1 s, a band width of 1 nm and with standard sensitivity. Molar ellipticity was calculated with the data obtained from the measurements.

#### 4.3.5 Enamel Remineralization Assay

Preparation of the teeth: Molar and incisor teeth were extracted from a sheep skull. Extracted teeth were cleaned with 10% bleach and rinsed thoroughly with distilled water and dried in an oven. After drying it was stored at 4 °C. For demineralization and remineralization experiments, each tooth was used after dividing into small pieces. Enamel surfaces were demineralized with 34% phosphoric acid for 15 - 60 s (optimized) and then rinsed thoroughly with distilled water several times. Demineralized teeth were stored in distilled water at 4 °C.

Preparation of the simulated body fluid (SBF): Simulated biological fluids are often used for *in vitro* assessment of the biotherapeutics. There are various simulated biological fluids that can mimic different biological fluids such as simulated body fluid (mimics human plasma), artificial saliva (mimics oral cavity), simulated ophthalmic tears, and simulated gastric fluids. Simulated body fluid is more widely used for dental implants and *in vitro* biomineralization experiments compared to artificial saliva. Therefore, in this study simulated body, fluid was used which has ion concentrations nearly equal to those of human blood plasma prepared according to Table 4.1 developed by in 1990 by Kokubo et al. [150]. Briefly, all bottles and beakers should be glass-ware and carefully cleaned in the following order: washed with (i) a neutral detergent, (ii) 1N HCl solution overnight, (iii) pure ethanol overnight, (iv) distilled water overnight, and (v) then dried in oven. 500 mL of ion-exchanged and distilled water was poured into the cleaned glass beaker and placed on a magnetic-stirrer with heating option and heated to 36.5 °C, and the reagents were dissolved one by one in the order as given in Table 4.1. The pH of the solution was carefully adjusted by tris(hydroxymethyl)aminomethane (Trizma<sup>®</sup> base) and 1 M HCl carefully. The total

volume was adjusted to 1 L and cooled down to room temperature. SBF was transferred to a polystyrene bottle and stored at 4 °C. (This solution should be used in one month. If some substance precipitates in the solution during preparation or storage, do not use this solution in experiments and bottle as container again).

**Table 4. 1 Reagents for preparation of 1X simulated body fluid (pH 7.40 , 1L)**

Order	Reagent	Amount
1	NaCl	7.996 g
2	NaHCO <sub>3</sub>	0.350 g
3	KCl	0.224 g
4	K <sub>2</sub> HPO <sub>4</sub> · 3H <sub>2</sub> O	0.228 g
5	MgCl <sub>2</sub> · 6H <sub>2</sub> O	0.305 g
6	1 M HCl	40 mL (Add about 90 % of HCl)
7	CaCl <sub>2</sub>	0.278 g
8	Na <sub>2</sub> SO <sub>4</sub>	0.071 g
9	(CH <sub>2</sub> OH) <sub>3</sub> CNH <sub>2</sub>	6.057 g

*Remineralization assay:* Demineralized tooth pieces were immersed into 100 μM E3-PA or E3-Peptide containing 1X SBF solution and the remineralization process was observed under scanning electron microscope (SEM) operating at low voltage (2-5 kV) and without coating every 30 min.

#### 4.3.6 *In vitro* Cell Viability and Proliferation

Human gingival fibroblasts (HGFs) were obtained from the laboratory of Prof. Dr. Sema Hakkı (Selçuk University, Faculty of Dentistry, Department Clinal Sciences, Program of Periodontics). HGFs were maintained in a humidified 37 °C, 5% CO<sub>2</sub> incubator using 75 cm<sup>2</sup> polystyrene cell culture flasks containing High Glucose Dulbecco's modified Eagle's medium (DMEM) supplemented with 10% fetal bovine serum (FBS, Gibco), 1% penicillin/streptomycin (P/S) and 2 mM L-glutamine. Mycoplasma test was done before the experiments with MycoAlert™ Mycoplasma Detection Kit (Lonza Bioscience). Passaging of cells was carried out at cell confluency between 50 to 70% using trypsin/EDTA.

HGFs were seeded at a density of  $5 \times 10^3$  cells/well in a 96-well plate and incubated for 4 h for attachment. Then, HGFs were treated with increasing concentrations of E3-PA and E3-Peptide diluted in cell culture media. After incubation, cellular response was assessed with two different methods: Live-dead assay was utilized for the assessment of viability and MTT assay (also known as Resazurin assay) for the analyzing the metabolic activity was used.

Live-dead assay: After 48 h, the plate was centrifuged for 5 min at 2500 rpm to keep dead cells on the surface. Then, each well was washed with 1× PBS for three times and 2 min centrifugation was done at each step. 2 μM calcein AM and 4 μM ethidium homodimer reagents were prepared in PBS and 100 μL of these solutions was added to each well. After subsequent 40 min incubation, cells were observed under a fluorescent microscope. The experiment was carried out with n = 3 and, representative images were taken per treatment group.

MTT assay: After 24 h, the medium was removed and the cells were treated with 200  $\mu$ L of 10% 3-(4,5-dimethylthiazol-2-yl)-2,5-diphenyltetrazolium bromide (MTT) in phenol-red free DMEM. After observing formazan crystal (~4 h), medium was removed and formazan crystals were dissolved with DMSO. The optical density of the dissolved formazan crystals (purple color) was quantified at 590 nm as indicative of metabolic activity.

Proliferation assay: The proliferation of cells treated with 100  $\mu$ M E3-PA and E3-Peptide was assessed using BrdU assay (Roche). Cells were seeded to tissue culture plates (TCP) at a density of  $5 \times 10^3$  cells/well. Cells were incubated in standard cell culture medium supplemented with 100  $\mu$ M BrdU labeling solution for 24 h. At the end of the incubation, BrdU incorporation assay was performed according to the manufacturer's instructions. Briefly, cells were fixed with FixDenat for 30 min and anti BrdU-POD solution was added into the wells. Following 90 min incubation and tapping, substrate solution was added into the wells and the proliferation rates of the cells were quantified by measuring the absorbance (370 nm, with 492 nm reference wavelength) with a microplate reader.

## **4.4 Results and Discussions**

### **4.4.1 Design and characterization of the mineralizing peptides**

The lauryl-VVAGEEEE-Am (E3-PA) and VVAGEEEE-Am (E3-Peptide) were designed according to the sequence of amelogenin protein which has 15-20% glutamic acid residues in its amino acid sequence and an important role in enamel formation [151]. In addition to that, previously, the mineral deposition effect of lauryl-VVAGEEEE-Am sequence was shown with human mesenchymal stem cells on titanium coated surfaces

by Ceylan. et al. [152]. Glu-Glu-Glu (EEE) sequence was synthesized in two forms with solid phase peptide sequence on rink amide resin. Both in E3-PA and E3-Peptide have the  $\beta$ -sheet forming VVAG motif to facilitate intermolecular hydrogen bonding in nanofiber structure, while the EEE sequence will help the deposition of hydroxyapatite onto the enamel surface and increase solubility of the peptide in aqueous environment. In contrast, E3-PA has a hydrophobic lauryl tail that promotes better self-assembly in conjunction with the  $\beta$ -sheet forming VVAG motif and enhance the mechanical stability of nanofibers (Figure 4.2a and 4.2b). After purification of the peptide products, the purity was assessed using Agilent 6530 quadrupole time of flight (Q-TOF) mass spectrometry with electrospray ionization (ESI) source equipped with a reverse-phase analytical HPLC. Due to the lack of an alkyl tail, lauric acid, the retention time was very quick in E3-Peptide (Figure 4.2).

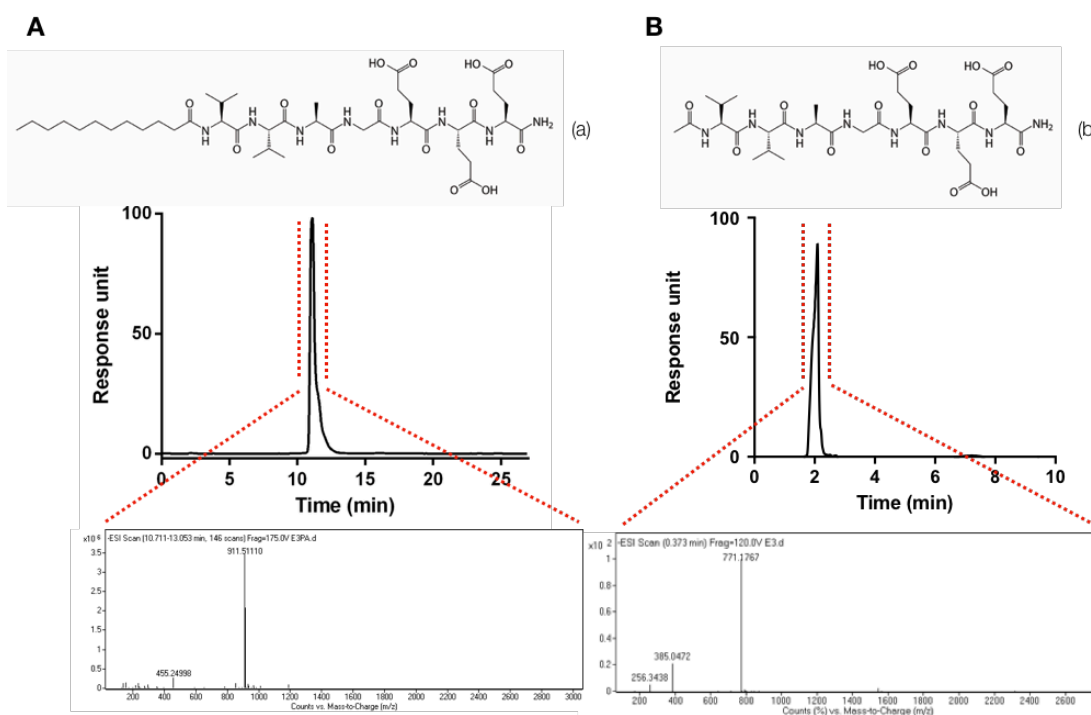


**Figure 4.2 Chemical structures, liquid chromatography and mass spectroscopy results of peptides. (A) Chemical structure, liquid chromatography and mass spectroscopy of C12-VVAGEEEE-NH<sub>2</sub> (E3-PA). For E3-PA [M-H]<sup>-</sup> (calculated) =**

912.52,  $[M-H]^-$  (observed) = 911.51,  $[M/2-H]^-$  (calculated) = 455.26,  $[M/2-H]^-$  (observed) = 455.24, **(B)** Chemical structure, liquid chromatography and mass spectroscopy of VVAGEEE-NH<sub>2</sub> (E3-Peptide). For E3-Peptide  $[M-H]^-$  (calculated) = 772.36,  $[M-H]^-$  (observed) = 771.17,  $[M/2-H]^-$  (calculated) = 385.18,  $[M/2-H]^-$  (observed) = 385.04,  $[M/3-H]^-$  (calculated) = 256.45,  $[M/3-H]^-$  (observed) = 256.34. The purities of the crude products were analyzed according to the optical density at 220 nm after subtracting mass spectrum of water sample.

Morphological analysis of the self-assembly was shown by TEM imaging. Although both E3-PA and E3-Peptide have three glutamic acid residues which is a strong  $\beta$ -sheet blocker, both E3-PA and E3-Peptide demonstrated  $\beta$ -sheet driven nanostructures in TEM images (Figure 4.3A and Figure 4.3B). TEM showed that E3-PA nanofibers were typically 8-12 nm in diameter and several microns in length (Figure 4.3B). However, due to lack of an alkyl tail, lauric acid, E3-Peptide formed a twisted nanoribbon-like structures as result of increased hydrogen bonding distance between two peptide molecules in nanoribbon (Figure 4.3A) [153, 154]. Similar to E3-PA nanofibers, E3-peptide nanoribbons were several microns length. Moreover, cryo-TEM preserves the morphology of the nanostructures in aqueous solution compared to conventional TEM sample preparation which creates drying effects. Therefore, the actual morphological structure of E3-Peptide can be observed with cryo-TEM. Circular dichroism results confirmed  $\beta$ -sheet formation in E3-PA with a positive signal around  $\sim 200$  nm and negative signal around  $\sim 220$  nm. In contrast to TEM images, E3-Peptide did not show  $\beta$ -sheet signal in circular dichroism and had a random coil signal which might arose from disordered  $\beta$ -sheets due to lack of alkyl tail [153] (Figure 4.3C).  $1 \times 10^{-4}$  M E3-PA and E3-Peptide concentration was chosen to show the actual secondary structure of the self-assembling peptide molecules when they are used in remineralization assay. Previously, the critical aggregation concentration (CAC) of peptide amphiphiles was



shown to be below 100  $\mu\text{M}$  ( $\sim 5 \mu\text{M}$ ) [155]. Therefore, observing  $\beta$ -sheet signal at  $1 \times 10^{-4}$  M concentration for E3-PA was expected. However, lack of alkyl tail might result in high CAC and delay the formation of secondary structures in E3-Peptide at  $1 \times 10^{-4}$  M.

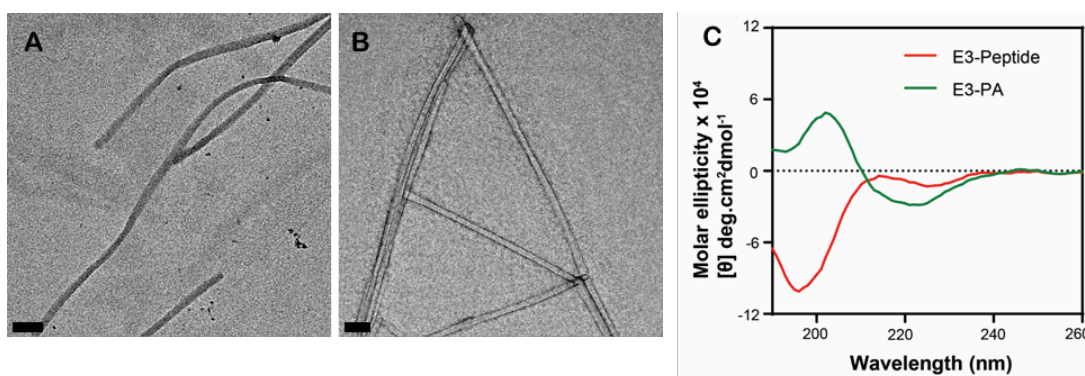


**Figure 4.3 Characterization of the self-assembling peptides and the mechanism of self-assembly.** TEM image of individual peptide molecules of (A) VVAGEEE-Am (E3-Peptide), (Scale bar, 100 nm), (B) Lauryl-VVAGEEE-Am (E3-PA), (Scale bar, 50 nm) (C) Secondary structure characterization of E3-PA and E3-Peptide with circular dichroism. pH of peptides was  $\sim 7$  after dissolving in water and concentrations of peptide molecules were 100  $\mu\text{M}$ .

#### 4.4.2 Enamel regeneration with self-assembling peptides

Tooth samples were demineralized as described in the methods section (see section 4.3.5) and remineralization assay was performed as depicted in Figure 4.1. After demineralization, enamel surfaces were immersed in 1X SBF (prepared according to protocol of [150]) containing either 100  $\mu\text{M}$  E3-PA or E3-Peptide at 37  $^{\circ}\text{C}$  for different time points (pH 7.4) to promote the nucleation and growth of the hydroxyapatite crystals. After immersion, nucleation and mineral deposition was observed by SEM (Figure 4.4). During the first 30 min and 60 min of immersion, the rods of enamel prism were still visible in both E3-PA and E3-Peptide treated groups. After 60 min, mineral deposition onto enamel prisms was observed in both groups. In contrast to E3-

PA, E3-Peptide treated enamel surfaces deposited more minerals. However, as seen in 120 min immersion samples, newly formed mineral layers started to peel off from enamel surfaces which is sign of weak interaction of newly formed hydroxyapatite crystals. Peeling effect of newly formed mineral layer was also observed in enamel surfaces treated with acidic peptide (DSS) [60]. This problem can be solved by adding additional nanomaterials such as apatite nanoparticles which help the crystal orientation of the newly formed hydroxyapatite and decrease scar-like tissue between repaired layer and pre-existed apatite rod with the help of glutamic acid in the immersion liquid [65]. On the other hand, these self-assembling peptides have shown quite rapid mineralization compared to other mineralizing agents.

#### **4.4.3 Biocompatibility of the mineralizing peptide**

Human gingival fibroblast cells were cultured in serially-diluted concentrations of E3-PA and E3-Peptide. After 24 h of the incubation, the metabolic activity of the cells which is an indirect sign of toxicity was assessed with MTT assay. Higher concentrations of E3-PA (above 128  $\mu$ M) resulted in significant decrease in the cell viability. Interestingly, high dose of E3-peptide did not show a decrease in viability of HGFs (Figure 4.5).

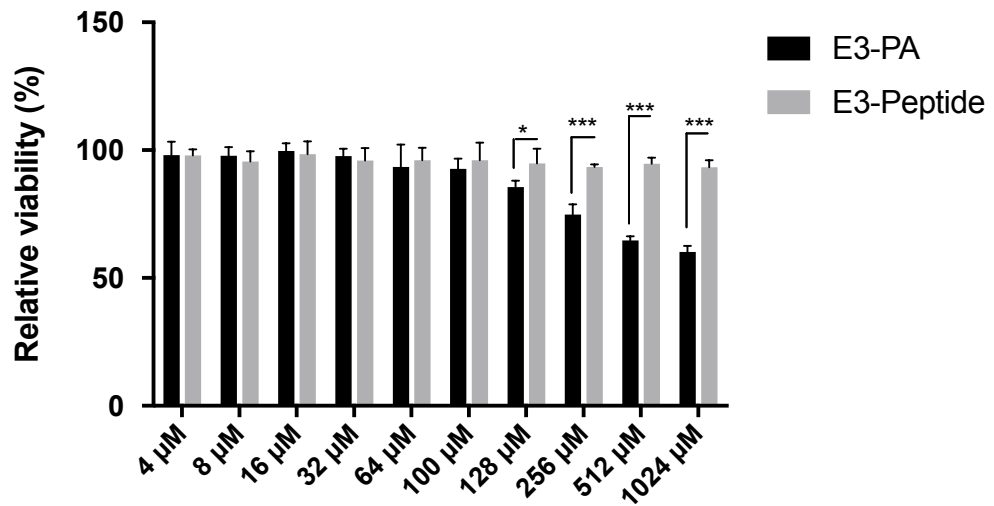


**Figure 4.5 Dose-dependent cytotoxicity in HGFs after 24 h.** HGFs were exposed to E3-PA and E3-Peptide 10% FBS DMEM and the metabolic activity was assessed with MTT assay. Error bars show s.e.m, two independent experiments were repeated with n=4 in each experiment. Two-way ANOVA with Sidak's Multiple Comparison Test was used to show statistical significance at \*\*\* p<0.001.

*E3-PA*

*E3-Peptide*

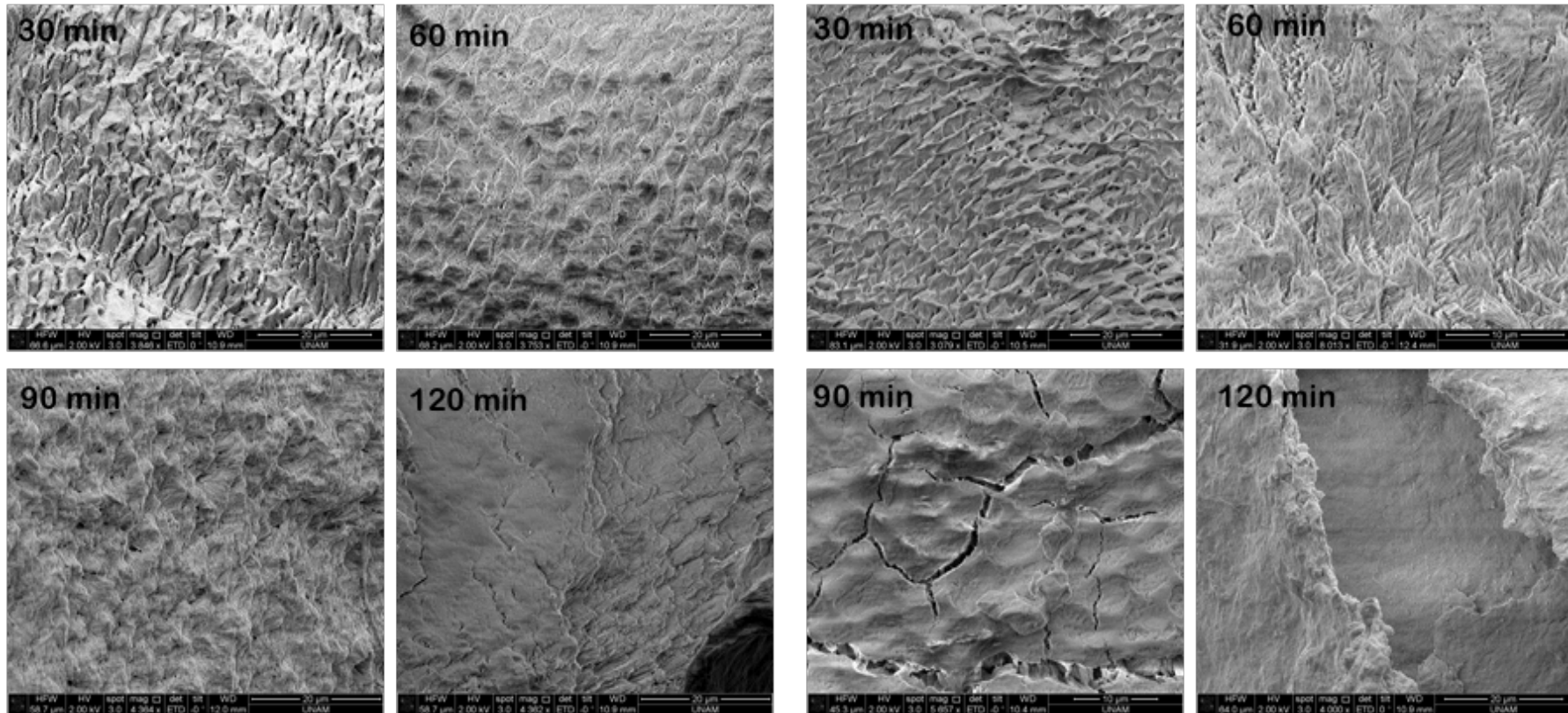


**Figure 4.4 Hydroxyapatite formation on demineralized tooth surfaces.** Demineralized teeth were treated with 100 µM E3-PA and E3-Peptides in simulated body fluid and SEM images were taken every 30 min

When LIVE/DEAD® staining was performed after 48 h incubation, although there was not notable number of dead cells in E3-PA treated HGFs, the number of live cells were decreased in 400  $\mu\text{M}$  and 800  $\mu\text{M}$  treated groups (Figure 4.6).

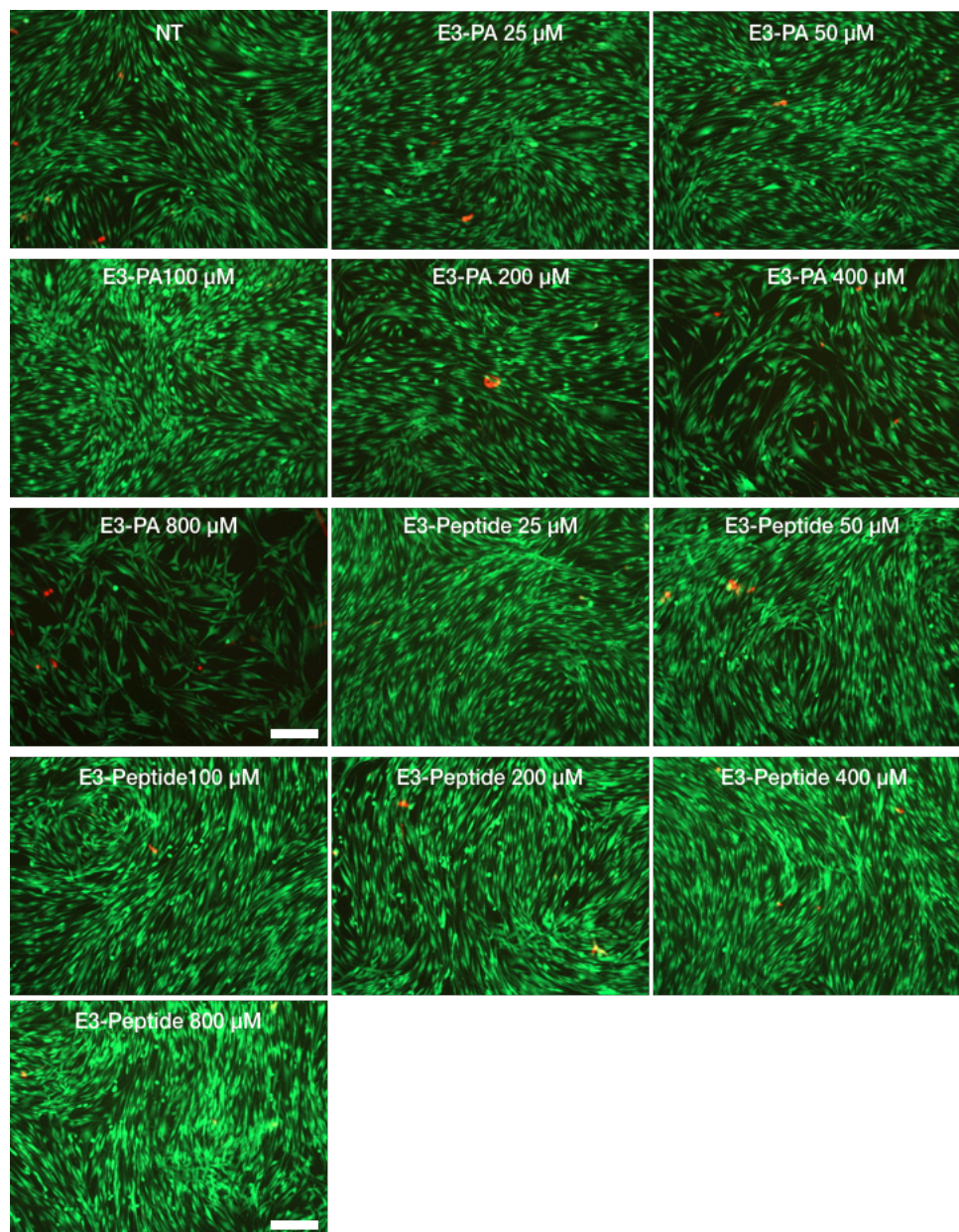


**Figure 4.6 Viability of HGFs treated with mineralizing peptides at 48 h.** HGFs were incubated with increasing doses of E3-PA and E3-Peptide in 10% FBS DMEM and calcein Am / ethidium homodimer staining was performed. Representative calcein am (live, green) and ethidium homodimer staining (red, dead) images. Scale bars are 200  $\mu\text{m}$ .

Moreover, when proliferation assay was performed with the concentration used in remineralization assay, the proliferative capacity of HGFs decreased in 100  $\mu$ M E3-PA treated group compared to E3-Peptide and control (Figure 4.7).

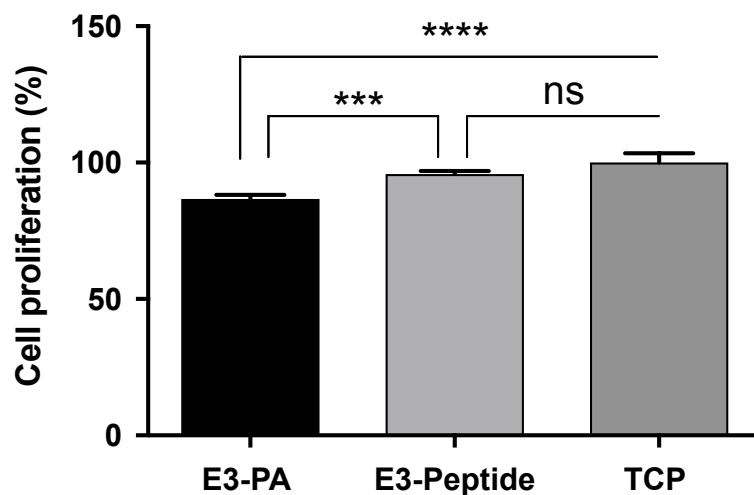


**Figure 4.7 Proliferation of HGFs treated mineralizing peptides at 24 h.** Peptide concentration was 100  $\mu$ M. Error bars show s.e.m, two independent experiments were repeated with n=4 in each experiment. One-way ANOVA with Tukey's Multiple Comparison Test was used to show the statistical significance at \*\*\* p<0.001.

The decrease in the proliferation capacity might explain reduced metabolic activity in the MTT assay. The hydrophobic tail and cationic charge are essential for cell death while designing peptides for cancer therapy and anti-microbial treatments. Anionic peptide amphiphiles are speculated as non-toxic due to electrostatic repulsion and presence of negative charges due to glycoproteins and polysaccharide chains on the cell surface. However, most of peptide studies focused on cationic peptides and their interaction with cell membrane [156]. A recent study shows that the strength of intermolecular cohesive forces between peptide molecules determine the membrane activity and interaction of peptides [157]. This might explain, decreased metabolic activity and proliferation capacity of E3-PA above critical aggregation concentrations.

## 4.5 Conclusion

In this study, amelogenin-inspired acidic self-assembling peptides were designed to induce remineralization in eroded enamel. Both E3-PA and E2-Peptide have self-assembling features yet alkyl tail increases nanomechanical and physical properties of peptide via an organized hydrogen bonding and  $\beta$ -sheet secondary structure between each peptide molecule in nanofiber. The peptide with longer sequences may attract more effectively  $\text{Ca}^{2+}$  and  $\text{PO}_4^{3-}$  ions to form new hydroxyapatites to repair eroded enamel. However, it is previously shown that longer peptides achieved by increasing the numbers of bioactive sequence (NSS) have difficulties in reaching the demineralized vacancies to initiate mineralization. Although both E3-PA and E3-Peptide have same number of bioactive epitopes (EEE), E3-PA showed slow remineralization capacity compared to E3-Peptide. Alkyl tail in E3-PA increased length of peptide sequence which might result slow remineralization. In addition to slow remineralization potential, E3-PA also showed low biocompatibility by affecting metabolic activity and proliferation of human gingival fibroblast (HGFs) above 100  $\mu\text{M}$ . In addition to biocompatibility assessments, genotoxicity and mutagenicity should be analyzed for potential clinical use of these self-assembling peptides. Overall, E3-Peptide can be potential biomolecular tools for biomimetic mineralization on the enamel surface and component novel nanomaterials for future clinical enamel erosion care.

## CHAPTER 5

### CONCLUSION & FUTURE PERSPECTIVES

In last decades, advances in nanotechnology and nanoscience have flourished development of engineered nanomaterials which are extensively used in different products including photocatalysts, food additive / packaging, optics and electronics, personal care products, cosmetics, textile, adhesives, tissue engineering, regenerative medicine, dental restoration materials, water purification system, antibacterial agents, therapeutic delivery, and medical devices. In this thesis, I studied the potential of engineered nanomaterials for intestinal metabolite delivery and enamel remineralization and developed an *in vitro* method to assess the toxicity associated with the long-term use of engineered nanomaterials.

In the first part of my dissertation, I developed a novel *in vitro* long-term accumulation model to assess long-term toxicity of metal nanoparticles by using gold nanoparticles as a model nanoparticle system. This accumulation model highlighted intracellular stress (ER stress) and mechanistic response to decrease ER stress through blocking uptake mechanism. Metal nanoparticles are promising candidates for applications such as photothermal therapy, targeted drug and gene delivery, imaging agent for magnetic resonance imaging (MRI), and anti-microbial agents etc. Therefore, thousands of industrial products or production processes that contain engineered nanoparticles and their interaction with biological systems raise increasing concerns. They are mostly speculated as “non-toxic” based on short-term *in vitro* toxicity assays. While long-term toxicity analyses are mostly based on animal experiments that do not provide insight about mechanistic interaction of the nanoparticles with the intracellular machinery. Therefore, this easy to implement accumulation model might provide an



invaluable insight about the nanoparticle-cellular machinery interactions and safer nanomaterial designs.

In the second part of this thesis, the role of a metabolic gene, HMGCS2, was investigated on intestinal stem cell maintenance and intestinal homeostasis through genetically engineered mouse models. Deletion of HMGCS2 compromised Lgr5<sup>+</sup> ISC numbers and function and induced the premature differentiation of Lgr5<sup>+</sup> ISCs into secretory cells. The effects of HMGCS2 deletion arose from its metabolite  $\beta$ OHB. Exogenous delivery of  $\beta$ OHB to *in vitro* organoids rectified the HMGCS2-null organoids and balanced colony formation and the number of secretory cells. However, *in vivo* delivery of small soluble molecules to intestine was challenging due to protective mucus layers. I assessed regenerative capacity of the modified forms of  $\beta$ OHB developed by nanoparticle synthesis (PLGA-encapsulated) and supramolecular chemistry ( $\beta$ OHB-oligomer) techniques in damaged intestine after irradiation challenge. These two approaches show the promising potential of engineered nanomaterials in drug delivery to challenging organs (e.g. stomach, intestine, colon) and might offer improvement in therapeutic approaches for the pathophysiology of gastrointestinal system such as inflammatory bowel disease and colorectal cancer.

In the last part, I developed self-assembling peptides to increase remineralization of the eroded enamel by mimicking the acidic residue of the amelogenin protein. The self-assembling peptides act as a bioorganic protein matrix of the developing enamel to guide the aggregation of the newly formed hydroxyapatite crystals. Supramolecular structure is also important for biocompatibility of self-assembling peptides. In addition, a better strategy should be developed to prevent peeling of newly formed layer on eroded enamel.

## BIBLIOGRAPHY

1. Gunduz, N., et al., *Safety of Nanomaterials*. Therapeutic Nanomaterials, 2016. **271**.
2. Blakemore, R., *Magnetotactic bacteria*. Science, 1975. **190**(4212): p. 377-9.
3. Oberdörster, G., E. Oberdörster, and J. Oberdörster, *Nanotoxicology: an emerging discipline evolving from studies of ultrafine particles*. Environ Health Perspect, 2005. **113**(7): p. 823-39.
4. Lehn, J.M., *Toward complex matter: supramolecular chemistry and self-organization*. Proc Natl Acad Sci U S A, 2002. **99**(8): p. 4763-8.
5. Rothemund, P.W., *Folding DNA to create nanoscale shapes and patterns*. Nature, 2006. **440**(7082): p. 297-302.
6. Chandrasekaran, A.R., et al., *Beyond the Fold: Emerging Biological Applications of DNA Origami*. Chembiochem, 2016. **17**(12): p. 1081-9.
7. Lin, P.C., et al., *Techniques for physicochemical characterization of nanomaterials*. Biotechnology Advances, 2014. **32**(4): p. 711-726.
8. Nel, A.E., et al., *Understanding biophysicochemical interactions at the nano-bio interface*. Nat Mater, 2009. **8**(7): p. 543-57.
9. Yang, J.A., S.E. Lohse, and C.J. Murphy, *Tuning cellular response to nanoparticles via surface chemistry and aggregation*. Small, 2014. **10**(8): p. 1642-51.
10. Dykman, L.A. and N.G. Khlebtsov, *Uptake of engineered gold nanoparticles into mammalian cells*. Chem Rev, 2014. **114**(2): p. 1258-88.
11. Agarwal, R., et al., *Mammalian cells preferentially internalize hydrogel nanodiscs over nanorods and use shape-specific uptake mechanisms*. Proc Natl Acad Sci U S A, 2013. **110**(43): p. 17247-52.
12. Barua, S., et al., *Particle shape enhances specificity of antibody-displaying nanoparticles*. Proc Natl Acad Sci U S A, 2013. **110**(9): p. 3270-5.
13. Gitrowski, C., A.R. Al-Jubory, and R.D. Handy, *Uptake of different crystal structures of TiO<sub>2</sub> nanoparticles by Caco-2 intestinal cells*. Toxicol Lett, 2014. **226**(3): p. 264-76.
14. Zhu, Z.J., et al., *The interplay of monolayer structure and serum protein interactions on the cellular uptake of gold nanoparticles*. Small, 2012. **8**(17): p. 2659-63.
15. dos Santos, T., et al., *Effects of transport inhibitors on the cellular uptake of carboxylated polystyrene nanoparticles in different cell lines*. PLoS One, 2011. **6**(9): p. e24438.
16. Kuhn, D.A., et al., *Different endocytotic uptake mechanisms for nanoparticles in epithelial cells and macrophages*. Beilstein Journal of Nanotechnology, 2014. **5**(1): p. 1625-1636.
17. Lesniak, A., et al., *Nanoparticle adhesion to the cell membrane and its effect on nanoparticle uptake efficiency*. J Am Chem Soc, 2013. **135**(4): p. 1438-44.
18. Wu, X.A., et al., *Intracellular fate of spherical nucleic Acid nanoparticle conjugates*. J Am Chem Soc, 2014. **136**(21): p. 7726-33.
19. Holt, B.D., et al., *Carbon nanotubes reorganize actin structures in cells and ex vivo*. ACS Nano, 2010. **4**(8): p. 4872-8.

20. Soenen, S.J., et al., *High intracellular iron oxide nanoparticle concentrations affect cellular cytoskeleton and focal adhesion kinase-mediated signaling*. *Small*, 2010. **6**(7): p. 832-42.
21. Cartiera, M.S., et al., *The uptake and intracellular fate of PLGA nanoparticles in epithelial cells*. *Biomaterials*, 2009. **30**(14): p. 2790-8.
22. Szabo, I., et al., *Physiology of potassium channels in the inner membrane of mitochondria*. *Pflugers Arch*, 2012. **463**(2): p. 231-46.
23. Wang, X.-H., et al., *Poly-L-lysine assisted synthesis of core-shell nanoparticles and conjugation with triphenylphosphonium to target mitochondria*. *Journal of Materials Chemistry B*, 2013. **1**(38): p. 5143-5152.
24. Theodossiou, T.A., et al., *Mitochondrial delivery of doxorubicin by triphenylphosphonium-functionalized hyperbranched nanocarriers results in rapid and severe cytotoxicity*. *Pharm Res*, 2013. **30**(11): p. 2832-42.
25. Luo, G.-F., et al., *Multifunctional Enveloped Mesoporous Silica Nanoparticles for Subcellular Co-delivery of Drug and Therapeutic Peptide*. *Sci. Rep.*, 2014. **4**.
26. Zeng, X., R. Morgenstern, and A.M. Nystrom, *Nanoparticle-directed sub-cellular localization of doxorubicin and the sensitization breast cancer cells by circumventing GST-mediated drug resistance*. *Biomaterials*, 2014. **35**(4): p. 1227-39.
27. Johnston, H.J., et al., *Evaluating the uptake and intracellular fate of polystyrene nanoparticles by primary and hepatocyte cell lines in vitro*. *Toxicol Appl Pharmacol*, 2010. **242**(1): p. 66-78.
28. Nam, H.Y., et al., *Cellular uptake mechanism and intracellular fate of hydrophobically modified glycol chitosan nanoparticles*. *J Control Release*, 2009. **135**(3): p. 259-67.
29. Krpetic, Z., et al., *Negotiation of intracellular membrane barriers by TAT-modified gold nanoparticles*. *Acs Nano*, 2011. **5**(6): p. 5195-201.
30. Nativo, P., I.A. Prior, and M. Brust, *Uptake and intracellular fate of surface-modified gold nanoparticles*. *Acs Nano*, 2008. **2**(8): p. 1639-44.
31. Zhang, E., et al., *Dynamic magnetic fields remote-control apoptosis via nanoparticle rotation*. *Acs Nano*, 2014. **8**(4): p. 3192-201.
32. Yanes, R.E., et al., *Involvement of lysosomal exocytosis in the excretion of mesoporous silica nanoparticles and enhancement of the drug delivery effect by exocytosis inhibition*. *Small*, 2013. **9**(5): p. 697-704.
33. Sahay, G., et al., *Efficiency of siRNA delivery by lipid nanoparticles is limited by endocytic recycling*. *Nat Biotechnol*, 2013. **31**(7): p. 653-8.
34. Bobo, D., et al., *Nanoparticle-Based Medicines: A Review of FDA-Approved Materials and Clinical Trials to Date*. *Pharm Res*, 2016. **33**(10): p. 2373-87.
35. Ventola, C.L., *Progress in Nanomedicine: Approved and Investigational Nanodrugs*. *P T*, 2017. **42**(12): p. 742-755.
36. Gangwal, S., et al., *Informing selection of nanomaterial concentrations for ToxCast in vitro testing based on occupational exposure potential*. *Environ Health Perspect*, 2011. **119**(11): p. 1539-46.
37. Krewski, D., et al., *Toxicity testing in the 21st century: a vision and a strategy*. *J Toxicol Environ Health B Crit Rev*, 2010. **13**(2-4): p. 51-138.

38. Demokritou, P., et al., *An in vivo and in vitro toxicological characterisation of realistic nanoscale CeO(2) inhalation exposures*. *Nanotoxicology*, 2013. **7**(8): p. 1338-50.
39. Han, X., et al., *Assessing the relevance of in vitro studies in nanotoxicology by examining correlations between in vitro and in vivo data*. *Toxicology*, 2012. **297**(1-3): p. 1-9.
40. Oberdorster, G., *Nanotoxicology: in vitro-in vivo dosimetry*. *Environ Health Perspect*, 2012. **120**(1): p. A13; author reply A13.
41. DeLoid, G., et al., *Estimating the effective density of engineered nanomaterials for in vitro dosimetry*. *Nat Commun*, 2014. **5**: p. 3514.
42. Kroll, A., et al., *Cytotoxicity screening of 23 engineered nanomaterials using a test matrix of ten cell lines and three different assays*. *Part Fibre Toxicol*, 2011. **8**: p. 9.
43. Lanone, S. and J. Boczkowski, *Biomedical applications and potential health risks of nanomaterials: molecular mechanisms*. *Curr Mol Med*, 2006. **6**(6): p. 651-63.
44. Tang, B.C., et al., *Biodegradable polymer nanoparticles that rapidly penetrate the human mucus barrier*. *Proc Natl Acad Sci U S A*, 2009. **106**(46): p. 19268-73.
45. Lamprecht, A., et al., *Biodegradable nanoparticles for targeted drug delivery in treatment of inflammatory bowel disease*. *J Pharmacol Exp Ther*, 2001. **299**(2): p. 775-81.
46. Yang, M., et al., *Biodegradable nanoparticles composed entirely of safe materials that rapidly penetrate human mucus*. *Angew Chem Int Ed Engl*, 2011. **50**(11): p. 2597-600.
47. Abramson, A., et al., *An ingestible self-orienting system for oral delivery of macromolecules*. *Science*, 2019. **363**(6427): p. 611-615.
48. Wu, J., et al., *Biomimetic Viruslike and Charge Reversible Nanoparticles to Sequentially Overcome Mucus and Epithelial Barriers for Oral Insulin Delivery*. *ACS Appl Mater Interfaces*, 2018. **10**(12): p. 9916-9928.
49. Ensign, L.M., R. Cone, and J. Hanes, *Oral drug delivery with polymeric nanoparticles: the gastrointestinal mucus barriers*. *Adv Drug Deliv Rev*, 2012. **64**(6): p. 557-70.
50. Gruber, P., M.A. Longer, and J.R. Robinson, *Some biological issues in oral, controlled drug delivery*. *Advanced Drug Delivery Reviews*, 1987. **1**(1): p. 1-18.
51. Kararli, T.T., *Comparison of the gastrointestinal anatomy, physiology, and biochemistry of humans and commonly used laboratory animals*. *Biopharm Drug Dispos*, 1995. **16**(5): p. 351-80.
52. Lai, S.K., Y.Y. Wang, and J. Hanes, *Mucus-penetrating nanoparticles for drug and gene delivery to mucosal tissues*. *Adv Drug Deliv Rev*, 2009. **61**(2): p. 158-71.
53. Knoll, A.H., *Biomineralization and Evolutionary History*. *Reviews in Mineralogy and Geochemistry*, 2003. **54**(1): p. 329-356.
54. Manolagas, S.C., *Birth and death of bone cells: basic regulatory mechanisms and implications for the pathogenesis and treatment of osteoporosis*. *Endocr Rev*, 2000. **21**(2): p. 115-37.

55. Palmer, L.C., et al., *Biomimetic systems for hydroxyapatite mineralization inspired by bone and enamel*. Chem Rev, 2008. **108**(11): p. 4754-83.
56. Chen, H., et al., *Self-assembly of synthetic hydroxyapatite nanorods into an enamel prism-like structure*. J Colloid Interface Sci, 2005. **288**(1): p. 97-103.
57. Wu, D., et al., *Hydroxyapatite-anchored dendrimer for in situ remineralization of human tooth enamel*. Biomaterials, 2013. **34**(21): p. 5036-47.
58. Schachschal, S., A. Pich, and H.J. Adler, *Aqueous microgels for the growth of hydroxyapatite nanocrystals*. Langmuir, 2008. **24**(9): p. 5129-34.
59. Cao, Y., et al., *Agarose hydrogel biomimetic mineralization model for the regeneration of enamel prismlike tissue*. ACS Appl Mater Interfaces, 2014. **6**(1): p. 410-20.
60. Hsu, C.C., et al., *Influence of 8DSS peptide on nano-mechanical behavior of human enamel*. J Dent Res, 2011. **90**(1): p. 88-92.
61. Dogan, S., et al., *Biomimetic Tooth Repair: Amelogenin-Derived Peptide Enables in Vitro Remineralization of Human Enamel*. ACS Biomaterials Science & Engineering, 2018. **4**(5): p. 1788-1796.
62. Kirkham, J., et al., *Self-assembling peptide scaffolds promote enamel remineralization*. J Dent Res, 2007. **86**(5): p. 426-30.
63. Yamagishi, K., et al., *Materials chemistry: a synthetic enamel for rapid tooth repair*. Nature, 2005. **433**(7028): p. 819.
64. Li, L., et al., *Repair of enamel by using hydroxyapatite nanoparticles as the building blocks*. Journal of Materials Chemistry, 2008. **18**(34): p. 4079-4084.
65. Li, L., et al., *Bio-inspired enamel repair via Glu-directed assembly of apatite nanoparticles: an approach to biomaterials with optimal characteristics*. Adv Mater, 2011. **23**(40): p. 4695-701.
66. Gunduz, N., et al., *Intracellular Accumulation of Gold Nanoparticles Leads to Inhibition of Macropinocytosis to Reduce the Endoplasmic Reticulum Stress*. Sci Rep, 2017. **7**: p. 40493.
67. Nel, A., et al., *Toxic potential of materials at the nanolevel*. Science, 2006. **311**(5761): p. 622-7.
68. Migowski, P. and J. Dupont, *Catalytic applications of metal nanoparticles in imidazolium ionic liquids*. Chemistry, 2007. **13**(1): p. 32-9.
69. Giljohann, D.A., et al., *Gold nanoparticles for biology and medicine*. Angew Chem Int Ed Engl, 2010. **49**(19): p. 3280-94.
70. Dreaden, E.C., et al., *The golden age: gold nanoparticles for biomedicine*. Chem Soc Rev, 2012. **41**(7): p. 2740-79.
71. Daniel, M.C. and D. Astruc, *Gold nanoparticles: assembly, supramolecular chemistry, quantum-size-related properties, and applications toward biology, catalysis, and nanotechnology*. Chem Rev, 2004. **104**(1): p. 293-346.
72. Turkevich, J.a.S.P.C.a.H.J., *A study of the nucleation and growth processes in the synthesis of colloidal gold*. Discussions of the Faraday Society, 1951. **11**: p. 55.
73. G, F., *Controlled Nucleation for the Regulation of the Particle Size in Monodisperse Gold Suspensions*. Nature physical science, 1973.
74. Brust, M., et al., *Synthesis of thiol-derivatised gold nanoparticles in a two-phase liquid-liquid system*. Journal of the Chemical Society, Chemical Communications, 1994(7): p. 801-802.

75. Hostetler, M.J.a.W.J.E.a.Z.C.-J.a.H.J.E.a.V.R.W.a.C.M.R.a.L.J.D.a., *Alkanethiolate Gold Cluster Molecules with Core Diameters from 1.5 to 5.2 nm: Core and Monolayer Properties as a Function of Core Size*. Langmuir, 1998. **14**(1): p. 17-30.
76. Woehrle, G.H., L.O. Brown, and J.E. Hutchison, *Thiol-functionalized, 1.5-nm gold nanoparticles through ligand exchange reactions: scope and mechanism of ligand exchange*. J Am Chem Soc, 2005. **127**(7): p. 2172-83.
77. Soenen, S.J., et al., *Cytotoxic effects of gold nanoparticles: a multiparametric study*. ACS Nano, 2012. **6**(7): p. 5767-83.
78. Gulsuner, H.U., et al., *Multi-domain short peptide molecules for in situ synthesis and biofunctionalization of gold nanoparticles for integrin-targeted cell uptake*. ACS Appl Mater Interfaces, 2015. **7**(20): p. 10677-83.
79. Scari, G., et al., *Gold nanoparticles capped by a GC-containing peptide functionalized with an RGD motif for integrin targeting*. Bioconjug Chem, 2012. **23**(3): p. 340-9.
80. Bansal, K., et al., *A Facile Approach for Synthesis and Intracellular Delivery of Size Tunable Cationic Peptide Functionalized Gold Nanohybrids in Cancer Cells*. Bioconjug Chem, 2018. **29**(4): p. 1102-1110.
81. Kennedy, L.C., et al., *A new era for cancer treatment: gold-nanoparticle-mediated thermal therapies*. Small, 2011. **7**(2): p. 169-83.
82. Kim, B., et al., *Tuning payload delivery in tumour cylindroids using gold nanoparticles*. Nat Nanotechnol, 2010. **5**(6): p. 465-72.
83. Pissuwan, D., T. Niidome, and M.B. Cortie, *The forthcoming applications of gold nanoparticles in drug and gene delivery systems*. J Control Release, 2011. **149**(1): p. 65-71.
84. Tsai, C.Y., et al., *Amelioration of collagen-induced arthritis in rats by nanogold*. Arthritis Rheum, 2007. **56**(2): p. 544-54.
85. Walkey, C.D., et al., *Nanoparticle size and surface chemistry determine serum protein adsorption and macrophage uptake*. J Am Chem Soc, 2012. **134**(4): p. 2139-47.
86. Walkey, C.D., et al., *Protein corona fingerprinting predicts the cellular interaction of gold and silver nanoparticles*. ACS Nano, 2014. **8**(3): p. 2439-55.
87. Salvati, A., et al., *Transferrin-functionalized nanoparticles lose their targeting capabilities when a biomolecule corona adsorbs on the surface*. Nat Nanotechnol, 2013. **8**(2): p. 137-43.
88. Annangi, B., et al., *Long-term exposures to low doses of cobalt nanoparticles induce cell transformation enhanced by oxidative damage*. Nanotoxicology, 2015. **9**(2): p. 138-47.
89. Coccini, T., et al., *Assessment of cellular responses after short- and long-term exposure to silver nanoparticles in human neuroblastoma (SH-SY5Y) and astrocytoma (D384) cells*. ScientificWorldJournal, 2014. **2014**: p. 259765.
90. Comfort, K.K., et al., *Less is more: long-term in vitro exposure to low levels of silver nanoparticles provides new insights for nanomaterial evaluation*. ACS Nano, 2014. **8**(4): p. 3260-71.
91. Mrakovcic, M., et al., *Assessment of long-term effects of nanoparticles in a microcarrier cell culture system*. PLoS One, 2013. **8**(2): p. e56791.

92. Mironava, T., et al., *Gold nanoparticles cellular toxicity and recovery: adipose Derived Stromal cells*. *Nanotoxicology*, 2014. **8**(2): p. 189-201.
93. Falagan-Lotsch, P., E.M. Grzincic, and C.J. Murphy, *One low-dose exposure of gold nanoparticles induces long-term changes in human cells*. *Proc Natl Acad Sci U S A*, 2016. **113**(47): p. 13318-13323.
94. Samali, A., et al., *Methods for monitoring endoplasmic reticulum stress and the unfolded protein response*. *Int J Cell Biol*, 2010. **2010**: p. 830307.
95. van Schadewijk, A., et al., *A quantitative method for detection of spliced X-box binding protein-1 (XBPI) mRNA as a measure of endoplasmic reticulum (ER) stress*. *Cell Stress Chaperones*, 2012. **17**(2): p. 275-9.
96. Bartczak, D., et al., *Exocytosis of peptide functionalized gold nanoparticles in endothelial cells*. *Nanoscale*, 2012. **4**(15): p. 4470-2.
97. Love, S.A., Z. Liu, and C.L. Haynes, *Examining changes in cellular communication in neuroendocrine cells after noble metal nanoparticle exposure*. *Analyst*, 2012. **137**(13): p. 3004-10.
98. Oh, N. and J.H. Park, *Surface chemistry of gold nanoparticles mediates their exocytosis in macrophages*. *ACS Nano*, 2014. **8**(6): p. 6232-41.
99. Mironava, T., et al., *Gold nanoparticles cellular toxicity and recovery: effect of size, concentration and exposure time*. *Nanotoxicology*, 2010. **4**(1): p. 120-37.
100. Krpetić, Z., et al., *Phagocytosis of biocompatible gold nanoparticles*. *Langmuir*, 2010. **26**(18): p. 14799-805.
101. Chithrani, B.D., A.A. Ghazani, and W.C. Chan, *Determining the size and shape dependence of gold nanoparticle uptake into mammalian cells*. *Nano Lett*, 2006. **6**(4): p. 662-8.
102. Ye, D., et al., *Nanoparticle accumulation and transcytosis in brain endothelial cell layers*. *Nanoscale*, 2013. **5**(22): p. 11153-65.
103. Zhang, W., et al., *Trafficking of gold nanorods in breast cancer cells: uptake, lysosome maturation, and elimination*. *ACS Appl Mater Interfaces*, 2013. **5**(19): p. 9856-65.
104. Deng, Z.J., et al., *Nanoparticle-induced unfolding of fibrinogen promotes Mac-1 receptor activation and inflammation*. *Nat Nanotechnol*, 2011. **6**(1): p. 39-44.
105. Xia, T., et al., *Comparison of the mechanism of toxicity of zinc oxide and cerium oxide nanoparticles based on dissolution and oxidative stress properties*. *ACS Nano*, 2008. **2**(10): p. 2121-34.
106. Szegezdi, E., et al., *Mediators of endoplasmic reticulum stress-induced apoptosis*. *EMBO Rep*, 2006. **7**(9): p. 880-5.
107. Noh, J.Y., et al., *SCAMP5 links endoplasmic reticulum stress to the accumulation of expanded polyglutamine protein aggregates via endocytosis inhibition*. *J Biol Chem*, 2009. **284**(17): p. 11318-25.
108. Li, J.J., N. Kawazoe, and G. Chen, *Gold nanoparticles with different charge and moiety induce differential cell response on mesenchymal stem cell osteogenesis*. *Biomaterials*, 2015. **54**: p. 226-36.
109. Cheng, H. and C.P. Leblond, *Origin, differentiation and renewal of the four main epithelial cell types in the mouse small intestine. V. Unitarian Theory of the origin of the four epithelial cell types*. *Am J Anat*, 1974. **141**(4): p. 537-61.

110. Karam, S.M., *Lineage commitment and maturation of epithelial cells in the gut*. Front Biosci, 1999. **4**: p. D286-98.
111. Radtke, F. and H. Clevers, *Self-renewal and cancer of the gut: two sides of a coin*. Science, 2005. **307**(5717): p. 1904-9.
112. Winton, D.J., M.A. Blount, and B.A. Ponder, *A clonal marker induced by mutation in mouse intestinal epithelium*. Nature, 1988. **333**(6172): p. 463-6.
113. Bjerknes, M. and H. Cheng, *Clonal analysis of mouse intestinal epithelial progenitors*. Gastroenterology, 1999. **116**(1): p. 7-14.
114. Sancho, E., E. Batlle, and H. Clevers, *Signaling pathways in intestinal development and cancer*. Annu Rev Cell Dev Biol, 2004. **20**: p. 695-723.
115. Barker, N., et al., *Identification of stem cells in small intestine and colon by marker gene Lgr5*. Nature, 2007. **449**(7165): p. 1003-7.
116. Mihaylova, M.M., D.M. Sabatini, and Ö. Yilmaz, *Dietary and metabolic control of stem cell function in physiology and cancer*. Cell Stem Cell, 2014. **14**(3): p. 292-305.
117. Yilmaz, Ö., et al., *mTORC1 in the Paneth cell niche couples intestinal stem-cell function to calorie intake*. Nature, 2012. **486**(7404): p. 490-5.
118. Igarashi, M. and L. Guarente, *mTORC1 and SIRT1 Cooperate to Foster Expansion of Gut Adult Stem Cells during Calorie Restriction*. Cell, 2016. **166**(2): p. 436-450.
119. Beyaz, S., et al., *High-fat diet enhances stemness and tumorigenicity of intestinal progenitors*. Nature, 2016. **531**(7592): p. 53-8.
120. Wang, B., et al., *Phospholipid Remodeling and Cholesterol Availability Regulate Intestinal Stemness and Tumorigenesis*. Cell Stem Cell, 2018. **22**(2): p. 206-220.e4.
121. Obniski, R., M. Sieber, and A.C. Spradling, *Dietary Lipids Modulate Notch Signaling and Influence Adult Intestinal Development and Metabolism in Drosophila*. Dev Cell, 2018. **47**(1): p. 98-111.e5.
122. Peregrina, K., et al., *Vitamin D is a determinant of mouse intestinal Lgr5 stem cell functions*. Carcinogenesis, 2015. **36**(1): p. 25-31.
123. Mihaylova, M.M., et al., *Fasting Activates Fatty Acid Oxidation to Enhance Intestinal Stem Cell Function during Homeostasis and Aging*. Cell Stem Cell, 2018. **22**(5): p. 769-778.e4.
124. Skarnes, W.C., et al., *A conditional knockout resource for the genome-wide study of mouse gene function*. Nature, 2011. **474**(7351): p. 337-42.
125. Huch, M., et al., *In vitro expansion of single Lgr5+ liver stem cells induced by Wnt-driven regeneration*. Nature, 2013. **494**(7436): p. 247-50.
126. Sato, T., et al., *Single Lgr5 stem cells build crypt-villus structures in vitro without a mesenchymal niche*. Nature, 2009.
127. Yin, X., et al., *Niche-independent high-purity cultures of Lgr5+ intestinal stem cells and their progeny*. Nat Methods, 2014. **11**(1): p. 106-12.
128. Ootani, A., et al., *Sustained in vitro intestinal epithelial culture within a Wnt-dependent stem cell niche*. Nat Med, 2009. **15**(6): p. 701-6.
129. Astete, C.E. and C.M. Sabliov, *Synthesis and characterization of PLGA nanoparticles*. J Biomater Sci Polym Ed, 2006. **17**(3): p. 247-89.
130. Jaipuri, F.A., B.D. Bower, and N.L. Pohl, *Protic acid-catalyzed polymerization of beta-lactones for the synthesis of chiral polyesters*. Tetrahedron-Asymmetry, 2003. **14**(20): p. 3249-3252.



131. Dedkova, E.N. and L.A. Blatter, *Role of  $\beta$ -hydroxybutyrate, its polymer poly- $\beta$ -hydroxybutyrate and inorganic polyphosphate in mammalian health and disease*. *Front Physiol*, 2014. **5**: p. 260.
132. Seebach, D., et al., *High-yield synthesis of 20-membered, 24-membered, and 28-membered macropentolide, macrohexolide, and macroheptolide, respectively, from (r)-3-hydroxybutanoic or (s)-3-hydroxybutanoic acid under yamaguchi macrolactonization conditions*. *Helvetica Chimica Acta*, 1988. **71**(1): p. 155-167.
133. Sato, T., et al., *Single Lgr5 stem cells build crypt-villus structures in vitro without a mesenchymal niche*. *Nature*, 2009. **459**(7244): p. 262-5.
134. Sato, T., et al., *Paneth cells constitute the niche for Lgr5 stem cells in intestinal crypts*. *Nature*, 2011. **469**(7330): p. 415-8.
135. Helenius, T.O., et al., *Keratin 8 absence down-regulates colonocyte HMGCS2 and modulates colonic ketogenesis and energy metabolism*. *Mol Biol Cell*, 2015. **26**(12): p. 2298-310.
136. Muñoz, J., et al., *The Lgr5 intestinal stem cell signature: robust expression of proposed quiescent '+4' cell markers*. *EMBO J*, 2012. **31**(14): p. 3079-91.
137. Cherbuy, C., et al., *Expression of mitochondrial HMGCoA synthase and glutaminase in the colonic mucosa is modulated by bacterial species*. *Eur J Biochem*, 2004. **271**(1): p. 87-95.
138. Metcalfe, C., et al., *Lgr5+ stem cells are indispensable for radiation-induced intestinal regeneration*. *Cell Stem Cell*, 2014. **14**(2): p. 149-59.
139. Wang, Q., et al., *Ketogenesis contributes to intestinal cell differentiation*. *Cell Death Differ*, 2017. **24**(3): p. 458-468.
140. Newman, J.C. and E. Verdin, *Ketone bodies as signaling metabolites*. *Trends Endocrinol Metab*, 2014. **25**(1): p. 42-52.
141. Youm, Y.H., et al., *The ketone metabolite  $\beta$ -hydroxybutyrate blocks NLRP3 inflammasome-mediated inflammatory disease*. *Nat Med*, 2015. **21**(3): p. 263-9.
142. Makadia, H.K. and S.J. Siegel, *Poly Lactic-co-Glycolic Acid (PLGA) as Biodegradable Controlled Drug Delivery Carrier*. *Polymers (Basel)*, 2011. **3**(3): p. 1377-1397.
143. Duan, Y., et al., *Effects of dietary poly- $\beta$ -hydroxybutyrate (PHB) on microbiota composition and the mTOR signaling pathway in the intestines of *litopenaeus vannamei**. *J Microbiol*, 2017. **55**(12): p. 946-954.
144. Jernvall, J. and I. Thesleff, *Tooth shape formation and tooth renewal: evolving with the same signals*. *Development*, 2012. **139**(19): p. 3487-97.
145. Bartlett, J.D., *Dental enamel development: proteinases and their enamel matrix substrates*. *ISRN Dent*, 2013. **2013**: p. 684607.
146. Smith, C.E., *Cellular and chemical events during enamel maturation*. *Crit Rev Oral Biol Med*, 1998. **9**(2): p. 128-61.
147. Reynolds, E.C., *Remineralization of enamel subsurface lesions by casein phosphopeptide-stabilized calcium phosphate solutions*. *Journal of Dental Research*, 1997. **76**(9): p. 1587-1595.
148. Wu, D., et al., *Hydroxyapatite-anchored dendrimer for in situ remineralization of human tooth enamel*. *Biomaterials*, 2013. **34**(21): p. 5036-5047.

149. Ruan, Q., et al., *An amelogenin-chitosan matrix promotes assembly of an enamel-like layer with a dense interface*. Acta Biomater, 2013. **9**(7): p. 7289-97.
150. Kokubo, T., et al., *Solutions able to reproduce in vivo surface-structure changes in bioactive glass-ceramic A-W*. J Biomed Mater Res, 1990. **24**(6): p. 721-34.
151. Termine, J.D., et al., *Properties of dissociatively extracted fetal tooth matrix proteins. I. Principal molecular species in developing bovine enamel*. J Biol Chem, 1980. **255**(20): p. 9760-8.
152. Ceylan, H., et al., *Bone-like mineral nucleating peptide nanofibers induce differentiation of human mesenchymal stem cells into mature osteoblasts*. Biomacromolecules, 2014. **15**(7): p. 2407-18.
153. Pashuck, E.T., H. Cui, and S.I. Stupp, *Tuning supramolecular rigidity of peptide fibers through molecular structure*. J Am Chem Soc, 2010. **132**(17): p. 6041-6.
154. Aggeli, A., et al., *Hierarchical self-assembly of chiral rod-like molecules as a model for peptide beta -sheet tapes, ribbons, fibrils, and fibers*. Proc Natl Acad Sci U S A, 2001. **98**(21): p. 11857-62.
155. Gulseren, G., et al., *Dentin Phosphoprotein Mimetic Peptide Nanofibers Promote Biomineralization*. Macromol Biosci, 2019. **19**(1): p. e1800080.
156. Newcomb, C.J., et al., *Cell death versus cell survival instructed by supramolecular cohesion of nanostructures*. Nat Commun, 2014. **5**: p. 3321.
157. Kornmueller, K., et al., *Peptides at the Interface: Self-Assembly of Amphiphilic Designer Peptides and Their Membrane Interaction Propensity*. Biomacromolecules, 2016. **17**(11): p. 3591-3601.

## APPENDIX A

### Copyright Clearance Agreements †

Reference Number	License Supplier	License Number
[1]	John Wiley and Sons	4570261233267
[6]	John Wiley and Sons	4565940893537
[47]	Science	4547080814554
[48]	American Chemical Society	Permission not required
[34]	Springer Nature	4566231428166
[124]	Springer Nature	4553170693238

† All license agreements between Nuray Gündüz and the License Suppliers are made by means of Copyright Clearance Center (CCC).

## APPENDIX B

### Publications

#### Submitted:

Cheng C.W., Biton M., Haber A.L., **Gunduz N.**, Eng G., Gaynor L.T., Tripathi S., Kocal-Calibasi G., Rickelt S., Gebert N., Butty V., Moreno M., Iqbal A.M., Bauer-Rowe K.E., Mylonas C., Whary M.T., Levine S.S., Hynes, R.O., Kenudson M.O., Deshpande V., Boyer L.A., Mihaylova M.M., Ori A., Fox J.G., Regev A. and Yilmaz O.H. Endogenous ketones instruct intestinal stem cell fate through Notch signaling. (submitted)

#### In preparation:

Sen M., Tuncay I.O., Yaylaci S, Sever M., **Gunduz N.**, Onat O.O., Tasdelen U., Kilinc G.M., Ulukan C., Aslanbaba E., Durmaz-Celik, F.N., Dogu O., Topaloglu H., Elibol B., Akbostanci C., Ozcelik T., Tekinay A.B. Gene MMP19p.Arg456Gln as the Disease-Causing Mutation for Two Different Families with Essential Tremor (in preparation)

**Gunduz, N.**, Guler, M.O., Tekinay, A.B. Self-assembling peptides for remineralization of enamel. (in preparation)

#### Published:

**Gunduz, N.**, Ceylan, H., Guler, M.O., Tekinay, A.B. Intracellular Accumulation of Gold Nanoparticles Leads to inhibition of Macropinocytosis to Reduce the Endoplasmic Reticulum Stress, Sci Rep. 2017 Feb 1; 7: 40493. DOI: 10.1038/srep40493.

Tohumeken, S., **Gunduz, N.**, Demircan, M.B., Gunay, G., Topal, A.E., Khalily, M.A., Tekinay, T., Dana, A., Guler, M.O., Tekinay, A.B., A Modular Antigen Presenting Peptide/Oligonucleotide Nanostructure Platform for Inducing Potent Immune Response Advanced Biosystems; Wiley, 2017,1,1700015 DOI: 10.1002/adbi.201700015

Yasa, I.C\*., **Gunduz, N\*.**, Kilinc, M., Guler, M.O., Tekinay, A.B., Basal Lamina Mimetic Nanofibrous Peptide Networks for Skeletal Myogenesis, Sci Rep. 2015 Nov 10; 5: 16460. DOI: 10.1038/srep16460. (\*Equal contribution)

Mammadov, R., Cinar, G., **Gunduz, N.**, Goktas, M., Kayhan, H., Tohumeken, S., Topal, A.E., Orujalipoor, I., Delibasi, T., Dana, A., Ide, S., Tekinay, A.B., Guler, M.O., Virus-like nanostructures for tuning immune response, Sci Rep. 2015 Nov 18; 5: 16728. DOI: 10.1038/srep16728

*Book Chapter:*

**Gunduz, N.**, Arslan, E., Guler, M.O., Tekinay, A.B., Safety of Nanomaterials, Therapeutic Nanomaterials. Wiley, ISBN: 978-1-118-98745-2.